Summer 8-15-2019

Adiabatic Dark Matter Density Cusps Around Supermassive Black Holes and Dark Matter Detection

Augusto Medeiros Da Rosa
Washington University in St. Louis

Recommended Citation

Medeiros Da Rosa, Augusto, "Adiabatic Dark Matter Density Cusps Around Supermassive Black Holes and Dark Matter Detection" (2019). *Arts & Sciences Electronic Theses and Dissertations*. 1928.
https://openscholarship.wustl.edu/art_sci_etds/1928

WASHINGTON UNIVERSITY IN ST. LOUIS
DEPARTMENT OF PHYSICS

Dissertation Examination Committee:
Francesc Ferrer, Chair
Claude W. Bernard
Renato Feres
Henric Krawczynski
Michael C. Ogilvie

Adiabatic Dark Matter Density Cusps Around Supermassive Black Holes and Dark Matter Detection

by
Augusto Medeiros da Rosa

A dissertation presented to
The Graduate School
of Washington University in
partial fullfillment of the
requirements for the degree
of Doctor of Philosophy

St. Louis, Missouri
August, 2019

Contents

List of Figures

List of Tables

Abbreviations

BH Black Hole.

DM Dark Matter.

FRW Friedmann, Robertson, Walker.

GC Galactic Center.

GR General Relativity.

GS Gondolo and Silk, Phys. Rev. Lett, 83:1719-1722, 1999.

MACHO Massive Compact Halo Object.

MC Monte Carlo.

MSSM Minimal Supersymmetric Standard Model.

NFW Navarro, Frenk, White.

NMSSM Next-to-Minimal Supersymmetric Standard Model.

NSC Nuclear Star Cluster.

PBH Primordial Black Hole.

SFW Laleh Sadeghian, Francesc Ferrer, and Clifford M.Will, Phys. Rev., D88(6):063522,2013.

SM Standard Model of Particle Physics.

SMBH Supermassive Black Hole.

WIMP Weakly Interacting Massive Particle.

Acknowledgements

During my time as a graduate student, I have had the opportunity to think about varied and interesting topics in particle physics and cosmology. I am grateful to my adviser, Francesc Ferrer, for providing the necessary support I needed along the way, and sharing invaluable insight into how to tackle the problems I was trying to solve.

I also want to thank my committee members, Claude Bernard, Michael Ogilvie, Henric Krawczynski, and Renato Feres. In particular, I would like to thank Prof. Krawczynski for letting me participate in his research group's discussions on general relativity, since those helped solidify important concepts and influenced the way in which I chose to present some of the concepts in this thesis.

It has been a pleasure spending my time as a PhD student with the amazing and friends and I colleagues that I met in St. Louis. I would like to thank my good friends Nathan Walsh, Janie Walsh, Mack Atkinson, Erika Schumacher, Kim Sukhum, Brendan Haas, Robert Ashcraft, Salina Bush, Tyler Webb, Lauren Williams, Jordan Russell, and Emily Russell. You were all like family these past six years, and I am deeply grateful for the friendship and support I got from all of you.

Being a peer mentor gave me the opportunity to meet basically every graduate student that has been in the physics department for the past six years, and it would be impossible to acknowledge all of them individually in a few short paragraphs. That said, I would like to thank my mentor colleagues Kelsey Meinerz, Andrew West, Lindsey Lisalda, Joben Lewis, Matt Reisman, and Ryan Murphy. You have all helped me feel at home in St. Louis and I very much enjoyed working with you to make this department the welcoming place that it feels like.

More recently, I have had the pleasure of spending time with my "office mates" Quin Abarr and Wolfgang Zober, who helped me get through writing stress. I am also grateful to Katie Randolph for helping me work through the anxiety of figuring out who my next self is going to be.

Being in a superposition of being at home and not at home, it is not often that a foreigner gets to feel like they are socially relevant, but my organizng comrades have made that and so much more possible. You have helped me become a better person by engaging in the fight for social and economic justice that is ongoing on this campus. Thank you, John Cavin, Lucky Santino, Grace Ward, Sarah Siegel, Sarah Crosley, Charles McCrory, Trent McDonald, Marc Blanc, Alex Cook, Les Stitt, and Spencer McAvoy.

Finally, I wish to thank my friends from Brazil, who have kept in touch in spite of the distance. You are the best friends anyone could have wished for, and I am grateful for all the support you have given me, even from afar. Thank you, Arthur Loureiro, Laura Piovesan, Luiz Aguinsky, Ingrid Pelisoli, Débora Peretti, Guilherme Kolinger, and Isadora Alves. In particular, I want to thank Natália Calleya for being around to speak Portuguese.

Augusto Medeiros da Rosa

Washington University in St. Louis
August, 2019

ABSTRACT OF THE DISSERTATION

Adiabatic Dark Matter Density Cusps Around Supermassive Black Holes
and Dark Matter Detection by
Augusto Medeiros da Rosa
Doctor of Philosophy in Physics
Washington University in St.Louis, 2019
Professor Francesc Ferrer (Chair)

The growth of a black hole surrounded by dark matter can lead to a significant enhancement of the dark matter density close to the hole. We investigate this effect, focusing on the phenomenologically interesting case where the black hole is supermassive and is embedded in a galactic dark matter halo, although the formalism developed does not depend on that fact. Due to the enhanced gravitational potential, the dark matter will tend to cluster around the black hole. The precise details of this clustering will, in general, depend on the formation process of the black hole. However, if the black hole grows slowly with respect to the orbital timescales of the local galactic potential, the density cusp only depends on the black hole's mass and spin, as well as on the local distribution of orbits.

The density cusp generated by the growing black hole is called an adiabatic spike. In the context of dark matter density cusps, these spikes were first investigated by Gondolo and Silk (1999), using a phase space analysis. General relativistic effects originating from the black hole's mass were calculated by Sadeghian, Ferrer, and Will (2013), revealing an enhancement of the density in the spike. Our work extends this calculation to include the effects of spin. We find a further enhancement to the spike that is strongly dependent on the black hole's spin parameter, meaning that it cannot be ignored for rapidly spinning black holes. We estimate its impact in local annihilation rates for two particular physical processes: particle dark matter annihilation in the s-channel, and the merger rate of binaries composed of primordial black holes in the local universe. We also present a derivation of the two-body collision rate per four-volume in terms of the phase space distribution that can be used in any coordinate system.

Whoever, horizon, passes beyond you
Passes from view, not from living or being.
Don't call the soul dead when it flies away.
Say: It vanished out there in the sea.

—Fernando Pessoa, 1922

Chapter 1

Introduction

This thesis is concerned with a possible observable connection between the black holes (BHs) at the centers of galaxies and indirect detection of dark matter (DM). We will begin by introducing a few of the basic concepts about the evidence for dark matter in the universe, some proposed candidates for its composition, galactic black holes and the adiabatic growth model.

We will use units in which $\hbar = c = 1$, but we will not make the gravitational constant G equal to unity. Our convention for the metric signature is $(-{+}{+}{+})$, meaning that, for example, the mass shell condition for a particle reads $p^2 = -m^2$, where p is the particle's 4-momentum and m its mass. Note that we will not necessarily attach indices to 4-vector quantities. When indices are used, the Einstein summation convention for repeated indices is assumed. We will use greek indices to indicate the components of a 4-dimensional tensor, and components of a 3-dimensional tensor will be represented by latin indices. A spatial 3-vector quantity in a given frame will be represented in bold face.

1.1 Evidence for Dark Matter

1.1.1 Beginnings, galactic scale evidence

Evidence for a discrepancy between the visible mass and the total mass in the universe like galaxies and galaxy has been steadily mounting since the 1930s. When these observations were first made, it was possible that this excess mass may have been in the form of cool stars or planets that could not be observed from the radiation they emit. Cosmological observations, to be discussed later, show that this is not the case.

More precisely, in the cosmological context, any massive component that has a pressure negligible compared to its energy density is referred to as *matter*. What observations have shown is that not all of the matter in the universe is composed of nuclei and electrons, like the ordinary matter that the Earth is composed of (see [3, 4, 5] for recent reviews). Nuclei and electrons are collectively referred to as baryons in the astronomical context.

The dark matter/dark energy paradigm has been successful at describing the bulk of the available evidence, in what has been called as a "concordance" model [6], and we will assume in this work that dark matter exists. Nevertheless, efforts have been made to describe observations with modifications of gravity.

Historically, the first piece of evidence was obtained by Zwicky [7], using observations of the velocities of galaxies in virialized clusters. The virial theorem, valid for any gravitationally bound system in a steady state[1], states that

$$\begin{gathered} 2T + U = 0, \\ T = \frac{1}{2}\sum_i m_i v_i^2, U = -\frac{1}{2}\sum_{i\neq j}\frac{G m_i m_j}{|\boldsymbol{r}_i - \boldsymbol{r}_j|}. \end{gathered} \tag{1.1}$$

This allows us to estimate the mass of the cluster as follows:

$$M = \frac{2\langle v^2\rangle}{G\langle \frac{1}{r}\rangle}. \tag{1.2}$$

To estimate $\langle v^2\rangle$, one can use the spread in the Doppler shift of the galaxies in the cluster, and $\langle \frac{1}{r}\rangle$ can be measured by the angular separation distance of members of the cluster, provided that the distance to the cluster is known. Zwicky's application of this

---

[1] The steady state condition is problematic observationally, as some objects that appear to be members of the cluster may not necessarily be bound to it.

method to the Coma cluster indicated that its mass was many times larger than what could be accounted for by the visible matter. This observation is independent of the nature of this “dark matter”, but may be used to estimate how much of it is in the universe.

The starting point is the mass to light ratio M/L (L is the cluster luminosity) that is usually provided by observations like Zwicky’s. A measure of the luminosity per unit volume of the universe $\mathcal{L}$ would then allow us to obtain the mass density of the universe, if the M/L value obtained for clusters is universal. By universal, we mean that it should apply not just across different types of clusters, but also for “field galaxies” that are not bound to a cluster. This is important since most of the light in the universe comes from these field galaxies.

In terms of the critical density of the universe, defined below by Eq. (1.6), this method yields $\rho_M \simeq 0.15\rho_{\text{crit}}$ [8], which is lower than what is implied by other pieces of evidence, but already large enough to rule out that all the matter in the universe is baryonic since primordial nucleosynthesis provides an estimate of the baryon density $\rho_B \simeq 0.04\rho_{\text{crit}}$.

Observations have also shown a mass discrepancy at galaxy scales through measurements of galactic rotation curves, a work that was pioneered by Vera Rubin [9]. Modern observations and modeling of stellar populations in galaxies allow us to determine the presence of a dark component to galaxies that is roughly 20 times more massive then the visible component [10, 11].

The basic idea of this method is as follows: if an object is orbiting a galaxy at a distance r from its center, it does so at a speed V such that the gravitational pull towards the galaxy provides the centripetal force to keep the object in orbit. Although a detailed mass model of the galaxy is required to reproduce the full rotation curve $V(r)$, the multipole expansion of the gravitational potential tells us that, for a distant satellite of the galaxy,

$$V^2(r) = \frac{GM}{r}, \tag{1.3}$$

M being the total mass of the galaxy. If no dark component exists, the rotation curve $V(r)$

should decay like $r^{-1/2}$ at large distances. Observations show that rotation curves are *flat* at large distances, implying a dark component that extends beyond the visible one. If this dark component is distributed isotropically, we may replace M by $M(r)$ in Eq. (1.3). The constant rotation curve ($M(r) \propto r$) then tells us that the dark component's density $\rho_{\text{dark}}(r) \propto r^{-2}$.

Historically, this observation was sharper than the one for clusters, as it gives hints not only for how much dark matter might be present in a galaxy, but also how it is distributed in galaxies. Since most of the DM mass is located on the outskirts of galaxies and its distribution extends much further out than the visible matter, it is said that DM is distributed in galactic *halos*. The ability of simulations of structure formation to reproduce this asymptotic behavior of the density profile is a seeming success of the dark matter picture [12].

1.1.2 Cosmological evidence

The "concordance model" of cosmology mentioned in the previous section assumes that the universe as a whole, at its largest scales, is spatially homogeneous and isotropic. At the largest observed scales, galaxy distributions become isotropic [13], and the observed isotropy of the cosmic wave background provides good evidence that this is a good assumption (see [14] for a review). The so called "Copernican principle", i.e the notion that we are not located at a special position in the universe, coupled with the observed isotropy, would then imply that the universe is homogeneous. In such a universe, the metric may be written as

$$\mathrm{d}s^2 = -\,\mathrm{d}t^2 + a^2(t)\left(\frac{\mathrm{d}r^2}{1 - Kr^2} + r^2\,\mathrm{d}\Omega^2\right), \tag{1.4}$$

where the constant $K \in \{-1, 0, 1\}$ discriminates between open, flat, and closed universes, respectively. This metric is known as the Friedmann-Robertson-Walker (FRW) metric.

The coordinate system defined above is called comoving: it defines the observers for which homogeneity and isotropy holds. The function $a(t)$ is a *scale factor* that determines the evolution of physical distances in terms of these comoving coordinates. The normalization of $a(t)$ is arbitrary for flat universes, which are favored by the data and will be implicitly assumed. If we then set $a(t) = 1$ at the present time, the scale factor tells us how much the universe has expanded between a time in the past and now.

Homogeneity and isotropy imply that the energy momentum tensor must be that of a perfect fluid, which is described by only two parameters: an energy density ρ and a pressure p. The strong constraints imposed on the metric simplify the Einstein equations to

$$\begin{aligned} \left(\frac{\dot{a}}{a}\right)^2 + \frac{K}{a^2} &= \frac{8\pi G}{3}\rho \\ \frac{\ddot{a}}{a} &= -\frac{4\pi G}{3}(\rho + 3p). \end{aligned} \tag{1.5}$$

We define the Hubble parameter H as $\dot{a}a^{-1}$. The *Hubble constant* H_0 is the present value of the Hubble parameter. The *critical density* is defined as that which implies $K = 0$, namely,

$$\rho_{\text{crit}} = \frac{3H^2}{8\pi G} = 8.68 \times 10^{-27}\text{kg m}^{-3}\left(\frac{H}{68\text{km s}^{-1}\text{Mpc}^{-1}}\right)^2 \tag{1.6}$$

Einstein's equations imply local conservation of energy, which, for a perfect fluid in the Friedmann universe, reads

$$\dot{\rho} + 3H(\rho + p) = 0. \tag{1.7}$$

The thermodynamic relation $T\,\mathrm{d}S = \mathrm{d}U + p\,\mathrm{d}V$, along with the above equation, implies $\dot{S} = 0$ if we take $V \propto a^3(t)$ and $S = Vs$. Note that we are abusing the notation from thermodynamics by defining s as the entropy density instead of the entropy per particle. This result shows that Eq. (1.7) is not conservation of energy but rather conservation of *entropy*. The universe's entropy density s will therefore provide a good fiducial quantity to which other densities may be normalized. Thus, when we talk about dark matter freeze-out, it will be useful to define the amount of dark matter per entropy $Y = \rho_{DM}/s$.

In the standard cosmological model, three components are assumed to contribute to the energy density: pressureless matter (non-relativistically moving particles), defined by $p = 0$; radiation (ultra-relativistically moving particles), which satisfy $p = \rho/3$; dark energy, which obeys $p = -\rho$. Dark energy, which drives the accelerated expansion of the present universe, could be generated dynamically, from the vacuum energy of some field, or it could be a fundamental cosmological constant, as allowed by general relativity (see, e.g, [15] for a discussion). The standard cosmology is at present only concerned with the dark energy equation of state and not its origin.

If only one energy component is present, Eq. (1.7) yields $\rho(t) \propto a^{-3(1+w)}$. When all three components are present, we may take them to evolve independently if they are not strongly interacting. Furthermore, the different a dependences for $\rho(t)$ imply that we can divide cosmic history in a radiation dominated period (the first $\sim$ 100kyr of the universe), a matter dominated period (until about 5Gyr ago), and a dark energy dominated period (the present universe). If one energy component overwhelms the others, the independent evolution approximation is also justified.

This picture in which the universe can be taken as a hot, relativistic fluid, cooling as it expands, and then growing structures (stars, galaxies, etc) is known as the "thermal history" of the universe. From our point of view of using cosmology to establish the existence of DM and placing constraints on models, there are 3 "major events" that happen during expansion that are worth emphasizing in our introductory discussion: nucleosynthesis, recombination, and structure formation.

Nucleosynthesis, or the formation of light nuclei in the early universe, provides a handle on the total amount of *baryons* in the universe. At very early times, weak interaction processes can efficiently convert neutrons to protons, and their abundances are similar. The total baryon density in the early universe is not very large, and nuclei can only form by two-body processes, which start with the formation of deuterium.

Deuterium, however, is very loosely bound, and the high photon-to-baryon ratio in our universe ($\sim 10^{10}$) means that photons can efficiently break it, preventing the formation of other nuclei until the universe has cooled to about 0.75MeV. Weak interactions fall out of equilibrium before this temperature is reached, and neutrons decay into protons for a time before nuclei can form. In a simplified picture, all the available neutrons then bind in ^{4}He nuclei.

Detailed nucleosynthesis calculations are much more complex, but the basic idea is that the known expansion history of the universe provides a relationship between the nuclear temperature and cosmic time, which determines how many neutrons are available to form complex nuclei. Coupled with the nuclear physics of the reactions happening in the early universe, it is then possible to predict the relative abundances of light nuclei given the baryon-to-photon ratio in the universe [8, 16]. Predicting these abundances was not only a great success of the standard cosmology, but it provided an important piece of evidence for not all of the matter in the universe being composed of baryons.

Recombination is the formation of *atoms*. It marks the transition between an ionized universe to a mostly neutral, transparent universe, in which the cool photon plasma does not significantly interact with the matter component of the universe. Those are the oldest photons that we can observe, and this transition from coupled photons to free-streaming photons defines a surface of last scattering, observed as the cosmic microwave background: an isotropic photon gas in thermal equilibrium. Detailed observations of the small anisotropies in the microwave background [17] allow a global constraint of the standard cosmology's parameter space, and its description is arguably the strongest success of our cosmological model.

The local universe, in which we observe planets, stars, galaxies, etc, is decidedly not homogeneous. Given the remarkable degree of homogeneity of the early universe, how does the rich structure that we observe form? This is a challenging problem, but a naive plan of attack would be as follows: since the standard cosmology works well at large scales, we may take the FRW metric as a "background" on which small fluctuations in the local mass content grow due to gravity. The collapse of these perturbations would then give rise to the observed structure in the universe. Once some initial data on the fluctuations is provided, numerical simulations could then be able to (statistically) reproduce the structure observed in the local universe. This means not only reproducing the distribution of stars and galaxies we observe, but also the DM halos mentioned in the previous section.

The cosmic microwave background has been observed sufficiently accurately that it may be used as initial data for cosmological density fluctuations. The temperature anisotropies $\Delta T(\hat{n})$ can be decomposed in spherical harmonics $Y_{lm}(\hat{n})$, and each mode l provides information about fluctuations at different length scales. Small l modes are large-scale fluctuations, providing information about modes that are “super-horizon” scale and would be set up, say, at inflation. Larger l modes correspond to smaller length scales, which are affected by the interactions between the different matter and radiation components of the universe.

Neither the implementation nor the interpretation of cosmological numerical simulations is straightforward. The detailed evolution of a fluctuation into a galaxy depends not only on the large scale gravitational physics but also on smaller scale physics like local interactions of baryons with radiation or even DM self-interactions, and capturing important physical effects on such disparate length scales is not straightforward. That said, modern simulations are capable of capturing such small scale effects and much progress has been made in their implementation.

Although cosmological simulations have become increasingly complex, it is not clear a priori which observables obtained from them can discriminate between cosmological models. It is true, however, that if a DM model cannot reproduce the observed structure in the universe (provided that the simulations are to be trusted), it must be ruled out. We will provide a simple analytical example of such an argument in the next section.

1.2 Dark Matter Candidates

Although cosmological observations have constrained the amount of dark matter in the universe and revealed that it is cold, not much else is known about its nature. The standard model of particle physics (SM) also has no candidate dark matter particle. In this section, we will present two distinct possibilities for what DM could be composed of, and briefly discuss how microscopic models can be linked to cosmological observables like the total dark matter density.

1.2.1 Particle Dark Matter

1.2.1.1 Generalities

Particle dark matter models make the assumption that DM is composed of some unknown particle yet to be discovered. Moreover, and more importantly, the main assumption we will make is that DM particles interact with standard model particles sufficiently strongly such that, at some point, they are in thermal equilibrium with the SM. These particles are known as *thermal relics* and, leaving aside their current distribution in halos, are parameterized by the dark matter mass m and their interaction cross section with the SM $\langle \sigma v \rangle$. Another possible parameter is the DM particle lifetime τ, if it is unstable. Observations of the cosmic microwave background put strong constraints on it, and so we will ignore that possibility. In the following discussion, we will make some order of magnitude estimates that link microscopic observables such as $\langle \sigma v \rangle$ to cosmological quantities.

The fact that thermal relics are in equilibrium with the SM means that we can link the DM density to the known thermal history of the universe [8]. Due to the expansion of the universe, interaction rates will eventually become too small to maintain equilibrium. Since there will no longer be any interconversion of DM particles and SM particles, the comoving DM density *freezes out* to an asymptotic value which must then match the observed density.

A *hot relic* decouples from the bath when it is still relativistic. It is then particularly simple to compute its final cosmological density. The DM density and the photon density will have a common temperature T at decoupling, and both of these scale like T^3. This means that the ratio $n_{\rm DM}/n_\gamma$ is given by [18]

$$\frac{n_{\rm DM}}{n_\gamma} = \frac{g_{\rm DM}}{2}\left(\frac{43/4}{g_{\rm eff,dec}}\right)\left(\frac{4}{11}\right). \tag{1.8}$$

The first factor is simply the ratio of the spin degrees of freedom of the DM (times 7/8 if DM is fermionic) to those of the photon (2). The other two factors multiplying this expression have to do with entropy conservation and increases in the photon number. As shown in [16], the entropy of the universe is dominated by its relativistic degrees of freedom (those that have $E \simeq p$). Since the photon is a relativistic particle in the aforementioned sense, we may express the entropy density of the universe as $s = g_{\rm eff} s_\gamma$, with $g_{\rm eff}$ counting the "effective number of relativistic degrees of freedom". For relativistic particles like the photon, it holds that $s_\gamma \propto n_\gamma$.

In thermal equilibrium, reactions like $e^+ + e^- \rightleftharpoons 2\gamma$ keep the e^+, e^- abundances stable, but once the temperature falls below the electron mass this is no longer the case. A typical photon pair will not have enough energy to produce two electrons, and these particles will not be replenished. They will also no longer be relativistic and will stop contributing to the entropy, meaning that $g_{\rm eff}$ goes down. To keep the entropy constant, we see that n_γ must go up by precisely the ratio $g_{\rm eff,before\ annihilation}/g_{\rm eff,after\ annihilation}$. Between the DM particle decoupling and the present, there are two such "boosts" to the photon density that must be taken into account. The first one is that all the relativistic degrees of freedom $g_{\rm eff,dec}$ will convert into only photons, electrons, positrons, and neutrinos.

In the SM, there are 3 neutrinos, each with 2 spin degrees of freedom, and electrons and positrons each have 2 spin degrees of freedom as well. Therefore, when these and photons are the relativistic degrees of freedom present, we have $g_{\rm eff} = 2 + 2 \times 2 \times 7/8 + 3 \times 2 \times 7/8 = 43/4 = 10.75$. When the entire SM is relativistic, $g_{\rm eff} = 106.75$. Later in the universe's thermal history, the neutrinos decouple from the bath entirely, but the electrons and positrons annihilate into photons. For electrons, positrons and photons, $g_{\text{eff}} = 11/2$, and so the photon number density increases by $11/4$ after $e^{\pm}$ annihilation. This takes care of all the factors in Eq. (1.8). Since we know the current photon density, we may use this to find the current DM density in units of the critical density [18]

$$\Omega_{\text{DM}} h^2 \equiv \frac{\rho_{\text{DM,today}}}{\rho_{\text{crit,today}}} \simeq \frac{115}{g_{\text{eff,dec}}} \frac{g_{\text{DM}}}{1.5} \left(\frac{m}{1\text{keV}} \right) \tag{1.9}$$

where $h = H_0/(100\text{km s}^{-1}\ \text{Mpc}^{-1})$. The observed value for $\Omega_{\text{DM}} h^2$ is ~ 0.15 [17]. Therefore, if a hot relic composes all of the dark matter, it must have a mass of around 0.1keV, although the precise value depends on when it decouples (through $g_{\text{eff,dec}}$). The fact that these particles are moving at the speed of light when they decouple, however, means that even when they become non-relativistic they can be moving sufficiently fast to escape the gravitational pull of density perturbations, preventing their collapse into, say, galaxies.

The motion of DM defines a (comoving) length scale l_{fs}, the *free streaming length*, below which density perturbations are erased. The idea is that if DM particles can move on average a distance l_{fs} away from each other as the universe expands, they can escape from an overdensity localized to that scale, effectively erasing it. Only overdensities that persist on scales $L \gtrsim l_{fs}$ can therefore grow and form structure. To estimate this scale, we will simply look at the geodesic motion of DM particles and see how far they can move between the epoch of matter domination (when perturbations begin to grow) and the present.

Geodesic motion in a matter dominated universe is simple to describe: particle momenta (i.e, those satisfying $E^2 - p^2 = m^2$) simply scale as $p \propto a^{-1}(t)$. Although we stated that our DM particles were relativistic when they decoupled, if they are to be the cold DM in the standard cosmology, they must be non-relativistic by the time the universe is matter dominated. We may therefore identify $p = mv$, and the comoving speed will be $v(t)/a(t)$. If the characteristic DM speed is $v(t_{\text{EQ}})$ at matter radiation equality, the free streaming length can be calculated as

$$l_{fs} = \int \mathrm{d}t\, \frac{v(t)}{a(t)} = 3v(t_{\mathrm{EQ}})t_{\mathrm{EQ}}^{1/3}t_0^{2/3}, \tag{1.10}$$

where we have used $a(t) = (t/t_0)^{2/3}$ for a matter dominated universe and the characteistic speed is $v(t) = v(t_{\mathrm{EQ}})(a(t_{\mathrm{EQ}})/a(t))$.

Since t_0 and t_{EQ} can be estimated, our goal is to calculate $v(t_{\mathrm{EQ}})$. To obtain it, we will use the fact that, prior to decoupling, our hot relic is relativistic. Consider, then, its phase space density $\frac{\mathrm{d}N}{\mathrm{d}^3\boldsymbol{x}\mathrm{d}^3\boldsymbol{p}}$, where $\boldsymbol{x}$ are comoving coordinates but $\boldsymbol{p}$ are physical momenta. Homogeneity and isotropy imply that this function can only depend on the magnitude of the momentum of the particle, p. We will therefore denote it by $n(p)$. The phase space volume $\mathrm{d}^3\boldsymbol{x}\,\mathrm{d}^3\boldsymbol{p}$ is dimensionless, which means that $n(p)$ must be dimensionless as well. If this distribution is characterized by a temperature T, then, on dimensional grounds, $n(p) = F(p/T)$, F being some arbitrary function. The average momentum of this distribution is then proportional to T. Since we are only interested in order of magnitude estimates, we will assume that all particles move with momentum p.

If we now assume that the DM decouples instantly at some time t_{dec} and ignore DM self interactions, the distribution $n(p)$ will evolve in time following the collisionless Boltzmann equation [19], which reads

$$\begin{aligned} \frac{\partial n(p,t)}{\partial t} - Hp\frac{\partial n(p,t)}{\partial p} &= 0, \\ n(p, t_{\mathrm{dec}}) &= F\left(\frac{p}{T_{\mathrm{dec}}}\right). \end{aligned} \tag{1.11}$$

By inspection, we can verify that the general solution to this equation is any function $g(a(t)p)$. Enforcing the initial conditions, we find

$$\begin{aligned} n(p,t_{\rm dec}) &= F\left(\frac{p}{T_{\rm dec}}\right) = g(a_{\rm dec}p), \\ n(p,t) = g(a(t)p) &= g\left(a_{\rm dec}\frac{a(t)p}{a_{\rm dec}}\right) = F\left(\frac{p}{T_{\rm dec}\left(\frac{a_{\rm dec}}{a(t)}\right)}\right). \end{aligned} \tag{1.12}$$

As expected, the typical momentum of the DM scales as a^{-1}. Rather than using the (unknown) decoupling temperature to scale our momenta, we will use a temperature $T_{\rm NR}$ that marks the transition between the relativistic and the non-relativistic regime. Therefore, our typical momentum will be $T_{\rm NR}a_{\rm NR}/a(t)$. This temperature is only loosely defined, but the value $T_{\rm NR} \simeq m/3$ is used in the literature [18, 20]. What this means is that we may use the Stefan-Boltzmann law for the DM density, $\rho_{\rm DM}(T_{\rm NR}) = \frac{\pi^2}{30}g_{\rm DM}T_{\rm NR}^4$, but still redshift the DM as pressureless matter, i.e, $\rho_{\rm DM}(T_{\rm NR}) = \rho_{\rm DM,today}a_{\rm NR}^{-3}$. This gives us the value of $a_{\rm NR}$ in terms of m and the observed DM density. Using the known value of $a_{\rm EQ}$ then gives [18]

$$v(a) \sim 0.012a^{-1}\left(\frac{\Omega_{\rm DM}h^2}{0.15}\right)^{1/3}\left(\frac{1.5}{g_{\rm DM}}\right)^{1/3}\left(\frac{1{\rm keV}}{m}\right)^{4/3}{\rm km/s}. \tag{1.13}$$

The mass inside a sphere of comoving length l_{fs} is then

$$M_{fs} = \frac{4\pi}{3}\rho_{\rm DM,today}l_{fs}^3 \simeq 8\times 10^8 M_\odot\left(\frac{\Omega_{\rm DM}h^2}{0.15}\right)\left(\frac{1.5}{g_{\rm DM}}\right)\left(\frac{1{\rm keV}}{m}\right)^4. \tag{1.14}$$

The meaning of M_{fs} is that structures having mass $M < M_{fs}$ will not form. The smallest structures made primarily of DM that we can observe have a mass of about $10^8 M_\odot$, which implies that DM particles must be heavier than about 0.6keV, if we set $M_{fs} = 10^8 M_\odot$. Note that Eq. (1.9) would then imply $\Omega_{\rm DM}h^2 \simeq 0.6$, contradicting observations. This means that DM particles in this mass range must have their relic density set by some other mechanism.

These types of bounds on hot thermal relics have led to the dominant hypothesis on particle DM to be that it is a *cold relic*. Cold relics decouple from the SM thermal bath when they are non-relativistic, and are generally taken to be in the mass range of a few

GeV-TeV. The calculation of their relic density is not as straightforward and depends on the details of their interactions with the SM [21]. This is because non-relativistic particles in thermal equilibrium have their abundances exponentially suppressed by a Boltzmann factor, $n \propto e^{-m/T}$ [16]. Thus, the relic density is sensitive to the decoupling temperature, which is set by DM interactions.

The picture, then, is that at early times the DM is in equilibrium with the SM. As the universe expands and cools, eventually the temperature will fall below the DM mass m, and DM particles that annihilate will not be replenished, since the SM bath does not have enough energy to produce them. This does not mean that all the DM will disappear: since the universe is expanding, the annihilation rate for DM+DM→SM+SM will decrease, and DM particles will stop annihilating altogether. At this point, the DM density *freezes out.*

The evolution from being slightly out of equilibrium to freezing out completely can be described by the following differential equation for $n(t)$ [19]

$$\frac{\mathrm{d}n}{\mathrm{d}t} + 3Hn = -\langle \sigma v \rangle \Big(n^2 - n_{eq}^2 \Big), \tag{1.15}$$

n_{eq} being the number density of DM in thermal equilibrium and $\langle \sigma v \rangle$ the thermally averaged cross section for the process DM+DM→ SM+SM. The left hand side of this equation may be understood as the dilution of particles due to the expansion of the universe, and the right hand side represents the interaction processes that change the number of DM particles by annihilation or production from the thermal bath of SM particles.

Since the DM is non-relativistic, a power series expansion of $\langle \sigma v \rangle$ in terms of the characteristic DM speeds v is appropriate. To simplify the calculation, we will assume that the DM annihilation proceeds through an s-wave process, therefore having a $\langle \sigma v \rangle$ that is independent of v and, consequently, of the temperature. Rather than considering the evolution of the DM density with cosmic time, it is useful to use entropy conservation to consider the evolution of the variable $Y = n/s$ with respect to the temperature of the microwave background. If the DM particle has mass m, we further introduce $x = m/T$ to obtain

$$\frac{\mathrm{d}Y}{\mathrm{d}x} = -\frac{\langle\sigma v\rangle s}{Hx}\Big(Y^2 - Y_{eq}^2\Big). \tag{1.16}$$

We now define $\Delta = Y - Y_{eq}$ and assume that the particle is non-relativistic so that $Y_{eq} \propto x^{3/2}e^{-x}$ [16]. Going through with the algebra leads to

$$\begin{aligned}\frac{\mathrm{d}\Delta}{\mathrm{d}x} &= -\frac{\mathrm{d}Y_{eq}}{\mathrm{d}x} - f(x)\Delta(2Y_{eq} + \Delta),\\ f(x) &\equiv \sqrt{\frac{\pi g_{\mathrm{eff}}}{45}}\frac{m\langle\sigma v\rangle}{G^2x^2}.\end{aligned} \tag{1.17}$$

Our expectations regarding the physics of this process lead us to define a transition temperature T_f, the *freeze-out temperature*, and a corresponding variable x_f. For $x \ll x_f$, departures from equilibrium should be small and thus we will set $\Delta \ll Y_{eq}$ and $\Delta' = 0$, so $\Delta \simeq -Y'_{eq}/2f(x)Y_{eq}$. On the opposite limit, with $x \gg x_f$, the departure from equilibrium is large and $\Delta \gg Y_{eq}$, leading to $\frac{\mathrm{d}\Delta}{\mathrm{d}x} = -f(x)\Delta^2$. In this region, particle creation has been Boltzmann-suppressed since the SM particles do not have enough energy to create DM particles, but annihilations are still important. Integrating from x_f to infinity gives

$$\frac{1}{\Delta_\infty} - \frac{1}{\Delta_f} = \sqrt{\frac{\pi g_*}{45}}\frac{m\langle\sigma v\rangle}{G^2x_f}. \tag{1.18}$$

Two approximations may now be made: $\Delta_\infty \simeq Y_\infty$, since $Y_\infty \gg Y_{eq}$ (Y_{eq} is exponentially suppressed, while Y is freezing out), and $Y_\infty^{-1} \gg \Delta_f^{-1}$. This last approximation comes from the physical fact that annihilations will still be important for sometime after freeze-out, leading the abundance of DM to be suppressed from that at freeze-out. Using the definition of Y and $\rho_{DM} = mn$, we now find [21]

$$\Omega_{DM}h^2 = \frac{3\times10^{-27}\mathrm{cm}^3\mathrm{s}^{-1}}{\langle\sigma v\rangle} = \frac{2.5\times10^{-10}\mathrm{GeV}^{-2}}{\langle\sigma v\rangle}, \tag{1.19}$$

The cross-section required to get the observed relic abundance is in the order of magnitude of what is expected of weak-scale processes, and it motivated the search for DM particles in the GeV-TeV mass scale with weak-scale couplings, known as weakly interacting massive particles (WIMPs). Such particles would become non-relativistic early in the history of the universe, fitting nicely with the cold DM paradigm that is obtained from cosmology. Moreover, heavy particles with order weak-scale couplings arise naturally in supersymmetry (SUSY), which has been a popular theoretical model for extending the SM.

Supersymmetry's popularity stems from a few reasons: its non-renormalization theorem allows it to solve the *hierarchy problem* coming from the separation of scales between the higgs boson mass and the scales at which we expect the SM to require completion, say, from quantum gravity. This scale separation is not radiatively stable [22], so if we envision the SM as an effective field theory, some mechanism is necessary to make sure that the higgs mass has the proper value. As mentioned previously, SUSY introduces natural candidates for the DM. In the context of grand unification, SUSY is also popular as the SM gauge couplings come closer to having a common value at high energy scales in models with SUSY than in those without.

1.2.1.2 Supersymmetry

In Chapter 3, we will show how specific models of particle dark matter can be constrained in the context of SUSY. Thus, we introduce some of the basic language in this section.

A *supersymmetry* is a hypothetical correspondence between a fermionic and a bosonic particle. If our universe had unbroken supersymmetry, every fermion of the SM, such as the electron, would have a scalar partner. These are generally referred to as *sfermions*: squarks, sleptons, sneutrinos. Gauge bosons would have spin 1/2 partners named *gauginos*: photino, gluino, wino, and bino. The *superpartner* of the higgs boson is named the higgsino. Formally, a supersymmetry is a continuous symmetry of the S-matrix [23]. Since this transformation is continuous, it may be described by infinitesimal generators satisfying certain algebraic relations.

Since supersymmetry transformations map a bosonic degree of freedom into a fermionic one, and vice-versa, the supersymmetry generators must have angular momentum and, therefore, transform non-trivially under the Lorentz group. The transformations are generated by a pair of spin 1/2 operators $Q_\alpha, Q^\dagger_{\dot\alpha}$, where undotted(dotted) indices indicate left(right)-handed spinors [24], which satisfy the following algebraic relations

$$\begin{gathered}\left\{Q_\alpha, Q^\dagger_{\dot\alpha}\right\} = -2\sigma^\mu_{\alpha\dot\alpha} P_\mu,\ \{Q_\alpha, Q_\beta\} = 0,\ \left\{Q^\dagger_{\dot\alpha}, Q^\dagger_{\dot\beta}\right\} = 0 \\ [Q_\alpha, P^\mu] = 0,\ \left[Q^\dagger_{\dot\alpha}, P^\mu\right] = 0, [Q_\alpha, J^{\mu\nu}] = \frac{i}{4}(\sigma^\mu\bar\sigma^\nu - \sigma^\nu\bar\sigma^\mu)_\alpha^{\ \beta} Q_\beta \\ \left[Q^\dagger_{\dot\alpha}, J^{\mu\nu}\right] = -\frac{i}{4}(\bar\sigma^\nu\sigma^\mu - \bar\sigma^\mu\sigma^\nu)^{\dot\beta}_{\ \dot\alpha} Q^\dagger_{\dot\beta}\end{gathered} \tag{1.20}$$

with $\sigma^\mu = (I, \boldsymbol{\sigma})$ and $\bar\sigma^\mu = (I, -\boldsymbol{\sigma})$. This supersymmetry algebra, which is not the most general one, is known as $\mathcal{N} = 1$ SUSY. Supersymmetry transformations can be represented as translations in *superspace*, an extension of spacetime with extra fermionic coordinates $\theta_\alpha, \theta^\dagger_{\dot\alpha}$ [25]. To construct a field theory in superspace, one proceeds much like in the case of a regular field theory: the "elementary" degrees of freedom are the ones that that transform irreducibly under supersymmetry, and additional internal symmetries, like gauge symmetries, may be imposed in the lagrangian.

Once this is done, the action can be written as the integral of a superspace lagrangian $S = \int \mathrm{d}^4x\, \mathrm{d}^2\theta\, \mathrm{d}^2\theta^\dagger\, \mathfrak{L}(x, \theta, \theta^\dagger)$. The fermionic integrals immediately lead to the usual four-dimensional lagrangian for the particle degrees of freedom contained in the supermultiplets. To construct the simplest supersymmetric extensions of the SM, two types of supermultiplets are necessary: the *chiral supermultiplet*, which consists of a complex scalar and a Weyl fermion, and the *vector supermultiplet*, comprised of a Weyl fermion and a massless vector. Note that these degrees of freedom correspond to those of massless particles. Except for the Higgs field, the SM Lagrangian is built up from massless particles, electroweak symmetry breaking being required for mass generation. Usage of these supermultiplets is therefore consistent with how we think of the SM "prior" to electroweak symmetry breaking.

In the Minimal Supersymmetric Standard Model (MSSM), the left-handed doublets such as the lepton multiplet (ν_L, e_L) become a doublet of chiral supermultiplets, and the right handed e_R become part of a *different* chiral supermultiplet. Thus, each lepton family in the MSSM is accompanied by three new complex scalars, and each quark family is accompanied by four. This is necessary for the superpartners of the SM particles to have the same number of degrees of freedom as the SM fermions: the doublet (ν_L, e_L) has four degrees of freedom, and the singlet e_R has two. Each complex field has two components, and that matches the fermions degrees of freedom.

In a sense, then, the charged leptons of the SM have *two* superpartners, but this is only because we think of the SM fermions in terms of their Dirac spinors and not in terms of the "more fundamental" chiral structure.

Supersymmetric models have been extensively studied phenomenologically both from the particle physics and the cosmology sides. In our work, we will consider one of many theoretical constraints, vacuum stability, in a region of supersymmetric parameter space that was experimentally motivated [26]. The problem of vacuum stability may be stated as follows: in a theory with several scalar fields ϕ_i, the hamiltonian contains a potential $V(\phi_i)$ that may have several extrema. If the fields are not varying spatially, as should be expected in a homogeneous universe, the ground state of our theory (the vacuum state) corresponds to the global minimum of this potential. The values ϕ_i of the fields at the vacuum state are known as vacuum expectation values. In the SM, the W and Z fields obtain their masses from the vacuum state of the higgs field not being the trivial $h = 0$ state. More explicitly, if we introduce a higgs field that transforms in the doublet representation of the $\mathrm{SU}(2)_L$ group of the SM, the lagrangian contains the terms

$$L_{\text{higgs}} = (D_\alpha H)^\dagger D^\alpha H + \mu^2 H^\dagger H - \lambda \Big(H^\dagger H\Big)^2, \tag{1.21}$$

$$D_\alpha = \partial_\alpha - ig\frac{\sigma_i}{2}W^i_\alpha - \frac{ig'}{2}B_\alpha, \quad H = \begin{pmatrix} H^+ \\ H^0 \end{pmatrix}, \tag{1.22}$$

where W^i, B are the gauge bosons of the SU$(2)_L$ and U$(1)_Y$ groups, respectively. The W bosons are $(W^1 \pm iW^2)/\sqrt{2}$, and the photon and Z boson are the fields

$$\begin{aligned} A_\alpha &= \cos\theta_W B_\alpha + \sin\theta_W W^3_\alpha \\ Z_\alpha &= -\sin\theta_W B_\alpha + \cos\theta_W W^3_\alpha, \end{aligned} \tag{1.23}$$

with θ_W the Weinberg angle such that $\tan\theta_W = g'/g$. From the lagrangian, we see that the higgs potential is $V(H) = -\mu^2|H|^2 + \lambda|H|^4$, which has a non-trivial minimum at $|H| = \mu/\sqrt{2\lambda} \equiv v/\sqrt{2}$. Using the gauge symmetry of the theory, we can choose our vacuum state to have a zero "spin-up" component and a purely "spin-down" component. Evaluating the covariant derivatives in L_{higgs} at this minimum gives

$$H = \frac{1}{\sqrt{2}}\begin{pmatrix} 0 \\ v \end{pmatrix} \Rightarrow L_{\text{Higgs}} = \frac{1}{2}\Big(\frac{gv}{2}\Big)^2 W^\dagger_\alpha W^\alpha + \frac{1}{2}\Bigg(\frac{\sqrt{g^2+g'^2}v}{2}\Bigg)^2 Z_\alpha Z^\alpha + \text{constant}. \tag{1.24}$$

These quadratic terms in L_{higgs} are masses for the W and Z bosons, and we see that the photon field remains massless. Furthermore, the Fermi constant, which can be measured in nuclear processes involving beta decay, is uniquely determined by v as $G_F = 1/(\sqrt{2}v^2)$. We see that the vacuum structure of the SM is linked to observable quantities, and its determination is therefore more than just an academic exercise.

This tight link between vacuum expectation values and observable quantities allows to understand why the introduction of more scalar fields, as in the case of SUSY, can be problematic. The scalar potential, which is quartic in the fields, can now have many minima other than the one with $|H| = v/\sqrt{2}$. It may be the case that one of these potential minima in the now multidimensional field space has a lower energy than the minimum in which the W and Z bosons have their correct masses. This is not acceptable because, as the universe cools during its expansion, the fields in the theory should settle down to their vacuum state. It is therefore necessary that the vacuum state describe the physics we observe.

Investigating vacuum stability in supersymmetry is a non-trivial task due to the presence of several scalar fields. We will therefore make several simplifying assumptions to reduce our problem. If any colored or charged particles acquire a vacuum expectation value, this would break the $SU(3)$ and $U(1)$ symmetries of the SM, violating color and charge conservation. We will therefore assume that the charged sfermions do not acquire an expectation value. We will also impose that the sneutrinos do not acquire a VEV, and thus we will restrict our analysis to the higgs sector.

The higgs sector of the MSSM contains two higgs doublets due to holomorphicity requirements of the superpotential function, which determines the fermionic mass matrices of the theory [25]. This means that the lagrangian terms $\overline{\Psi}_L(i\sigma_2 H^*)\Psi_R + \text{h.c.}$ that are used in the quark mass matrix will not be allowed, since the complex conjugate of a field is present. With two higgs doublets, defined as

$$H_u = \begin{pmatrix} h_u^+ \\ h_u \end{pmatrix}, \quad H_d = \begin{pmatrix} h_d \\ h_d^- \end{pmatrix}, \tag{1.25}$$

SUSY models now have at least twice as many higgs degrees of freedom as the SM. As in the case of the SM, electroweak symmetry breaking implies that 3 of these (say, the charged and pseudoscalar components of H_d) "go into" the longitudinal degrees of freedom of the W and Z bosons. We are still left with 5 degrees of freedom: two neutral scalars h_u, h_d, a charged component $H^\pm$, and a pseudoscalar component denoted as A^0. None of these are usually taken to get vacuum expectation values: $H^\pm$ violates charge conservation, and A^0 violates CP. The scalar potential of the MSSM is therefore taken to be a function $V(h_u, h_d)$.

In Chapter 3, we will consider the vacuum stability of the Next-to-Minimal Supersymmetric Standar Model (NMSSM), which adds one scalar supermultiplet to the MSSM. The scalar in this supermultiplet will be allowed to obtain an expectation value, making our problem three dimensional. There, we will deal not only with the higher dimensionality of the problem, but also with radiative corrections, which make the potential non-polynomial and introduce challenges in identifying all extrema.

1.2.2 Primordial Black Holes

In the standard cosmological model, the structures that we observe in the universe like galaxies, clusters, and superclusters, form from the gravitational collapse of primordial density fluctuations. This structure formation is *hierarchical*: smaller scales collapse first, and then larger structures are formed from smaller ones.

Within this context, it is natural to ask if a given perturbation could collapse all the way down to a black hole. Provided that a density fluctuation is large enough, the answer is affirmative [27]. The black holes formed through this mechanism are a particular case of what is known as a primordial black hole (PBH), a black hole formed in the early universe, not originating from stellar evolution. There are many different ways in which PBHs can form: see, for instance, [28] for a proposal linking PBHs and axions. To get an idea for how such a black hole might be formed and what mass it may have, we will focus on the idea of a collapsing overdensity, as that is the simplest formation process.

The basic idea is to study a perturbation on scales that are larger than the Hubble horizon size (any given perturbation satisfies this at some point in time [29]). Causal processes do not act on regions larger than the horizon, and this perturbed region may therefore be modeled as a separate, closed universe. We will not question how these perturbations are set up, although we point out that inflationary models can account for them [30]. As we will see, these perturbations grow in time. However, once the universe has expanded sufficiently so that causal processes can act on scales of the size of the perturbation, we must consider mechanisms that prevent the overdensity from collapsing, like pressure support. This effectively defines a Jeans length [31] Λ_J, and only perturbations in scales $L > \Lambda_J$ collapse. As we will show, this implies a lower bound on the overdensities that can form PBHs.

The separate universe's expansion is given by the Friedmann equation with curvature

$$H^2 + \frac{K}{a^2} = \frac{8\pi G}{3}\rho, \tag{1.26}$$

ρ being the total density. At this point, we must make a choice: the scale factor for a closed universe has dimensions of length, whereas that for an open universe is dimensionless. Ultimately, all that matters is that K/a^2 has the correct units, so instead of taking $K = 1$ as is usally done for a closed universe, we will take the curvature to be dimensionful and keep a dimensionless. This also emphasizes that the induced curvature in the overdense region is a perturbation, as we will see that it can be linked to the density contrast $\delta \equiv (\rho - \bar{\rho})/\bar{\rho}$, $\bar{\rho}$ being the density in the unperturbed region. To forge this link, assume that at some time H^2 is equal in the perturbed and unperturbed regions, and that their scale factors are similar [29]. Using the Friedmann equation for the unperturbed universe then gives.

$$\delta = \frac{K}{a^2 H^2_{\text{unperturbed}}}. \tag{1.27}$$

Since $H^2 \sim a^{-4}$ in the radiation dominated epoch, we see that the density contrast grows as the universe expands. A positive curvature Friedmann universe begins collapsing when $K/a^2 = 8\pi G\rho/3$. Substituting K/a^2 for δ, we see that this corresponds to $\delta = 1$. For this perturbation to actually collapse, however, it must not be erased by the pressure. This means that the overdensity must extend to length scales larger than the Jeans length of the universe at the time collapse begins (when $\delta = 1$). The Jeans length may be estimated classically by comparing the time a pressure wave with speed c_s moves through a system of length Λ, t_{pres}, with the time it would take for the a particle at the edge of this system to freely fall to its center, t_{fall}. We may estimate $t_{\text{pres}} = \Lambda/c_s$, and $t_{\text{fall}} \simeq (G\rho)^{-1/2} \simeq H^{-1}$. For the fluctuation to collapse, we then require $t_{\text{fall}} > t_{\text{pres}} \Rightarrow \Lambda > \Lambda_J = c_s H^{-1}$. In the radiation dominated era, $c_s^2 = 1/3$.

To connect this with the density power spectrum (loosely defined here as the Fourier transform of the density contrast), consider the fluctuation δ as having an associated co-moving momentum scale k. The physical length scale associated with k is $a(t)/k$. In order for the collapse to happen, this length scale must be greater than the Jeans length of the background universe $c_s H^{-1}$. If the physical length scale is equal to the Jeans length *and* has $\delta = 1$ at the collapse time t_c, we find

$$c_s^2 k^2 = H^2 a^2(t_c) = K. \tag{1.28}$$

This gives us the condition for the PBH to be formed. This can be translated into a requirement on the fluctuation δ when the length scale $a(t)/k$ crosses the horizon at the time t_k such that $a(t_k)/k = H^{-1}$. Using Eq. (1.27), we find

$$\delta(k, t_k) = \frac{K}{H^2 a^2} = \frac{c_s^2 k^2}{H^2 a^2} = c_s^2. \tag{1.29}$$

Therefore, perturbations with $\delta(k, t_k) > c_s^2$ collapse into PBHs. This condition is more useful since, if a model for the density perturbations is given, we now know exactly which (and how many, if we have the distribution of fluctuations) overdensities will form black holes. This picture also gives us an idea of the mass of the BHs that are formed. Since the fluctuations must persist on length scales of order H^{-1}, the particle horizon size, the mass of the PBHs will be of order the horizon mass

$$M_{\text{PBH}} \sim 10^{15} g \Big(\frac{t}{10^{-23} s} \Big) \sim 10^5 M_\odot \Big(\frac{t}{1 s} \Big). \tag{1.30}$$

We see from the above equation that by tuning the formation time of the PBHs, they can be produced with any mass. In particular, LIGO observations of black hole mergers from BHs with masses of $\sim 30 M_\odot$ raised the possibility that these may be primordial [32]. This is because, although these large masses are not impossible to obtain from stellar evolution, they are rare. An appealing hypothesis, then, given the several null results of experiments trying to detect particle DM, is that these BHs are both primordial and compose the dark matter in the universe.

One problem with this idea is that observations of the microwave background show temperature fluctuations on the order of $\Delta T/T \propto \Delta\rho/\rho \sim 10^{-5}$. If the fluctuation spectrum is scale invariant, which is motivated by the simplest inflation models, as well as gaussianly distributed, large density contrasts $\sim 1/3$ will be exceedingly rare. That said, it is possible to construct models that are experimentally viable and achieve this [30].

Currently, there are a variety of experimental constraints on the fraction of DM that is allowed to be PBHs as a function of the PBH mass. These comprise a wide variety of physical phenomena, such as contributions to background radiation from Hawking evaporation and disruption of binary stellar systems from three-body encounters. Such constraints typically assume a monochromatic black hole mass spectrum, and they rule out primordial black holes as being 100% of the DM. The situation is less clear-cut, however, if one assumes an extended mass spectrum. Even if PBHs are not all of DM, their existence could still alleviate some of the problems with structure formation in the standard cosmology [33].

1.2.3 Caveats

In the previous two sections we presented two very distinct candidates for the composition of DM. That such large uncertainties are present as far as the mass scales and interactions of DM particles are concerned stems from the fact that, as soon as the assumption of thermal equilibrium is dropped, many of the constraints from cosmology can be evaded.

For instance, the free-streaming length for light particles that are in thermal equilibrium with the SM seems to put a strong lower bound on the particle mass. However, the information that this truly provides is that the dark matter is cold. This means that particles that are *not* in thermal equilibrium with the SM can evade this bound by becoming non-relativistic in another way. As an example that has received theoretical attention recently, a scalar field can behave as pressureless matter regardless of the mass of its quanta. To see this, let's consider the lagrangian for a free scalar

$$L = -\frac{1}{2}\partial^\mu\phi\partial_\mu\phi - \frac{1}{2}m^2\phi^2. \tag{1.31}$$

The energy momentum tensor of this field is given by $T^{\mu\nu} = \partial^\mu\phi\partial^\nu\phi + g^{\mu\nu}L$. If we assume the field to be homogeneous, $\partial_i\phi = 0$, we obtain the energy-momentum tensor of a perfect fluid, with density and pressure given by

$$\rho = \frac{1}{2}\dot{\phi}^2 + \frac{1}{2}m^2\phi^2; \quad p = \frac{1}{2}\dot{\phi}^2 - \frac{1}{2}m^2\phi^2. \tag{1.32}$$

In the FRW metric, the Euler-lagrange equation [15] for the homogeneous field reads

$$\begin{aligned} \nabla_\mu\left(\frac{\partial L}{\partial\phi_{,\mu}}\right) &= \frac{\partial L}{\partial\phi} \\ \Rightarrow \ddot{\phi} + 3H\dot{\phi} + m^2\phi &= 0, \end{aligned} \tag{1.33}$$

with ∇_μ the covariant derivative and $\phi_{,\mu} = \partial_\mu\phi$. A homogeneous scalar field therefore evolves like a damped harmonic oscillator. During both the matter dominated and radiation dominated eras, the Hubble parameter satisfies $H = bt^{-1}$. In this case, the differential equation is a modified Bessel equation, with the explicit solution

$$\begin{aligned} \phi(t) =&(mt)^{(1-3b)/2}\Big(c_1 J_{(1-3b)/2}(mt) + c_2 Y_{(1-3b)/2}(mt)\Big) \\ \sim& \frac{\phi_0}{(mt)^{-3b/2}}\cos(mt-\varphi), mt \gg 1 \end{aligned} \tag{1.34}$$

where φ is a phase. The late time evolution of the field is therefore quite simple and, to leading order, the energy density scales as t^{-3b}. From the definition of H, $H = bt^{-1}$ implies $a \propto t^b$. Therefore, the energy density of this field scales as a^{-3}, as expected of cold DM. Furthermore, the pressure is proportional to $\cos(2mt)$ to leading order. Since $mt \gg 1$ at late times, it is reasonable to average the pressure over a period of oscillation of the field, $\tau = m^{-1}$, which implies that the observed averaged pressure is zero. Again, this is just as expected of cold DM. To get a feeling for what "late time" means ($t \gg m^{-1}$), we note that m^{-1} is 1s for a mass $m = 4.5 \times 10^{-15} eV$. Only for an exceedingly light particle, then, would we not satisfy the condition $t \gg m^{-1}$ in cosmological timescales.

This is an example of a (rather contrived) way to have a DM particle that is light but still behaves like pressureless matter in cosmological scales. There are many subtleties that we are overlooking here, such as the appropriateness of the classical description or how the initial value of the field could be set up such that the current energy density corresponds to the observed value of the DM density. However, we point out that in realistic axion models physical processes similar to the one described here are at play and these difficulties can be overcome, making axions a viable dark matter candidate [34, 35]. The point of this discussion is simply to emphasize that there is still much that is not known about the nature of DM and the cosmological data avaiable can still be explained by a wide variety of models.

1.3 Supermassive Black Holes at the Centers of Galaxies

It is currently accepted that most galaxies contain a black hole at their center. The history of these detections dates to the discovery of the first quasars (see [36] for a review) that had spectral variability on timescales of days or weeks. These timescales imply that these objects must be at most light-day or light-week sized (1 light day $\sim 10^{-3}$ pc). Early attempts at model building (see [37] for an early review and derivation of accretion efficiencies) quickly converged on models of galactic nuclei being powered by very massive black holes. Models of accretion and direct observation of the nuclear regions of nearby galaxies have somewhat confirmed these expectations.

For nearby galaxies, the observational goal is mostly straightforward. A point-like newtonian mass M generates a potential $\Phi(r) = -GM/r$, and the only velocity scale present in this problem is $v_c = \sqrt{GM/r}$. Thus, direct observation of stellar or gas dynamics in the nuclear region of a galaxy can reveal the presence of a black hole if a "keplerian rise" $v \propto r^{-1/2}$ is revealed in the data. This is seemingly simple until it is realized how small most black holes are in the scale of galaxies. The Schwarzschild radius of a spherical black hole of mass M is given by

$$r_s = 2GM = 1.98 \times 10^{-7}\text{pc}\left(\frac{M}{4 \times 10^6 M_\odot}\right). \tag{1.35}$$

For reference, the OSIRIS camera at Keck observatory can only resolve distance scales of about 7×10^{-4}pc. This means that galactic black holes are not resolvable by telescopes, and must be detected indirectly. That said, due to the black hole's immense mass, its gravitational effects are still important at a scale $r_h > r_s$, known as the black hole's *influence radius.* Using the above ideas of $v^2 \propto M/r$, r_h is defined as

$$r_h = \frac{GM}{\sigma^2}, \tag{1.36}$$

where σ is the velocity dispersion observed for a population of stars, gas, etc.

Ignoring radial components to the velocity, $\sigma^2 \simeq 2v_c^2$, so we see that the radius of influence roughly defines the distance at which the enclosed mass is twice the black hole mass. For the black hole at the center of our galaxy, $r_h \simeq 2$pc, meaning that the influence radius of the central black hole is very well resolved. In fact, a complete orbit of a star around the central mass has been observed, which has provided a very precise estimate of M for the Milky Way's central black hole [38].

In nearby galaxies, where individual orbits cannot be tracked but stellar motions can still be measured, the velocity profile measured, say, by the Doppler broadening of emission lines, can still be used to model the presence of a black hole [36]. For spherically symmetric systems, the Jeans equation [31] gives

$$GM(r) = v_c^2 r + \sigma_r^2 r \left[-\frac{\mathrm{d}\log\rho}{\mathrm{d}\log r} - \frac{\mathrm{d}\log\sigma_r^2}{\mathrm{d}\log r} - \left(2 - \frac{\sigma_t^2}{\sigma_r^2}\right)\right]. \tag{1.37}$$

In the above equation, $M(r)$ is the enclosed mass a distance r from the center of the galaxy, v_c is the circular velocity, ρ is the density of the observed population, and σ_r, σ_t are the radial and tangential components of the velocity dispersion. If it is possible to observationally determine all of the terms in the previous equation, then a model for $M(r)$ can be constructed and a black hole might be detected by looking at the limit of $M(r)$ for small r. If one assumes that the velocity distribution is completely isotropic, then the tangential velocity dispersion satisfies $\sigma_t^2 = 2\sigma_r^2$, and the above equation simplifies. Furthermore, only one component of the velocity need be observed, and the line of sight velocity dispersion can be obtained by looking at how stellar light is doppler shifted. This was used early on to establish evidence for an SMBH at the center of M87 [39]. More recently, models that drop the assumption of spherical symmetry have been developed that generalize these ideas and provide mass models for galaxies, also being able to detect the presence of SMBHs [40]. Currently, SMBHs in the mass range $(10^6 - 10^{10})M_\odot$ have been detected.

For distant galaxies, where r_h cannot be observed, even more assumptions are necessary to derive a black hole mass. A typical method is reverberation mapping [41], which uses the idea that galactic nuclei are powered by accretion to link correlations in the continuum emission from the nuclear region —which should come from the accretion disk —to variations in broad line emission from surrounding cooler gas. Using these correlations to estimate the size of the broad line region, and further assuming that it is virialized, allows for an estimate of the mass of the black hole once velocity dispersions are obtained from Doppler widths.

Such a wealth of observations has revealed correlations between properties of the central black hole and the host galaxy, such as the relation between black hole mass and velocity dispersion determined in [42]. These have led to the idea that central black holes evolve jointly with their host galaxies. This is still a topic in which active research is being made, and this thesis only intercepts that in the sense that we will be investigating a potential connection between central black holes and their surrounding DM halos.

1.4 Adiabatic Density Cusps Around Black Holes

Although the formation of galactic black holes is not completely understood, estimates of the timescales for its growth [43] imply that supermassive black holes (SMBH) of mass similar to that of the one at the center of the Milky Way could be formed in 10^7 to 10^8 years. Taking a DM velocity dispersion of $\sim$ 30km/s in the central region, which is about 2pc in size, we see that orbital timescales are much smaller than the timescales in which the SMBH is growing. Thus, we may consider that the SMBH grows *adiabatically*, and particle orbits can instantaneously adjust to the growing SMBH mass.

As first explored by Peebles [44], this slow growth of the black hole meant that even an initially cored profile with a finite central density could evolve into a singular density cusp after the growth of the black hole. The resulting density cusp was first considered as a way to identify the presence of a black hole at the center of a galaxy or globular cluster through its influence in the surrounding stellar population.

Peebles argued that density cusps could be identified as point sources in photographs of increasingly shorter exposure of galaxies, and, in the absence of a signal, one could constrain a central mass by the camera's ability to resolve the black hole's radius of influence. Quantitavely, what was shown was that a central stellar core would be turned into a cusp with slope 3/2, a result later strengthened by Young [45] in a self-consistent calculation.

The presence of a cusp, however, is not enough to identify the presence of a black hole. There are self-consistent density profiles that have density cusps and can be supported by a collisionless system, for instance those that are parameterized by the Zhao functional form [46]

$$\rho(r) = \rho_0 \left(\frac{R_0}{r}\right)^{\gamma} \left[\frac{1 + (R_0/a)^{\alpha}}{1 + (r/a)^{\alpha}}\right]^{(\beta-\gamma)/\alpha}. \tag{1.38}$$

As was pointed out by Quinlan *et al.* [47], these cusps can be dramatically enhanced in the presence of a slowly growing black hole, and it is difficult to observationally disentangle the origin of the cusp. Although the influence of a central BH in a stellar population might be hard to pinpoint, Gondolo and Silk [1] (GS) argued that its impact on the surrounding *dark matter* could be detected if DM particles interact with the SM.

That is because the observed flux of energetic particles such as gamma rays produced from these interactions scales with $\int \rho^2 \, \mathrm{d}s$, where the integral is done over our line of sight to an observation point. Therefore, if DM particles can annihilate into SM particles, the presence of the spike would give rise to an observable particle flux that could not be explained by the surrounding stellar population. If the profiles obtained from simulations (which work only at large distances from the center of the galaxy) are to be trusted, then we can expect the DM halo to be described by the Navarro, Frenk, White (NFW) profile [12], obtained by setting $(\alpha, \beta, \gamma) = (1, 3, 1)$ in Eq. (1.38). This "cuspy" profile ($\rho \propto r^{-1}$ as $r \to 0$) becomes even cuspier if adiabatic growth holds ($\rho \propto r^{-2.33}$), which would make the GC a bright point source for gamma rays.

The GS spike produces annihilation fluxes that are dominated by regions having a size of a few tenths of the central BH's gravitational radius [1, 48]. This makes these spikes sensitive to the effects of general relativity (GR), which is the main focus of this thesis. It must be pointed out, however, that the GS spike is very fragile, and its presence corresponds to the most optimistic scenario in which we could observe DM annihilations.

This is because, as explained in [47], the presence of an adiabatic spike hinges on an abundance of cold orbits that are deeply bound to the black hole. Any disturbances, such as mergers [49], scattering from stars [50], or an initially off-center seed black hole [43] can kick out these cold particles and prevent the spike from being formed. In particular, the original GS application to our galactic center (GC) has already been ruled out by current observation [51], as the spike profile that would be consistent with other data would be too bright. Although some of our motivation originated in the application to the GC, most of the corrections that we will calculate here can be translated into a simple rescaling of a few observable quantities, and can therefore be applied to any system where a spike is expected to be present.

Chapter 2

The Phase Space Formalism And Adiabatic Invariance

This chapter studies the phase space distribution of a system of collisionless particles in a Kerr metric background. The idea is to generalize the distribution $f(\boldsymbol{x}, \boldsymbol{p})$ from statistical mechanics to a four-dimensional $f(x, p)$. This object will then allow us to obtain a phase space distribution $f^{(3)}(\boldsymbol{x}_u, \boldsymbol{p}_u)$ measured by any observer moving with four-velocity u. The interpretation of the phase space distribution as the probability of a particle being in the element of phase space $\mathrm{d}^3 x_u \, \mathrm{d}^3 p_u$ tells us that knowledge of $f^{(3)}$ is all we need to calculate any physical observable like the energy-momentum tensor of the system. Our main results in this chapter are Eqs. (2.13, 2.20), in which we give, respectively, the mass current density four vector and the local interaction rate per four-volume — given an interaction cross section σ — in terms of the conserved quantities of Kerr geodesics. Our work here is a direct extension of the calculations performed in [52] (SFW heareafter).

2.1 Phase Space Analysis for a Newtonian System

As a prelude to the relativistic calculation, we will review the calculation of a density from a phase space distribution $f(\boldsymbol{x}, \boldsymbol{p})$ in newtonian mechanics. Due to the relationship $\boldsymbol{p} = m\boldsymbol{v}$ between the canonical momentum and the velocity in Cartesian coordinates, it is customary to refer to a distribution in velocity space $f(\boldsymbol{x}, \boldsymbol{v})$, which we will do. Although this object has a probability interpretation, instead of normalizing it to 1, we will normalize it to the total mass of the system. Therefore, the mass density is given by

$$\rho(\boldsymbol{x}) = \int \mathrm{d}^3\boldsymbol{v}\, f(\boldsymbol{x}, \boldsymbol{v}). \tag{2.1}$$

Even though the components of the velocity are not coordinates in phase space, this object is also referred to as a phase-space density or a phase-space distribution function. We will be interested in time-independent density profiles, which constrain the function $f(\boldsymbol{x}, \boldsymbol{v})$ to be a function of the constants of the motion for orbits in the gravitational potential it generates, a result known as the Jeans theorem [31]. These conserved quantities are, for a spherically symmetric system

$$\boldsymbol{L} = \boldsymbol{x} \times \boldsymbol{v}, \tag{2.2a}$$

$$E = \frac{1}{2}v^2 + \Phi(r), \tag{2.2b}$$

where $r = |\boldsymbol{x}|$. From this point forward, we will only consider non-relativistic systems that are spherically symmetric. This implies that the distribution function can only depend on E and L, which are invariant under rotations. Changing our phase space coordinates from (v^r, v^θ, v^ϕ) to (E, L, L_z) allow us to simplify Eq. (2.1). The components of the velocity in spherical coordinates are related to the conserved quantities by

$$v^r = \pm\sqrt{2(E - \Phi(r)) - \frac{L^2}{r^2}}, \tag{2.3a}$$

$$v^\theta = \pm\frac{1}{r}\sqrt{L^2 - \frac{L_z^2}{\sin^2\theta}}, \tag{2.3b}$$

$$v^\phi = \frac{L_z}{r\sin\theta}. \tag{2.3c}$$

In the above equation, $v^\theta = \boldsymbol{v} \cdot \hat{\theta}, v^\phi = \boldsymbol{v} \cdot \hat{\phi}$, instead of $\dot{\theta}, \dot{\phi}$ as is usual in relativity. We do this so that the volume element $\mathrm{d}^3\boldsymbol{v} = \mathrm{d}v^r\,\mathrm{d}v^\theta\,\mathrm{d}v^\phi$. The Jacobian matrix $\frac{\partial(v^r, v^\theta, v^\phi)}{\partial(E, L, L_z)}$ is triangular, so its determinant j can be straightforwardly calculated, and we obtain

$$j = \frac{L}{r^2 \sin\theta \sqrt{2(E - \Phi(r)) - L^2/r^2}\sqrt{L^2 - L_z^2/\sin^2\theta}}. \tag{2.4}$$

Because of the ± in Eqs. (2.3a, 2.3b), each triad (E, L, L_z) corresponds to 4 velocity vectors. Therefore, to properly integrate over velocity space, we must use $4j$ instead of j once we have performed the change of variables in Eq. (2.3). The integration limits are obtained by requiring that the velocity components are real, and we will also assume that only bound $(E < 0)$ orbits contribute to the density. The L_z integral may be immediately performed, giving a factor of π, and we obtain

$$\rho(r) = \frac{4\pi}{r^2} \int\limits_{\Phi(r)}^{0} \mathrm{d}E \int\limits_{0}^{r\sqrt{2(E-\Phi(r))}} \mathrm{d}L\, \frac{L f(E, L)}{\sqrt{2(E - \Phi(r)) - L^2/r^2}}. \tag{2.5}$$

If the velocity distribution is also isotropic, then f can only depend on v, and it will therefore have no L dependence. The L integral may then be performed, giving

$$\rho(r) = 4\pi \int_{\Phi(r)}^{0} \mathrm{d}E\, f(E) \sqrt{2(E - \Phi(r))}. \tag{2.6}$$

In this very special case, Eddington's method [31] allows us to obtain $f(E)$ directly from the density profile $\rho(r)$ in a way that is consistent with Poisson's equation $\nabla^2\Phi(r) = 4\pi G\rho(r)$.

2.2 Phase Space Distributions in a Relativistic Background

The phase-space formalism can be applied in GR with only slight modifications to the Newtonian calculation: a phase space distribution $f^{(4)}(x,p)$ can be defined without any issues, but the scalar character of the distribution [53] means that some care must be taken in trying to extract a frame-dependent quantity such as a density from it. The proper way to do this is by defining a mass-current density 4-vector

$$J_\mu(x) = \int \mathrm{d}^4p \,\sqrt{-g} f^{(4)}(x,p) u_\mu, \tag{2.7}$$

where the $\sqrt{-g}$ factor means that we are integrating over contravariant momentum components [54] and $u_\mu = p_\mu/m_\chi$, m_χ being the mass of the DM particle. Throughout this work, we will consider a single species of dark matter, which implies that our phase-space distribution will only be non-zero for momenta satisfying the mass-shell condition $\tilde{\mu} \equiv \sqrt{-g_{\mu\nu}p^\mu p^\nu} = m_\chi$. In order to connect with the non-relativistic formalism, we will define

$$f^{(4)}(x,p) = \tilde{\mu}^{-3} f(x,\boldsymbol{p})\delta(\tilde{\mu} - m_\chi), \tag{2.8}$$

where $\boldsymbol{p}$ refers to the spatial components of the momentum in a given coordinate system. This makes it so that the phase space distribution we are defining here has the same units as the non-relativistic $f(\boldsymbol{x},\boldsymbol{v})$, so the relativistic phase space distribution is also normalized to a mass (see Sec. (2.4) for a more precise definition). We now specialize these definitions to the Kerr metric in Boyer-Lindquist coordinates, which is given by

$$\begin{aligned}\mathrm{d}s^2 = &-\left(1 - \frac{2Gmr}{\Sigma^2}\right)\mathrm{d}t^2 + \frac{\Sigma^2}{\Delta}\,\mathrm{d}r^2 + \Sigma^2\,\mathrm{d}\theta^2 - \frac{4Gmar}{\Sigma^2}\sin^2\theta\,\mathrm{d}\phi\,\mathrm{d}t \\ &+ \left(r^2 + a^2 + \frac{2Gmra^2\sin^2\theta}{\Sigma^2}\right)\sin^2\theta\,\mathrm{d}\phi^2\,. \end{aligned} \tag{2.9}$$

Here, m is the mass of the black hole, $a = J/m$, where J is the hole's angular momentum, and we have introduced the functions $\Delta = r^2 + a^2 - 2Gmr$ and $\Sigma^2 = r^2 + a^2\cos^2\theta$. We will also define $\alpha = a/Gm$, a dimensionless Kerr parameter that satisfies $0 \le \alpha \le 1$. The DM distribution is also a source of gravitational potential, and we should look for self-consistent solutions of Einstein's equations including both the BH and the DM. However, within the radius of influence of the BH, the contribution of the DM to the gravitational field is negligible and, as such, we are allowed to use the Kerr metric as a fixed background for our phase space integrations.

Just as in the non-relativistic formalism, if our phase space distribution is to describe an equilibrium system, it may only depend on constants of the motion. Thus, we will perform a similar change of variables as was performed in Eq. (2.3) to write the components of the four-velocity in Boyer-Lindquist coordinates in terms of the conserved quantities. For geodesics of the Kerr spacetime this is possible as there are four constants of the motion: the specific energy $\mathcal{E}$, the specific angular momentum L_z, the rest mass $\tilde{\mu}$ and the Carter constant C, which is related to the total angular momentum in the limit $a \to 0$ [55, 52]. The change of variables reads

$$\mathcal{E} \equiv -u_t = -g_{tt}u^t - g_{t\phi}u^\phi, \tag{2.10a}$$

$$L_z \equiv u_\phi = g_{\phi\phi}u^\phi + g_{t\phi}u^t, \tag{2.10b}$$

$$\tilde{\mu} \equiv \sqrt{-g_{\mu\nu}p^\mu p^\nu}, \tag{2.10c}$$

$$C \equiv \Sigma^4(u^\theta)^2 + \frac{L_z^2}{\sin^2\theta} + a^2\cos^2\theta(1-\mathcal{E}^2). \tag{2.10d}$$

Using these definitions, we can convert the momentum space volume d^4p to the integration volume $\mathrm{d}\mathcal{E}\,\mathrm{d}L_z\,\mathrm{d}C\,\mathrm{d}\tilde{\mu}$ by calculating the inverse jacobian $\mathcal{J}^{-1}$

$$\begin{aligned}\mathcal{J}^{-1} = \left|\frac{\partial(\mathcal{E}, L_z, C, \tilde{\mu})}{\partial(p^t, p^r, p^\theta, p^\phi)}\right| &= \tilde{\mu}^{-3}\begin{vmatrix} -g_{00} & 0 & 0 & -g_{t\phi} \\ \frac{\partial C}{\partial u^0} & 0 & 2\Sigma^4 u^\theta & \frac{\partial C}{\partial u^\phi} \\ g_{t\phi} & 0 & 0 & g_{\phi\phi} \\ \mathcal{E} & -u_r & -u_\theta & L_z \end{vmatrix}. \\ &= -\frac{2\Sigma^4 \Delta u_r u^\theta \sin^2\theta}{\tilde{\mu}^3} \end{aligned} \tag{2.11}$$

In order to use this expression, we need to manipulate Eqs. (2.10) to find u_r, u^θ, which are given by

$$u_r = \pm\frac{r^2}{\Delta}V(r)^{1/2}, \tag{2.12a}$$

$$u^\theta = \pm\Sigma^{-2}\sqrt{U(\theta)}, \tag{2.12b}$$

$$V(r) = \left(1 + \frac{a^2}{r^2} + \frac{2Gma^2}{r^2}\right)\mathcal{E}^2 - \frac{\Delta}{r^2}\left(1 + \frac{C}{r^2}\right) + \frac{a^2L_z^2}{r^4} - \frac{4Gma\mathcal{E}L_z}{r^3}, \tag{2.12c}$$

$$U(\theta) = C - \frac{L_z^2}{\sin^2\theta} - a^2\cos^2(1 - \mathcal{E}^2). \tag{2.12d}$$

An important observation is that $-V(r)$ is analogous to the effective potential from classical mechanics, but with 0 total energy. This identification allows us to qualitatively understand the radial motion of a Kerr geodesic by looking at a plot of $V(r)$.

As in the newtonian case, the ± above implies that each set $(\mathcal{E}, C, L_z)$ is related to four different 4-momenta. Thus, when we change variables from p^μ to $(\mathcal{E}, C, L_z, \tilde{\mu})$, we must add a factor of 4 to our result. To obtain a final expression for the currents, we use the fact that $\sqrt{-g} = \Sigma^2\sin\theta$, and then plug in Eq. (2.8) into Eq. (2.7), using the jacobian and the four-velocities given in Eqs. (2.11) and (2.12).

The J_r, J_θ components will be identically zero due to the fact that the positive u_r, u_θ contributions in the integral have the exact same weights as the negative contributions. For a Schwarzschild black hole, $V(r)$ is independent of L_z, and J_ϕ is also zero by parity. For the Kerr metric, this is no longer the case, and the J_ϕ component will be non-zero. We can interpret this as the "frame-dragging" induced by the spinning black hole. The non-zero components $J_{(t,\phi)}$ are given by

$$J_{(t,\phi)} = \frac{2}{r^2 \sin\theta} \int \mathrm{d}\mathcal{E}\, \mathrm{d}C\, \mathrm{d}L_z\, \frac{u_{(t,\phi)} f(\mathcal{E}, C, L_z)}{\sqrt{V(r)U(\theta)}}. \tag{2.13}$$

Our calculations in this chapter and the following chapters will all be performed in Boyer-Lindquist coordinates. Since this is not a familiar coordinate system, some expressions that we will derive in this section, like Eq. (2.20), seem rather involved. To make the derivation of these expressions more palatable, we will use two ideas. The first is that we can locally define any observer by a time-like vector n_μ that is normalized: $n^2 = -1$. This is just the observer's four-velocity at a given point. The second is that some of the frame dependent quantities may be expressed as scalars *if we make the frame dependence explicit.*

As an example, given the mass current four-vector J_μ, the "observer n_μ" measures a DM density $\rho(n) = -J^\mu n_\mu$. Thus, if we have J_μ and n_μ in Boyer-Lindquist coordinates, we know the density observed by n_μ. There is a special observer t_μ that moves with the average velocity of the DM distribution. The frame moving with velocity t_μ is the *rest frame* of the DM. We will refer to the density in that frame as ρ, without any four-vector attached to it. By definition, $J_\mu = \rho t_\mu$, from which we obtain $\rho = \sqrt{-J^2}$. In Boyer-Lindquist coordinates, introducing $\Omega \equiv J_\phi / J_t$, the rest frame density is given by

$$\rho = |J_t| \sqrt{\frac{g_{\phi\phi} - 2 g_{t\phi}\Omega + g_{tt}\Omega^2}{\Delta \sin^2\theta}}. \tag{2.14}$$

To calculate more complicated observables, we need to go back to the idea that $f(x,p)\,\mathrm{d}^4p$ represents the probability that a particle is in an element d^4p of momentum space and understand how a given observer would define her own probability distribution having knowledge of $f(x,p)$. To simplify the notation, we will refer to the integrand of each current component in Eq. (2.13) as $\mathrm{d}J_\mu$. We can use this differential current element to define the fraction of particles in a given phase-space element $(\mathcal{E}, C, L_z)$, which is a frame-dependent probability distribution. Since $-n^\mu \, \mathrm{d}J_\mu$ is the "differential density element" observed in the frame n, we may define this probability distribution as

$$\mathcal{P}_n(\mathcal{E}, L_z, C) = \frac{n^\mu \, \mathrm{d}J_\mu}{J_\alpha n^\alpha}. \tag{2.15}$$

Although the probability distribution defined above is explicitly frame dependent, we emphasize that it is *not* dependent on any coordinate system. This is because the differential phase space distribution $f(\mathcal{E}, L_z, C)\mathcal{J}^{-1} \, \mathrm{d}\mathcal{E} \, \mathrm{d}L_z \, \mathrm{d}C$ is a scalar [53]. Physically, this is just a restatement of the fact that the constants of the motion are uniquely determined by a given geodesic. Therefore, the above probability distribution provides the "density of particles following a given trajectory", which is an explicitly coordinate independent (but frame dependent) quantity. With this definition, it is now straightforward to calculate averages over phase space. For instance, if we consider quantities $x_{1\mathrm{ptc}}(\mathcal{E}, L_z, C), x_{2\mathrm{ptc}}(\mathcal{E}, L_z, C, \mathcal{E}', L_z', C')$ that depend, respectively, on the phase space coordinates of one and two particles, their averages will be given by

$$\langle x_{1\mathrm{ptc}} \rangle = \int \mathrm{d}\mathcal{E} \, \mathrm{d}L_z \, \mathrm{d}C \, \mathcal{P}_n(\mathcal{E}, L_z, C) x_{1\mathrm{ptc}}(\mathcal{E}, L_z, C), \tag{2.16a}$$

$$\langle x_{2\mathrm{ptc}} \rangle = \int \mathrm{d}\mathcal{E} \, \mathrm{d}L_z \, \mathrm{d}C \, \mathrm{d}\mathcal{E}' \, \mathrm{d}L_z' \, \mathrm{d}C' \, \mathcal{P}_n(\mathcal{E}, L_z, C)\mathcal{P}_n(\mathcal{E}', L_z', C') x_{2\mathrm{ptc}}(\mathcal{E}, L_z, C, \mathcal{E}', L_z', C'). \tag{2.16b}$$

As examples of what the quantities $x_{1\mathrm{ptc}}, x_{2\mathrm{ptc}}$ may be, $x_{1\mathrm{ptc}}$ could be the kinetic energy of a particle, and $x_{2\mathrm{ptc}}$ could be a two-body collision cross-section, which depends on the center of mass energy of the system, and therefore on a combination of the phase space coordinates of each colliding particle. In fact, an important application of the second of Eqs. (2.16) is the calculation of a two-body collision rate per unit four-volume of spacetime, which we will now derive, as it will be important in later sections.

In order to make this calculation more transparent, we will go one step further than simply considering what an observer n_μ would measure: we will also define locally flat coordinates $x = (t, \boldsymbol{x})$ that have as a time coordinate the proper time measured by the observer n_μ. This will allows to generalize an expression derived in flat spacetime by Weaver [56]. At a given point, the collision rate of a pair of identical particles χ is [57]

$$\tilde{\Gamma} = \sigma u_\chi n_\chi, \tag{2.17}$$

with σ the total interaction cross section, n_χ the particle number density, and

$$u_\chi = \frac{\sqrt{(u_1 \cdot u_2)^2 - 1}}{\gamma_1 \gamma_2}, \tag{2.18a}$$

$$\gamma_i = -u_i \cdot n. \tag{2.18b}$$

The factor u_χ in the above equation is known as the Möller velocity, and it is the relativistic equivalent of the newtonian relative velocity $|\boldsymbol{v}_1 - \boldsymbol{v}_2|$, and does not correspond to a physical velocity [58]. The relative velocity v_{rel} that one of the colliding particles sees the other one moving with is such that $\sqrt{(u_1 \cdot u_2)^2 - 1} = \gamma_{\mathrm{rel}} v_{\mathrm{rel}}$. There are $n_\chi \, \mathrm{d}^3x \,/2$ pairs of particles in a 3-volume around the spacetime point, which gives a collision rate per 4-volume

$$\frac{\mathrm{d}N}{\mathrm{d}^4x} = \frac{n_\chi^2 \sigma \gamma_{\mathrm{rel}} v_{\mathrm{rel}}}{2\gamma_1\gamma_2}. \tag{2.19}$$

The above equation assumes that each particle in the pair has fixed four-velocities u_1, u_2. In order to obtain the total event rate per four-volume, what we must do is average Eq. (2.19) over the four-velocities of each particle in the pair. We do this by using Eq. (2.16) with Eq. (2.19) as the observable x_{2ptc}. We now use the expression for $\mathcal{P}_n(\mathcal{E}, C, L_z)$, Eq. (2.15), and the expressions for $\mathrm{d}J_\mu$. Since the currents are normalized to a mass density, we also insert $n_\chi = \rho/m_\chi$, where m_χ is the mass of the dark matter particle.

$$\frac{1}{\sqrt{-g}}\frac{\mathrm{d}N}{\mathrm{d}^4x} = \frac{1}{2m_\chi^2}\left(\frac{2}{r^2\sin\theta}\right)^2 \int \frac{\mathrm{d}\mathcal{E}\,\mathrm{d}L_z\,\mathrm{d}C}{V(r)U(\theta)}\frac{\mathrm{d}\mathcal{E}'\,\mathrm{d}L_z'\,\mathrm{d}C'}{V(r)'U(\theta)'} f(\mathcal{E},L_z,C)f(\mathcal{E}',L_z',C')\sigma(\gamma_{\mathrm{rel}})\gamma_{\mathrm{rel}}v_{\mathrm{rel}}, \tag{2.20}$$

where we have now inserted a factor of $(-g)^{-1/2}$ —which is simply 1 in our flat coordinate system —to allow x to refer to any desired set of coordinates. Since this is an event-rate per spacetime volume, the above expression should be a Lorentz scalar, which it is since the combination $f\mathrm{d}^3\boldsymbol{p}$ is a scalar, as pointed out previously. We display Eq. (2.20) in the above form precisely so that the combination $f\mathrm{d}^3\boldsymbol{p}$ is easily recognizable and the formalism can be simply transferred to other background metrics. It is important to stress, however, that our definition of the currents, Eq. (2.7), contains a factor of $\sqrt{-g}$. This means that, in an FRW background, for example, $\boldsymbol{p}$ would be the comoving momentum, not the physical momentum. In general, $\boldsymbol{p}$ would be the contravariant components of the *canonical momentum* p_μ.

2.2.1 Identifying the Integration Region

The expressions for the four-velocities in Eqs (2.12) show that, once a point (t, r, θ, ϕ) is fixed, the constants of the motion $(\mathcal{E}, L_z, C)$ are not allowed to vary arbitrarily, just as in the newtonian case. The components of the four-velocities must be real numbers, and we must therefore require that $V(r) \geq 0$ and $U(\theta) \geq 0$.

The first constraint provides an upper bound to the Carter constant $C \leq C_{\mathrm{max}}(\mathcal{E}, L_z)$, which can be interpreted physically as an angular momentum barrier: if the orbit has an angular momentum that is too high, it must be farther away from the black hole than the coordinate r. We will also only consider bound orbits, which implies $\mathcal{E} \leq 1$. This is different from the non-relativistic condition $E < 0$ since the relativistic energy includes the total mass m_χ. Thus, if the particle is bound, the energy per unit mass $\mathcal{E} \leq 1$.

The last restriction we will impose on our integration over orbits is that only particles that are not captured by the black hole are counted. Unlike the non-relativistic Kepler problem, particles with non-zero angular momentum can reach the singularity, and will therefore not be a part of the spike, as they are captured in finite time.

We illustrate this in Fig. (2.1): decreasing the Carter constant for fixed $\mathcal{E}$,L_z takes us from a bound orbit to a plunge orbit, which falls into the black hole. We denote this critical Carter constant by $C_{\text{crit}}(\mathcal{E}, L_z)$. In the Schwarzschild geometry, an explicit criterion is known for determining whether or not an orbit plunges [52], but this is not the case for the Kerr metric, due to the additional complexity of the potential.

Fig. (2.1) does, however, illustrate a simple method to exclude plunge orbits: we begin by finding the location of the unstable orbit (the concave down extremum of the potential). If that point is such that the effective potential $-V(r) < 0$, then, as we can see from the figure, the particle will plunge. We therefore require $V(r) < 0$ at the the unstable orbit.

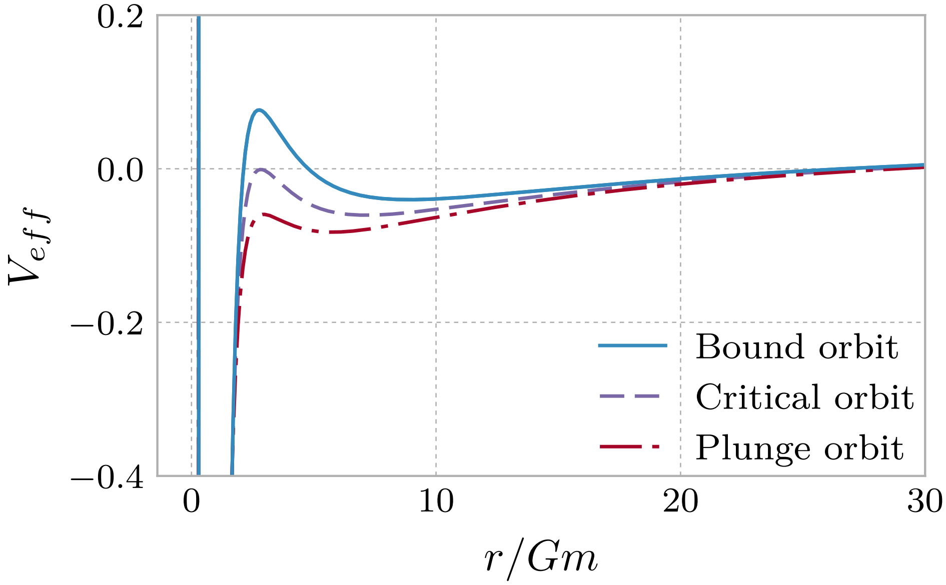

Fig. 2.1: A plot of $V_{\text{eff}}(r) = -V(r)$ vs. r/Gm with fixed $\mathcal{E}$, L_z. Varying the Carter constant separates bound and plunge orbits. The blue orbit has C=12.0$(Gm)^2$. Decreasing C we reach the red line showing the critical orbit with C=C_{crit}, which is equal to $C_{\text{crit}} = 10.3(Gm)^2$ in this case. For smaller C the orbits plunge into the hole, as depicted by the dot-dashed red line with $C = 9(Gm)^2$.

Another important point that can be uncovered from the above figure is that the orbits are not connected, in the sense that, given ($\mathcal{E}$, L_z, C), two bound orbits are actually present, due to a potential barrier at very small distances. This potential barrier is not physical: orbits that are “bound” by it would always have to cross the event horizon of the black hole [59], and should therefore be excluded as plunge orbits. To exclude these orbits, we calculate the location $r_{\text{unst}}(\mathcal{E}, L_z, C)$ of the unstable orbit for each phase space point and require that the point r *at which we are evaluating the currents* is such that $r > r_{\text{unst}}$. See Fig. (2.2) for a graphical identification of these features.

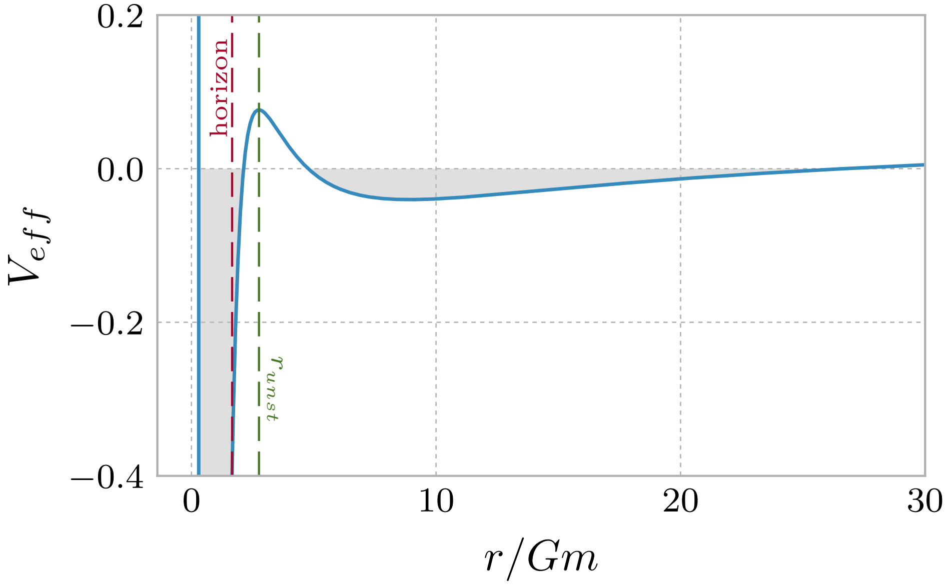

Fig. 2.2: A plot of $V_{eff} = -V(r)$. The shaded regions correspond to where the particle is allowed to move. The unstable particle orbit at r_{unst} is shown, along with the event horizon. This figure illustrates that, generically, the correct bound orbit must have $r > r_{\text{unst}}$.

Fig. (2.3) shows a typical slice of the phase space region at fixed energy, comparing it to the corresponding Schwarzschild case. The upper curve in that figure corresponds to $V(r)=0$, and the two parabolic branches to the left and right correspond to $U(\theta)= 0$. The bottom curve, corresponding to the boundary of captured orbits, is in fact a double constraint: since our criterion for a particle not to plunge is that, at the extremum point r_{unst}, for which $V(r_{\text{unst}}, \mathcal{E}, C, L_z)' = 0$, $V(r_{\text{unst}}) > 0$, the separation between stable and plunge orbits occurs whenever $V(r_{\text{unst}}, \mathcal{E}, C, L_z)' = V(r_{\text{unst}}) = 0$. Note that this orbit *does not* have to be located at the coordinate r where we are evaluating the currents. Anticipating the results that shall be explicitly obtained further on, we note that there are two main effects to the addition of spin to the calculation: preferential capture of counter-rotating orbits [60] and enhanced binding of co-rotating orbits. We will show that the latter effect is dominant, which will lead to an enhancement of the density.

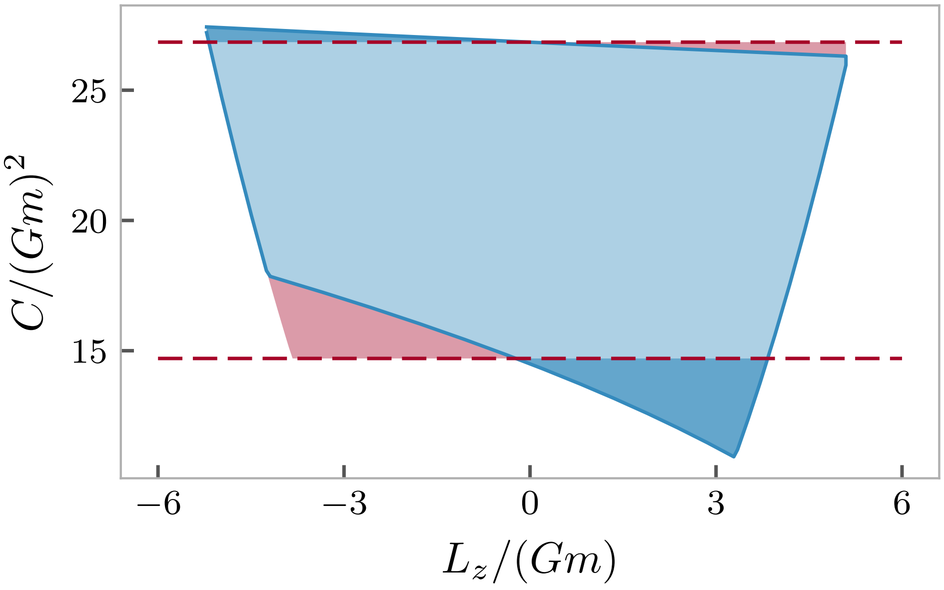

Fig. 2.3: The blue region shows a phase space slice of fixed energy, $\mathcal{E} = 0.98$, at $r/Gm = 20$ on the equatorial plane for a Kerr hole with $\alpha = 0.5$. The upper dashed line corresponds to $V(r) = 0$ for $r = 20Gm$, and the lower dashed line corresponds to the capture condition for $\mathcal{E} = 0.98$, both in the Schwarzschild case. The red-shaded lower-left region shows the counter-rotating orbits that are lost due to capture by the hole, which are compensated by the tightly bound co-rotating orbits in the dark blue-shaded region.

When all four constraints are saturated simultaneously, we have an energy slice that would consist of a single point: this is the minimum allowed energy $\mathcal{E}_{\text{min}}(r, \theta)$. The four constraints described above give us a set of polynomial equations that can be solved for a set $(\mathcal{E}_{\text{min}}, C_{\text{min}}, L_z^*, r_{\text{unst}}^*)$. We use the values of $\mathcal{E}_{\text{min}}$ and C_{min} to bound our phase space region.

Since the boundaries of the integration region cannot be determined analytically, no simplifying change of variable can be made to speed up the calculations, and we therefore use monte carlo (MC) integration to overcome this difficulty. Most MC integrators require that the region be mapped into a cube, and in order to do that we use the following change of variables

$$\begin{aligned}
\mathcal{E} &= x + (1-x)\mathcal{E}_{\min}, \\
C &= yC_{\max} + (1-y)C_{\min}, \\
L_z &= (2z-1)\sin\theta\sqrt{C - a^2\cos^2\theta(1-\mathcal{E}^2)},
\end{aligned} \tag{2.21}$$

which maps the integration region to $[0,1]\times[0,1]\times[0,1]$. $C_{\max}$ is found by noting that, from the positivity of $U(\theta)$ one obtains $C \geq \sin^2\theta L_z^2$ for bound orbits. Thus, substituting $L_z = -\sin\theta\sqrt{C}$ and $\mathcal{E}=1$ in the constraint $V(r)\geq 0$, we find

$$-\left(\frac{\Delta - a^2\sin^2\theta}{r^4}\right)C + \frac{4a\sin\theta}{r^3}\sqrt{C} + \left(1 + \frac{a^2}{r^2} + \frac{2Gma^2}{r^3} - \frac{\Delta}{r^2}\right) \geq 0. \tag{2.22}$$

Reversing the sign of the inequality, we find

$$\begin{aligned}
&\gamma C - \delta\sqrt{C} + \beta \leq 0, \\
&\gamma = \frac{r^2 - 2Gmr + a^2\cos^2\theta}{r^4},\ \delta = \frac{4Gma\sin\theta}{r^3},\ \beta = \frac{2Gm}{r}\left(1 + \frac{a^2}{r^2}\right).
\end{aligned} \tag{2.23}$$

The coefficient $\gamma > 0$ outside of the ergoregion, the region in which particles are forced to spin in the direction of the SMBH's spin [15]. We will treat points inside that region separately. Outside of that region, the above inequality is satisfied for $\sqrt{C_-} \leq \sqrt{C} \leq \sqrt{C_+}$, with

$$\sqrt{C_+(r,\theta)} = \frac{\delta + \sqrt{\delta^2 + 4\beta\gamma}}{2\gamma}(Gm). \tag{2.24}$$

This allows us to find an upper bound for C everywhere outside the ergoregion. Inside of the ergoregion, what bounds C is the capture condition: we may always find a plunge orbit with $\mathcal{E} = 1$ and $V(r) = 0$ there, and this provides an upper bound on C.

In the Schwarzschild geometry, there is a special circular orbit at $r = 4Gm$ which has $\mathcal{E} = 1$. This is known as the marginally bound orbit, and any particle orbit that gets closer to the black hole than this is either unbound or a plunge orbit. The location of the equivalent orbit in the Kerr geometry is known for equatorial orbits [61], and we can find the marginally bound orbit for an arbitrary inclination by setting $\mathcal{E}_{\text{min}}(r_{\text{min}}(\theta), \theta) = 1$. As in the spherical case, any orbit with $r < r_{\text{min}}(\theta)$ is either unbound or a plunge orbit, which means that the dark matter density is zero inside the surface $r < r_{\text{min}}(\theta)$. See Fig. (2.4) for a plot of $r_{\text{min}}(\theta)$ With this information in hand, we know where the density is non-zero, as well as the appropriate set of orbits to integrate over, and we may now begin to explore various choices for the phase space distribution $f(\mathcal{E}, C, L_z)$.

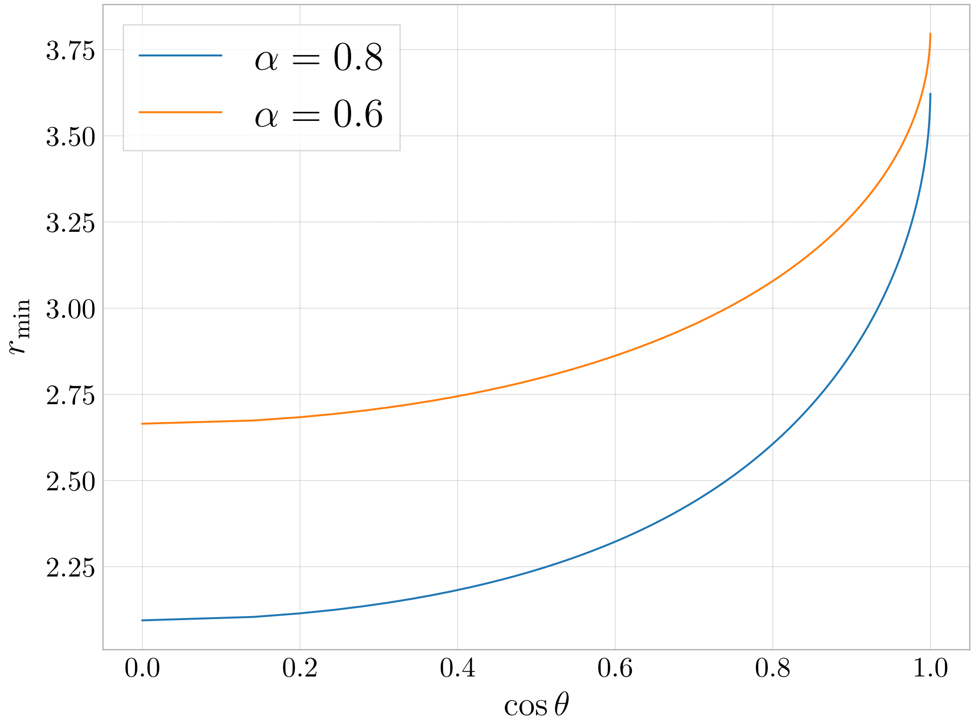

Fig. 2.4: The radial coordinate of the surface of marginally bound orbits $r_{\text{min}}(\theta)$ for two values of the dimensionless spin parameter.

2.2.2 Axial Orbits

Similarly to Newtonian mechanics, any orbit with $L_z \neq 0$ cannot cross the axis $\theta = 0$. This means that the phase space for these orbits should be effectively two-dimensional, which simplifies calculations greatly. Moreover, since $u_\phi = L_z$, $J_\phi = 0$ along the axis, and the calculation of the current density is further simplified.

Using the change of variables from Eq. (2.21), we have

$$J_\mu = \frac{2(1-\mathcal{E}_{\min})(C_{\max}-C_{\min})}{r^2} \int\limits_0^1 \mathrm{d}x\,\mathrm{d}y\,\mathrm{d}z\,\frac{u_\mu f(\mathcal{E},C,L_z)}{\sqrt{V(r)}\sqrt{z(1-z)}}. \tag{2.25}$$

In the limit $\sin\theta \to 0$, our change of variables forces $L_z \to 0$ everywhere, and once that is done the z dependence in the integral comes strictly from the factor $(z(1-z))^{-1/2}$. This can be integrated explicitly to give a factor of π. For clarity, we can now "undo" the change of variables in Eq. (2.21) to find

$$J_t = -\frac{2\pi}{r^2} \int\limits_{\mathcal{E}_{\min}}^{1} \mathrm{d}\mathcal{E} \int\limits_{C_{\mathrm{crit}}(\mathcal{E})}^{C_{\max}} \mathrm{d}C\,\frac{\mathcal{E} f(\mathcal{E},C)}{\sqrt{V(r)}}. \tag{2.26}$$

Referring to Eq. (2.12), we see that the potential can be written as $p(r)/r^4$, where p is a polynomial in r. With L_z fixed to 0, there is an alternative method of finding C_{crit} which allows us to simplify the integration region: a plunge orbit has $V(r) = rV(r)' = 0$, which implies $p = rp' = 0$. This condition implies that the polynomial $p(r)$ has a double root, further implying that its discriminant vanishes. Setting the discriminant to zero gives a fifth order polynomial equation in C, which can be solved numerically. In general, this equation will have 3 positive roots, corresponding to the three extrema of the potential that can be set to 0 potential. The second largest root is the one that sets the unstable orbit to have $V(r) = 0$, and thus this gives us a method to find $C_{\mathrm{crit}}(\mathcal{E})$. This allows a further change of variable

$$\mathcal{E} = x + (1-x)\mathcal{E}_{\min}(r), \tag{2.27a}$$

$$C = yC_{\max}(\mathcal{E}) + (1-y)C_{\text{crit}}(\mathcal{E}). \tag{2.27b}$$

This change of variables fully constrains the integration region to $[0,1] \times [0,1]$, which allows us to use efficient grid-based methods rules to perform the integration numerically. Noting that we can write $V(r) = (\Delta/r^4)(C_{\max} - C)$, we obtain a simple expression for J_t

$$J_t = -\frac{2\pi}{\sqrt{\Delta}}(1-\mathcal{E}_{\min}) \int\limits_0^1 \mathrm{d}x\, \mathrm{d}y\, \mathcal{E} f(\mathcal{E}, C) \frac{\sqrt{C_{\max} - C_{\text{crit}}}}{\sqrt{1-y}}. \tag{2.28}$$

The minimum energy can also be found by a simpler method, since we have a better way of finding C_{crit}. We can just solve the equation $C_{\max} = C_{\text{crit}}$ by the bisection method, as this is now a one-dimensional equation. To find $r_{\min}$, we can use the fact that, for $r < r_{\text{ISCO}}$, where r_{ISCO} is the innermost stable circular orbit for the axis (which, in this case, would be a spherical orbit), the unstable orbit r_{unst} is in fact located at r. This allows us to explicitly solve for the minimum energy, obtaining

$$\mathcal{E}_{\min} = \frac{\sqrt{r}\Delta}{\sqrt{r^5 - 3r^4 + 2a^2r^3 - 2Gma^2r^2 + a^4r + Gma^4}}. \tag{2.29}$$

Setting $\mathcal{E}_{\min}$= 1 now allows us to find the minimum radius of the spike along the axis and perform the desired integrations. Due to the angular momentum barrier, we expect that the density along the axis should provide a lower bound on the density everywhere else, and this simpler expression provides us with a check that the MC is integrating correctly, both by checking its $\theta \to 0$ limit and by making sure that the density is always larger than what is obtained along the axis.

2.3 A Toy Model: Constant Distribution Function

The first application of adiabatic matching was done by Peebles [44], in which he considered an isothermal distribution $f(E) \propto \exp(-E^2/\sigma_v^2)$, where E is the kinetic energy. Only the most bound orbits should get close to a growing central mass, and therefore it is appropriate to set $E = 0$ close to the black hole, which leads to a constant distribution function. The invariance of the distribution function under adiabatic growth of the point mass implies that we can take this same constant distribution function as our $f(\mathcal{E}, C, L_z)$. In this case, the density will be proportional to the total phase space volume available at each point. This is an important quantity on its own, as it quantifies the total number of orbits crossing a given point. We will therefore focus on the calculation of the currents with a constant distribution function to gain a physical understanding of the effects of spin.

2.3.1 Restriction to Equatorial Orbits

Far from the black hole (formally, as $r \to \infty$, in the weak field region), the gravitational field of the black hole can be decomposed into an electric and a magnetic part, the magnetic part being due to the "frame-dragging" induced by the black hole's spin [62]. Therefore, to have some intuition for this problem, it is reasonable to think of the spinning black hole as a combination of a gravitational "monopole" coming from its mass and a gravitational "dipole" generated by the spin.

This means that the effective potential will have a magnetic dipole-like term, giving rise to a "spin-orbit" coupling between the angular momentum of the black hole and the angular momentum of the orbiting particle. The effects of spin get stronger as we move closer to the black hole: for instance, observers within the ergoregion are forced to rotate in the same direction as the black hole is spinning. Since equatorial orbits are the ones that can get the closest to the event horizon (see Fig. (2.4)), we expect the effects of spin to be enhanced along the equatorial plane.

For these orbits, which are planar, we have $C = L_z^2$. Therefore, if we restrict ourselves to a constant distribution of equatorial orbits by setting $f(\mathcal{E}, C, L_z) = f_{\text{eq}}\delta(u_\theta)$, this will reduce the phase space integration to two dimensions. The effective potential is also simplified to the point that most of the calculations can be done analytically. Inserting this into Eq. (2.13) and expanding the delta function, we find

$$J_\mu = \frac{4f_{\text{eq}}}{r^2}\int \mathrm{d}\mathcal{E}\,\mathrm{d}C\,\mathrm{d}L_z\,\delta(C - L_z^2)V(r)^{-1/2}u_\mu. \tag{2.30}$$

We will use the delta function to eliminate the Carter constant, but we should keep in mind that there are two solutions for $C = L_z^2$, one for each sign of L_z. This will naturally separate our current into a co-rotating contribution and a counter-rotating contribution, as follows

$$J_\mu = \frac{4f_{\text{eq}}}{r^2}\int_{\mathcal{E}_{\min}}^{1}\mathrm{d}\mathcal{E}\left(\int_{L_z^-}^{L_z^{\text{crit,-}}}\mathrm{d}L_z\,\frac{u_\mu}{\sqrt{V(r)}} + \int_{L_z^{\text{crit,+}}}^{L_z^+}\mathrm{d}L_z\,\frac{u_\mu}{\sqrt{V(r)}}\right). \tag{2.31}$$

In the above equation, L_z^+, L_z^- are the solutions to $V(r) = 0$, once the substitution $C = L_z^2$ has been made, and $L_z^{\text{crit,+}}, L_z^{\text{crit,-}}$, are the critical values of the L_z that determine whether or not an orbit is captured. Considering a fixed energy slice, as in Fig. (2.3), this procedure would consist of integrating along the left and right boundaries of the integration region for each slice. Since we are simply considering a toy-model, it will be more convenient to work with dimensionless quantities, setting $G = m = 1$ and, to make it clear that we are working with a different set of quantities, we will also change $r \to x$. In these coordinates, the event horizon, located at $\Delta = 0$, has radial coordinate

$$x_{\text{horizon}} = 1 + \sqrt{1 - a^2}, \tag{2.32}$$

and the boundary of the ergosphere is:

$$x_{\text{ergosphere}} = 1 + \sqrt{1 - a^2\cos^2\theta} = 2. \tag{2.33}$$

The effective potential reads

$$\begin{aligned} V\Big|_{C=L_z^2} &= \frac{\mathcal{E}^2(x^3 + a^2(2+x)) - 4aL_z\mathcal{E} + (2-x)(L_z^2 + x^2) - a^2x}{x^3} \\ &= \frac{(x-2)}{x^3}(L_z^+ - L_z)(L_z - L_z^-). \end{aligned} \tag{2.34}$$

The two roots are given explicitly by

$$L_z^\pm = \frac{-2a\mathcal{E} \pm \sqrt{x\Delta((1-\mathcal{E}^2)x - 2)}}{x-2}. \tag{2.35}$$

The quantity in the square root will be positive so long as $\mathcal{E}^2 > 1 - 2/x$. Plugging this energy into the potential, we find that it gives $V < 0$, and so we can safely assume that $\mathcal{E}_{\rm min}^2 > 1 - 2/x$. In general, we will have a positive and a negative root for $x > 2$, and two positive roots for $x < 2$. At $x = 2$, the negative root goes to infinity, but the positive root tends to a finite limit.

This will not be a problem since, as we will show, there are no counter-rotating orbits at $x \leq 2$. For $x < 2$, we have $L_z^- > L_z^+$, so, referring to Eq. (2.34), we see the potential is positive for $L_z < L_z^+$ or $L_z > L_z^-$. The orbits with $L_z > L_z^-$ have $V(y) > 0$ for $y < x$, and are therefore plunge orbits. Inside the ergosphere, therefore, we will only have orbits with $L_z^{\rm crit,+} < L_z < L_z^+$. This is ultimately a consequence of the fact that the marginally bound counter-rotating orbit occurs at $x_{\rm mb}^- > 2$, which we will now show.

2.3.1.1 Finding the Critical Angular momentum and Energy

In order to find the critical angular momenta $L_z^{\rm crit,\pm}(\mathcal{E})$ and the minimum energy $\mathcal{E}_{\rm min}(x)$, we must examine the capture criterion for an orbit, which, at fixed $\mathcal{E}$, reads

$$V(x') = 0 = \frac{\mathrm{d}V}{\mathrm{d}x'}, \tag{2.36}$$

where x' is the location of the unstable orbit in the potential, which, for the critical orbit, is also a turning point of the motion. It should be clear from the physics, and also from Fig. (2.1), that x' is *not* the point x at which we are evaluating the currents. The equation for the derivative is a second order polynomial in x, which can be solved to give

$$\frac{\mathrm{d}V}{\mathrm{d}x} = 0 \Rightarrow x_{\mp} = \Big(a^2\big(1-\mathcal{E}^2\big) + L_z^2 \mp \sqrt{(L_z^2 + a^2(1-\mathcal{E}^2))^2 - 12(L_z - a\mathcal{E})^2}\Big)/2. \tag{2.37}$$

Analyzing the sign of the second derivative, or taking the $a \to 0$ limit, shows that it is the smaller root x_- that corresponds to the unstable orbit once we impose the constraint $V = 0$. Inserting this value of x_- into $V = 0$ and squaring the obtained equation gives us a polynomial in L_z.

$$\begin{aligned}
&V\Big(x,\mathcal{E}, L_z^{\mathrm{crit}}\Big) = 0 \Rightarrow \\
&\qquad 0 = -9(L_z^{\mathrm{crit}} - a\mathcal{E})^2 \times \\
&\qquad \Big[\Big(\mathcal{E}^2 - 1\Big)L_z^{\mathrm{crit}6} + \Big(36\mathcal{E}^2 - 27\mathcal{E}^4 - 3a^2\Big(1-\mathcal{E}^2\Big)^2 - 8\Big)L_z^{\mathrm{crit}4} \\
&\qquad + 36a\mathcal{E}\Big(2 - 5\mathcal{E}^2 + 3\mathcal{E}^4\Big)L_z^{\mathrm{crit}3} + 4a\mathcal{E}\Big(8 + 9a^2\Big(1-\mathcal{E}^2\Big)^2\Big(-1+3\mathcal{E}^2\Big)\Big)L_z^{\mathrm{crit}} \\
&\qquad + \Big(2a^2\Big(10 - 91\mathcal{E}^2 + 162\mathcal{E}^4 - 81\mathcal{E}^6\Big) + 3a^4\Big(\mathcal{E}^2-1\Big)^3 - 16\Big)L_z^{\mathrm{crit}2} \\
&\qquad -16a^2\mathcal{E}^2 - a^6\Big(1-\mathcal{E}^2\Big)^4 - a^4\Big(1-\mathcal{E}^2\Big)^2\Big(-1 - 18\mathcal{E}^2 + 27\mathcal{E}^4\Big)\Big],
\end{aligned} \tag{2.38}$$

which contains an unphyiscal solution $L_z = a\mathcal{E}$, and a sixth order polynomial in L_z. This polynomial can be solved numerically, and, since we know that $L_z^- \leq L_z \leq L_z^{\text{crit,-}}$ and $L_z^{\text{crit,+}} \leq L_z \leq L_z^+$, we can find both critical angular momenta by taking the largest positive root smaller than L_z^+ and the largest (in magnitude) negative root that is larger than L_z^-. As in our discussion of axial orbits in Sec. (2.2), these are, in general, the second largest roots in magnitude.

Knowing this, we can solve for $\mathcal{E}_{\min}(x)$ using a bisection method for the equation $L_z^{\text{crit,+}} = L_z^+$. The marginally bound orbits can be found by solving Eq. (2.38) with $\mathcal{E} = 1$, and then going back to the solution x_-. This is because the marginally bound orbit is itself unstable, meaning that the location of the unstable orbit will coincide with the point where we are evaluating the currents. When we set $\mathcal{E} = 1$, we obtain

$$0 = -9(a - L_z)^2\Big(-16a^2 + 32aL_z - 16L_z^2 + L_z^4\Big), \tag{2.39}$$

which can be solved analytically, giving

$$\begin{aligned} L_z^{\text{crit}} = a, 2\Big(1 - \sqrt{1-a}\Big), 2\Big(1 + \sqrt{1-a}\Big),& \\ 2\Big(-1 - \sqrt{1+a}\Big), 2\Big(-1 + \sqrt{1+a}\Big).& \end{aligned} \tag{2.40}$$

This has only one negative solution, corresponding to a counter-rotating marginally bound orbit at

$$x_{\text{mb}}^{-} = 2 + a + 2\sqrt{1+a}. \tag{2.41}$$

Note that $x_{\text{mb}}^{-} > 2$, and recall from our discussion in Sec. (2.2) that any orbit that approaches the black hole more than the marginally bound orbit is either unbound or plunges. This implies that the phase-space for counter-rotating orbits will vanish beyond x_{mb}^{-}. In particular, there are no counter-rotating orbits inside of the ergosphere, as stated previously.

In order to find the marginally bound co-rotating orbit, we calculate x_- for each of the positive angular momenta obtained in Eq. (2.40) The solution for $L_z = a$ occurs at $x = 0$, which is clearly not physical. The solutions for $L_z = \Big(\pm 1 \mp \sqrt{1 \mp a}\Big)$ are located at $x = 2 \pm a - 2\sqrt{1 \pm a}$, which are inside the event horizon. The only physical solution is

$$x_{\text{mb}}^{+} = 2 - a + 2\sqrt{1-a}. \tag{2.42}$$

Note that, unlike counter-rotating orbits, co-rotating orbits *can* extend into the ergoregion for sufficiently large spin parameters.

2.3.1.2 Calculating the Currents

Now that we know how to find the minimum energy, we can go back to Eq. (2.31) and do the integration over L_z, which gives

$$J_t = \frac{4f_{\text{eq}}}{\sqrt{r}} \int_{\mathcal{E}_{\text{min}}}^{1} \mathrm{d}\mathcal{E}\, \mathcal{E} \mathfrak{I}_t(\mathcal{E}), \tag{2.43a}$$

$$J_\phi = \frac{4f_{\text{eq}}}{\sqrt{r}} \int_{\mathcal{E}_{\text{min}}}^{1} \mathrm{d}\mathcal{E}\, \mathfrak{I}_\phi(\mathcal{E}), \tag{2.43b}$$

with

$$\begin{aligned}
\mathfrak{I}_t(\mathcal{E}) = {} & \frac{2}{\sqrt{|x-2|}} \left[\theta\Big(x - x_{\text{mb}}^+\Big)\left(\theta(x-2)\arctan\frac{1}{\sqrt{\kappa^+}} + \theta(2-x)\,\operatorname{arctanh}\frac{1}{\sqrt{-\kappa^+}}\right)\right. \\
& \left. + \quad \theta\Big(x - x_{\text{mb}}^-\Big)\arctan\frac{1}{\sqrt{\kappa^- - 1}}\right], \\
\mathfrak{I}_\phi(\mathcal{E}) = {} & \frac{1}{\sqrt{|x-2|}} \left[\theta\Big(x - x_{\text{mb}}^+\Big)\left(\theta(x-2)\left\{\Big(L_z^+ + L_z^-\Big)\arctan\frac{1}{\sqrt{\kappa^+}} + \sqrt{\Big(L_z^+ - L_z^{\text{crit},+}\Big)\Big(L_z^{\text{crit},+} - L_z^-\Big)}\right\}\right.\right. \\
& \left. + \theta(2-x)\left\{\Big(L_z^+ + L_z^-\Big)\operatorname{arctanh}\frac{1}{\sqrt{-\kappa^+}} - \sqrt{\Big(L_z^{\text{crit},+} - L_z^+\Big)\Big(L_z^{\text{crit},+} - L_z^-\Big)}\right\}\right) \\
& \left. + \theta\Big(x - x_{\text{mb}}^-\Big)\left\{\Big(L_z^+ + L_z^-\Big)\arctan\frac{1}{\sqrt{\kappa^- - 1}} - \sqrt{\Big(L_z^+ - L_z^{\text{crit,-}}\Big)\Big(L_z^{\text{crit,-}} - L_z^-\Big)}\right\}\right],
\end{aligned} \tag{2.44}$$

where we have defined

$$\kappa^+ \equiv \frac{L_z^{\text{crit},+} - L_z^-}{L_z^+ - L_z^{\text{crit},+}} \qquad \kappa^- \equiv \frac{L_z^+ - L_z^-}{L_z^{\text{crit,-}} - L_z^-}, \tag{2.45}$$

And $\theta(x)$ is the Heaviside function. The Heaviside functions are inserted to make sure that the co-rotating and counter-rotating contributions to the currents vanish at the appropriate points, as well as to take into account a change in form for the co-rotating current that happens inside of the ergosphere. Fig. (2.5) shows the results of the calculation for the density. The takeaway is that increasing the spin parameter increases the density, and

Fig. (2.6) is helpful in understanding the physical origin of this effect. As that figure shows, the density enhancement is coming from co-rotating orbits, which are more deeply bound to the black hole due to the "spin-orbit" coupling mentioned at the beginning of this section. This can be further understood by analyzing the circular orbit energy, displayed in Fig. (2.7).

Gondolo and Silk [1] have shown that, in their non-relativistic framework, the density is proportional to the binding energy of a circular orbit to the power 3/2. This turns out to also provide a good fit to our calculations, and it makes the physical origin of the density enhancement very clear - it is due to the increased binding of co-rotating orbits, which can come closer to the black hole than in the Schwarzschild case. Counter-rotating orbits are only mildly suppressed, as their binding energy is only slightly lowered. It is important to note that the boost obtained here is amplified by the fact that the co-rotating equatorial orbits are the most bound to the black hole, but when we integrate over the full phase space, the net effect will be the same.

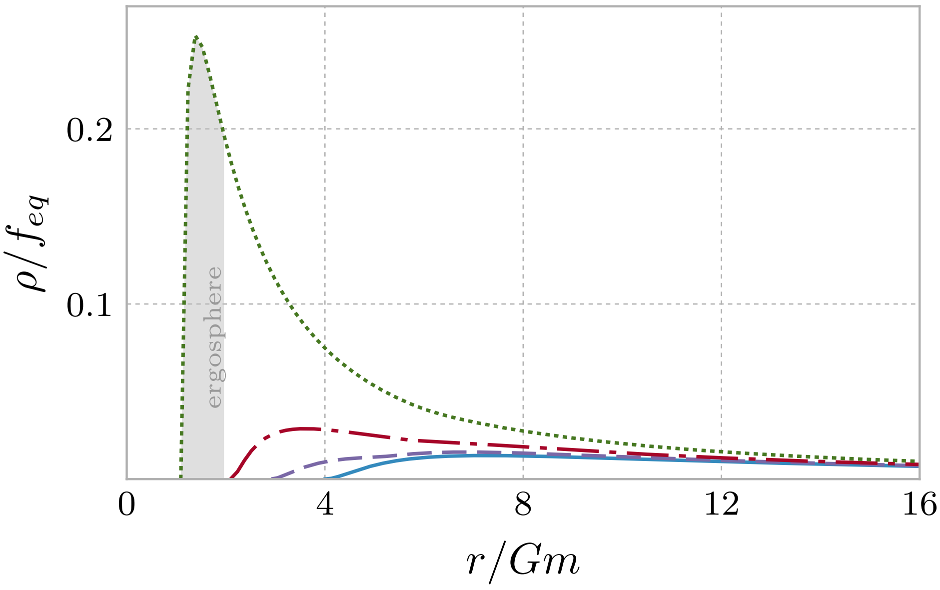

Fig. 2.5: Density profiles for a distribution of equatorial orbits. The density increases as we vary the Kerr parameter $a = 0$ (solid), 0.5 (dashed), 0.8 (dot-dashed) and 0.998 (dotted). Since the latter value is greater than $a > 2\left(\sqrt{2} - 1\right)$, the spike extends into the ergosphere (shaded region).

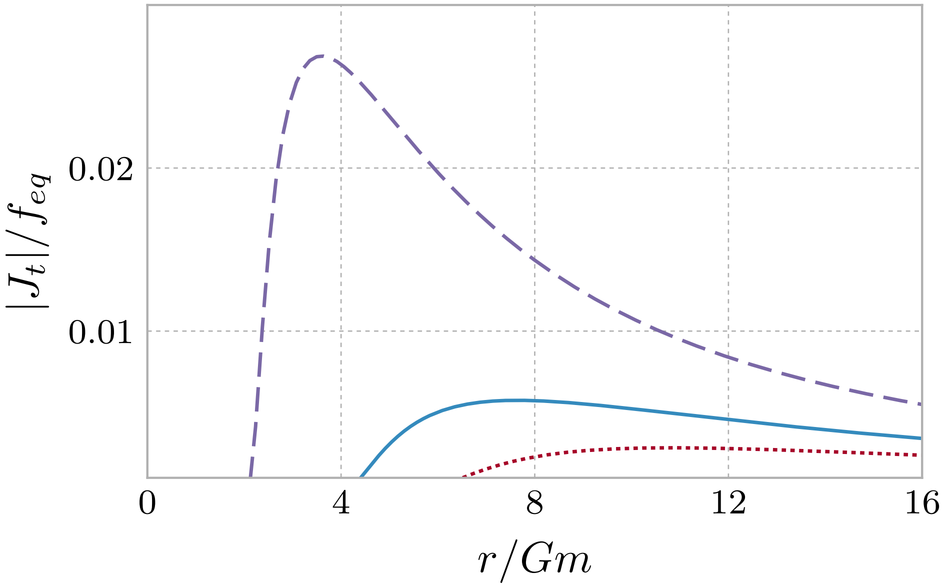

Fig. 2.6: The corotating (dashed) and counter-rotating (dotted) parts of $|J_t|$ for $a = 0.8$, compared with $|J_t|/2$ for the Schwarzschild case (solid).

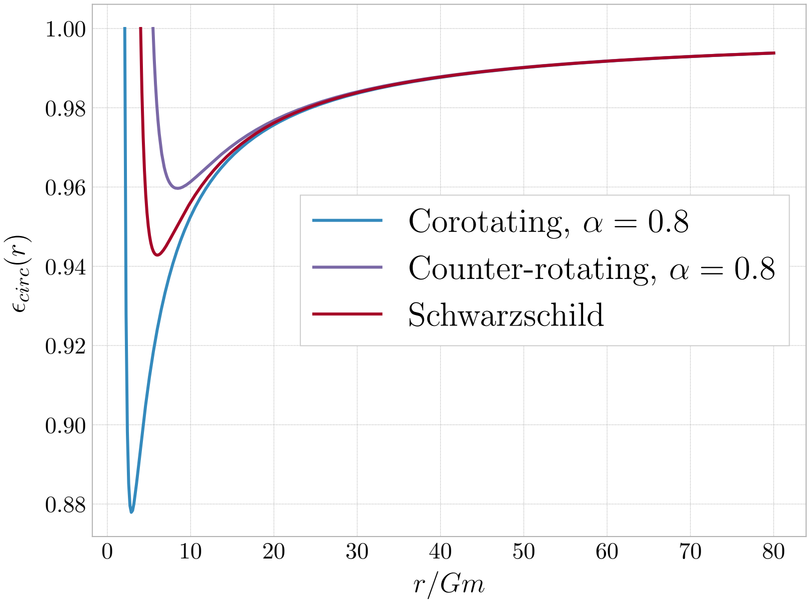

Fig. 2.7: Circular orbit energy for co-rotating (blue) and counter-rotating (purple) orbits with $a = 0.8$, compared to the circular orbit energy for a Schwarzschild black hole (red)

2.3.2 Full Phase Space

Now that we have obtained a strong understanding of the physical origins of the increased density, we will calculate the currents for a constant phase space distribution by integrating over the full phase space, $f(\mathcal{E}, C, L_z) \to f_0$. For a constant phase space distribution, GS can perform their calculation exactly, obtaining $\rho \propto r^{-3/2}(1 - 8Gm/r)^{3/2}$ [1] for the density obtained from a cored profile. The term $8Gm/r$ is the binding energy of the circular orbit of the circular orbit that get captured by the black hole. Motivated by this, we propose a functional form to fit the Schwarzschild result —obtained by taking the $a \to 0$ limit in Eq. (2.13) —in which the binding energy of circular orbits determines the main features of the density profile,

$$\rho(r) = \frac{4\pi}{3}(2\alpha_0)^{3/2} f_0 \frac{(1 - \mathcal{E}_{\rm circ}(r))^{3/2}}{\left(1 + \frac{4Gm}{r}\right)^{\beta_0}}, \tag{2.46}$$

where $\mathcal{E}_{\rm circ}$ is the energy of a circular orbit at coordinate r. We obtain a fit that is reasonable for astrophysical purposes ($\sim 5\%$ errors) with $\alpha_0 = 2.07$ and $\beta_0 = 2.247$. A similar fit can be obtained for the Kerr metric by letting $\mathcal{E}_{\rm circ} \to \mathcal{E}_{\rm min}(r, \theta)$ and changing the denominator by letting $(1 + 4Gm/r)^{\beta_0} \to (1 + (r^+_{\rm mb}(\theta) + a)/r)^{\beta_1}(1 + (r^-_{\rm mb}(\theta) + a)/r)^{\beta_2}$, with β_1, β_2 free parameters and $r^\pm_{\rm mb}$ the co-rotating and counter-rotating marginally bound orbits. This result is displayed here simply to emphasize the dependence of the density on the binding energy of a particle orbiting the black hole, which, as shown in Fig. (2.7), increases dramatically with the spin parameter, leading to a net increase in the density, even once the preferential capture of counter-rotating orbits, displayed in Fig. (2.3) is included.

As mentioned in Sec. (2.2), the boundaries of the phase space volume are not known analytically, and we use MC integration in order to efficiently sample the phase space and extract an estimate for the currents. We used the VEGAS algorithm as implemented by the CUBA library [63], and verified that the evaluation of the currents led to a Gaussian distribution of results, implying that the error estimates given by the program are reliable. Since astrophysical uncertainties are frequently very large, we decided that a 1% numerical error for the current components is acceptable.

Now, given a spin parameter α and an inclination θ, we have all the necessary tools to calculate the current density for any $r > r_{\min}(\theta)$, and sample results are displayed in Figs. (2.8) and (2.9), where, following previous work [52], we used $f(\mathcal{E}, C, L_z) = f_0 = \frac{0.3 \text{ GeV/cm}^3}{(2\pi(100 \text{ km/s})^2)^{3/2}} = 5.1 \times 10^8 \text{ GeV/cm}^3$. Dimensionally, $f_0 \sim \rho/v^3$, so the value we took is motivated by measurements of the local dark matter density and what we expect the velocity dispersion to be. The exact value comes from assuming that the phase space distribution is gaussian. Fig. (2.10) provides a pictorial illustration of the density distribution in two dimensions, making it clearer where the spike is most enhanced.

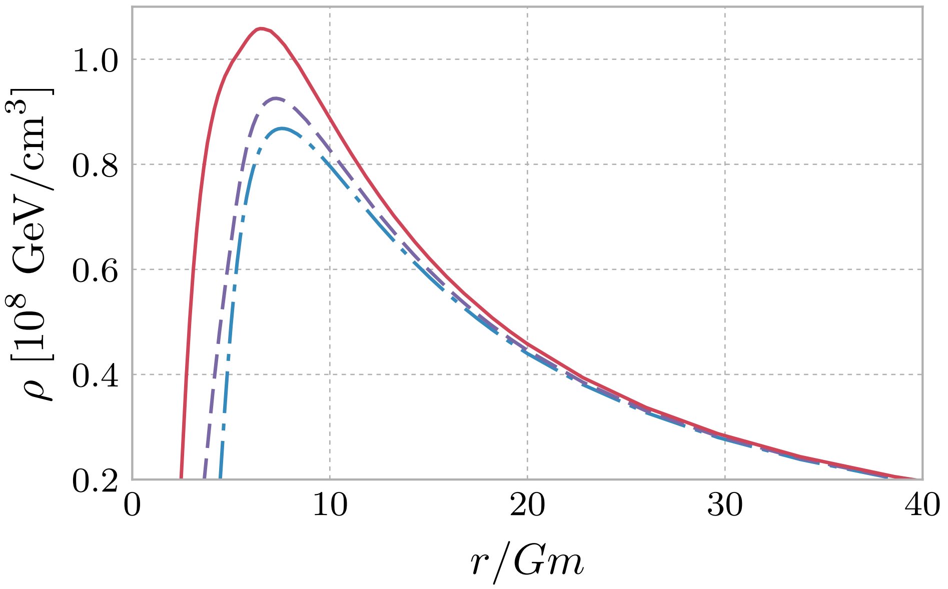

Fig. 2.8: The dark matter density in the equatorial plane increases with the spin parameter, and the spike gets closer to the hole. The different lines show the Schwarzschild calculation from SFW (blue, dot-dashed), $\alpha = 0.5$ (purple, dashed), and $\alpha = 0.8$ (red, solid).

We observe that the density decreases as we get away from the equatorial plane, which is expected: recall that an orbit can only cross the axis if $L_z = 0$ and, unlike the spherical case, in which the components L_x and L_y of the angular momentum were also conserved, this restriction effectively reduces the available phase space and, consequently, the density.

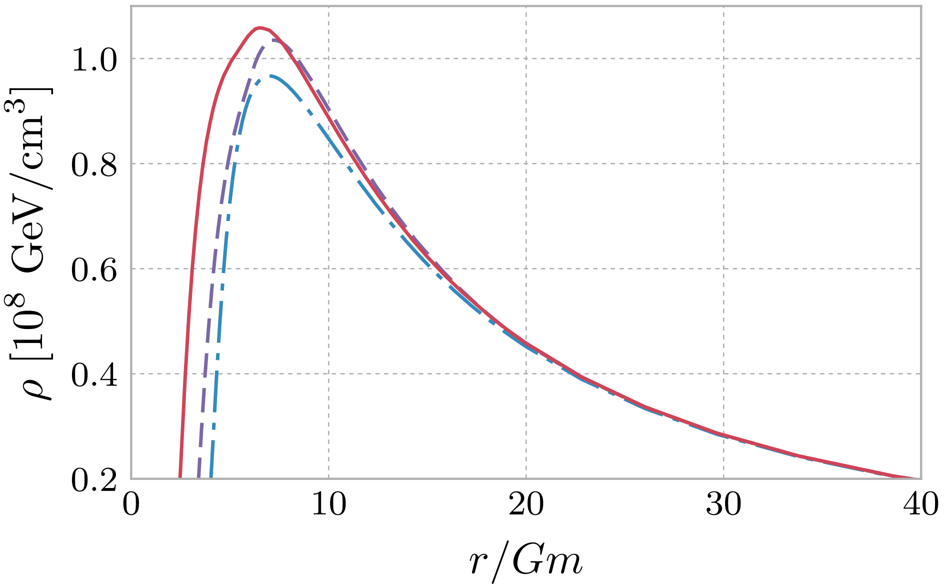

Fig. 2.9: Density anisotropy for $\alpha = 0.8$. The spike is shown at different angles with respect to the black hole rotation axis: on axis $\theta = 0$ (blue, dot-dashed), $\theta = \pi/3$ (purple, dashed) and equatorial $\theta = \pi/2$ (red, solid).

In fact, for axial orbits we can perform some of the integrations explicitly by using the substitutions in Eq. (2.27) and obtain an expression for J_t as

$$J_t = \frac{4\pi f_0}{\sqrt{\Delta}} \int_{\mathcal{E}_{\min}}^{1} \mathrm{d}\mathcal{E}\, \mathcal{E} \sqrt{C_{\max}(\mathcal{E}) - C_{\mathrm{crit}}(\mathcal{E})}, \tag{2.47}$$

Where, as usual, $C_{\max}$ is obtained from $V(r) = 0$ and C_{crit} is the critical Carter constant. As mentioned in Sec. (2.2), we find the critical Carter constant by solving a polynomial equation, and the density can be easily obtained from Eq. (2.14) by setting $\Omega = 0$. We use this explicit, more numerically reliable form of the current along the axis to check that the MC integration has the appropriate limit as $\theta \to 0$.

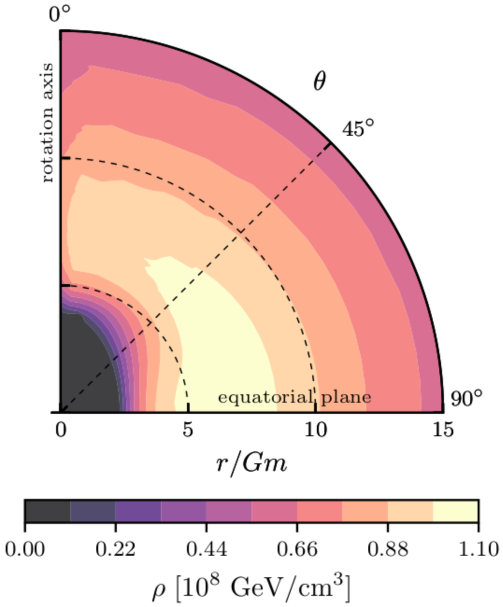

Fig. 2.10: Dark matter density in the $r - \theta$ plane for a spin parameter $\alpha = 0.8$, and a constant initial distribution function. The axis of the black hole points vertically, and r/Gm is plotted from 0 to 15. The density is axisymmetric about the spin axis.

2.4 Adiabatic Matching

2.4.1 Adiabatic Invariants

We will now apply the formalism of adiabatic black hole growth to the determination of the phase-space distribution $f(\mathcal{E}, C, L_z)$. Prior to the formation of the black hole, we will assume that the dark matter is distributed according to a density profile $\rho_i(r)$, which we will take to be spherically symmetric. This density generates a gravitational potential $\Phi(r)$, and a phase space distribution $f_{\rm NR}(E)$ may be determined from it using Eddington's method [31], where E is the non-relativistic total energy, which is negative for a bound orbit. Since the potential has spherical symmetry, particle orbits moving under its influence have three conserved quantities: the total energy E, the total angular momentum L, and the z-component of the angular momentum, L_z. From these, we can calculate the action variables for bound orbits

$$I_r = \oint \mathrm{d}r\, p_r = \int \mathrm{d}r\, \sqrt{2(E - \Phi(r) - L^2/r^2)}, \tag{2.48a}$$

$$I_\theta = \oint \mathrm{d}\theta\, p_\theta = \int \mathrm{d}\theta\, \sqrt{L^2 - \frac{L_z^2}{\sin^2\theta}} = 2\pi(L - |L_z|), \tag{2.48b}$$

$$I_\phi = \oint \mathrm{d}\phi\, p_\phi = 2\pi L_z. \tag{2.48c}$$

From the Kerr metric, Eq. (2.9), we can calculate the canonical momenta for a geodesic orbit, and using Eqs. (2.10) we can write the action variables in terms of the constants of the motion as follows

$$I_r^K(\mathcal{E}, C, L_z) = \oint \mathrm{d}r\, p_r = \int \mathrm{d}r\, \frac{r^2}{\Delta} V(r)^{1/2}, \tag{2.49a}$$

$$I_\theta^K(\mathcal{E}, C, L_z) = \oint \mathrm{d}\theta\, p_\theta = \int \mathrm{d}\theta\, U(\theta)^{1/2}, \tag{2.49b}$$

$$I_\phi^K = \oint \mathrm{d}\phi\, p_\phi = 2\pi L_z. \tag{2.49c}$$

There are some subtleties in the numerical evaluation of I_r^K, I_θ^K, which we now outline. To evaluate the angular integral, we begin by performing a change of variable $v = \cos\theta$. The angular turning points of $U(\theta)$ can be found by setting $U(\theta) = 0$, which gives rise to a quartic equation in v having the following solutions

$$v^2 = \frac{C + a^2(1-\mathcal{E}^2) \pm \sqrt{(C + a^2(1-\mathcal{E}^2))^2 - 4a^2(1-\mathcal{E}^2)(C - L_z^2)}}{2a^2(1-\mathcal{E}^2)}. \tag{2.50}$$

In the $\mathcal{E} \to 1$ limit, the solution is simply $v = \sqrt{1 - L_z^2/C}$, and so we need to make sure to pick the solution that joins smoothly to that limit, which is the solution with the minus sign. The subtraction can also be numerically problematic, and so we use the following equivalent expression for v

$$v^2 = \frac{2(C - L_z^2)}{C + a^2(1-\mathcal{E}^2) + \sqrt{(C + a^2(1-\mathcal{E}^2))^2 - 4a^2(1-\mathcal{E}^2)(C - L_z^2)}}. \tag{2.51}$$

We will refer to this root as v_f, and we will define the second root of Eq. (2.50) as v_2. The orbit is limited by $-v_f \leq v \leq v_f$, but the symmetry of the integrand allows us to integrate in the $0 \leq v \leq v_f$ domain. The last step is to perform the change of variable $v = wv_f$, which maps our integration interval to $[0, 1]$. The final result is

$$I_\theta^K(\mathcal{E}, C, L_z) = 4av_f^2\sqrt{1-\mathcal{E}^2}\int_0^1 \frac{\mathrm{d}w}{\sqrt{1 - w^2v_f^2}}\sqrt{(1-w^2)(v_2^2 - w^2v_f^2)}. \tag{2.52}$$

To evaluate the radial invariant, we recall that the potential can be written as $V(r) = p(r)/r^4$, with p a polynomial. We will factor $p(r) = (1-\mathcal{E}^2)(r - r_1)(r - r_2)(r - r_3)(r_4 - r)$, where r_i are the roots of p, ordered so that $r_1 < r_2 < r_3 < r_4$. In general, our orbit is confined to $r_3 \leq r \leq r_4$, see Fig. (2.2) for reference: the root r_1 is always within the event horizon, and the "orbit" $r_1 \leq r \leq r_2$ is unphysical. The physical orbit is between the two larger roots r_3 and r_4. We have written $p(r)$ in a way that explicitly shows that $V(r) > 0$ at all points in the bound orbit. If we then change the integration variable by $r = wr_4 + (1 - w)r_3$, we can evaluate the radial integral as

$$I_r^K(\mathcal{E}, C, L_z) = \sqrt{1-\mathcal{E}^2}(r_4 - r_3)^2\int_0^1 \frac{\mathrm{d}w}{\Delta(w)}\sqrt{w(1-w)(r(w) - r_1)(r(w) - r_2)}. \tag{2.53}$$

Now that we have a simple way to evaluate the action integrals numerically, we will use them in the process of *adiabatic matching* to obtain an expression for $f(\mathcal{E}, C, L_z)$. It is well known from classical mechanics that the action variables are constant under adiabatic evolution of a system [64], and the other fact that we will need in our calculation is the invariance of the distribution function, first established by Young [45] in the non-relativistic case.

The invariance of the distribution function, which we will establish in the following section, means that we can find $f(\mathcal{E}, C, L_z)$ by solving the equations $I_i^K(\mathcal{E}, C, L_z) = I_i(E', L', L_z')$ for E', L', L_z' and then setting $f(\mathcal{E}, C, L_z) = f_{\mathrm{NR}}(E')$. The fact that two of the invariants for the non-relativistic actions can be calculated in closed form makes this procedure straightforward. We being by noting that the Kerr metric is axisymmetric, so, as expected, L_z will be conserved. Next, we can find L' by setting $L' = |L_z| + I_\theta^K/(2\pi)$. Once L' and L_z' have been determined, the equation $I_r = I_r^K$ is a one-dimensional problem, which can be solved using standard methods such as bisection.

2.4.2 Invariance of the Phase-Space distribution

Before we begin applying this formalism to find the effect of a central black hole on astrophysically relevant dark matter distributions, we will finish this chapter by proving that the distribution function f remains invariant during adiabatic evolution. In order to make the following arguments clearer, we will present a brief discussion of Liouville's theorem in classical mechanics (see, e.g [64] for a review of all the facts stated in this section), which states that the phase space distribution $f(q, p)$ for a mechanical system evolving under the influence of a time-independent hamiltonian H satisfies

$$\frac{\partial f}{\partial t} = -\{f, H\}, \tag{2.54}$$

with $\{\,,\}$ the Poisson bracket. This statement follows from the uniqueness of solutions of Hamilton's equations, which implies that trajectories in phase space do not cross, as well as the fact that hamiltonian evolution is divergenceless in the following sense: given a hamiltonian $H(q, p)$, Hamilton's equations read

$$\dot{q} = \frac{\partial H}{\partial p} \qquad \dot{p} = -\frac{\partial H}{\partial q}. \tag{2.55}$$

Thus, a hamiltonian defines a vector field in phase space (q, p) that can be seen as the analogous to the velocity field of a fluid. From Hamilton's equations (2.55), it follows that this field is divergenceless, i.e

$$\frac{\partial \dot{q}}{\partial q} + \frac{\partial \dot{p}}{\partial p} = \frac{\partial^2 H}{\partial q \partial p} - \frac{\partial^2 H}{\partial p \partial q} = 0. \tag{2.56}$$

The divergence-free character of this velocity field implies that evolution driven by it is volume preserving. Thus, a given phase-space region Ω will evolve into a different region $\Omega'(t)$ that has the same volume. Constancy of the distribution function f can now be established by using the uniqueness of solutions: a given region Ω will have a number of particles $\mathrm{d}N = f\,\mathrm{d}q\,\mathrm{d}p$ inside of it. Under time evolution, $\Omega \to \Omega'$, and no trajectories are allowed to leave the volume $\Omega(t)$: if they did, they would have to cross with a different trajectory, violating the uniqueness of solutions. Thus, $\mathrm{d}N'(t) = \mathrm{d}N$. Moreover, due to the volume preserving character of hamiltonian evolution, $\mathrm{d}p\,(t)\,\mathrm{d}q\,(t) = \mathrm{d}q\,\mathrm{d}p$, from which $f(q(t), p(t), t) = f(q, p, 0)$, proving the constancy of the distribution.

There is another way to view this result which is particularly helpful in what follows: if we lump the phase space coordinates (q, p) into a single vector η, Hamilton's equations may be written as

$$\dot{\eta_i} = \{\eta_i, H\}. \tag{2.57}$$

Under an infinitesimal canonical transformation, we have $\delta\eta_i = \epsilon\{\eta_i, G\}$, where G is a generating function of the transformation. Infinitesimal canonical transformations take $\eta \to \eta'$, and are volume preserving, i.e $\left|\frac{\partial \eta}{\partial \eta'}\right| = 1$. Thus, time evolution may be viewed as a canonical transformation of phase space into itself, taking coordinates $(q, p) \to (q(t), p(t))$. Since canonical transformations are volume preserving, this "coordinate transformation" will also be volume preserving.

Our proof of the adiabatic invariance of the distribution function will therefore simply consist of computing the appropriate jacobian determinant connecting two different sets of canonical coordinates and showing that it is, in fact, 1. What makes this step in our time-dependent problem permissible is the assumption of slow evolution of the Hamiltonian: if

$H(q,p)$ also depends on time, it is not guaranteed that trajectories in phase space will not cross as they evolve in time. However, under adiabatic evolution, the constancy of the action variables guarantees that trajectories remain separated. In order to cross, two trajectories would have to have the same action variables, but initially, the triplet I_r, I_θ, I_ϕ uniquely labels each orbit.

The application of these ideas to our system reads as follows: before the black hole forms, we have a certain set of stationary states labeled by their conserved quantities E, L, L_z. If the growth of the black hole is adiabatic, we know that each trajectory will be uniquely mapped into another stationary state labeled by $\mathcal{E}, C, L_z$. The total energy will change due to the addition of a new source of gravitational potential, the black hole, and the total angular momentum will change because the final metric is not spherically symmetric, meaning that the black hole will exert a torque on DM particles, but it will not change L_z. This means that, if $N(\mathcal{E}, C, L_z)$ is the number of particles per unit constants of the motion, we are guaranteed to have

$$N(\mathcal{E}, C, L_z)\,\mathrm{d}\mathcal{E}\,\mathrm{d}C\,\mathrm{d}L_z = N(E, L, L_z)\,\mathrm{d}E\,\mathrm{d}L\,\mathrm{d}L_z\,. \tag{2.58}$$

All that is required of us is to then prove that the volume of the phase space elements before and after the growth of the BH are the same.

Before we prove our result using the full relativistic machinery and the Kerr metric, we will present a sketch of the derivation for the non-relativistic case. In that case, we can find $N(E, L)$ by

$$\begin{aligned} N(E,L) &= \frac{4\pi}{r^2} L f(E,L) \times 4\pi r^2 \int \mathrm{d}r \, \frac{1}{\underbrace{\sqrt{2(E-\Phi(r)) - L^2/r^2}}_{\mathrm{d}r/\mathrm{d}t \text{ for the particle with } (E,L)}} \\ &= 8\pi^2 L P(E,L) f(E,L). \end{aligned} \tag{2.59}$$

We obtain this expression by defining $N(E,L)$ to be such that the total number of particles in the system satisfies [2] $\int \mathrm{d}E\,\mathrm{d}L\,N(E,L) = \int \mathrm{d}^3x\,\rho(\boldsymbol{x})$ and interchanging the order of integration once the expression for ρ obtained in Eq. (2.5) is inserted. $P(E,L)$ is the period of radial motion of the orbit with energy E and angular momentum L. It is also known that $P(E,L) = \frac{\partial I_r(E,L)}{\partial E}$. As the system evolves adiabatically, the gravitational potential evolves, $\Phi \to \Phi^*$ and the energy changes $E \to E^*$, keeping the action integrals constant. We thus have

$$\frac{\mathrm{d}E^*}{\mathrm{d}E} = \frac{\partial I_r}{\partial E}\frac{\partial E^*}{\partial I_r^*} = \frac{P(E,L)}{P^*(E^*,L)}. \tag{2.60}$$

Substituting E^* for E in $N(E,L)\,\mathrm{d}E\,\mathrm{d}L = N(E^*,L)\,\mathrm{d}E^*\,\mathrm{d}L$ and using the fact that Eq. (2.59) applies for both the “starred” and “unstarred” systems, we obtain our final result.

To prove the invariance of the distribution function in the full relativistic formalism, we will start by finding an expression for $N(\mathcal{E},C,L_z)$. To do this, we integrate the current density, Eq. (2.13), to find the total mass[3] enclosed in a hypersurface of constant time. The future-pointing normal vector to the surface is $n_\alpha = -(g^{tt})^{-1/2}\partial_\alpha t$, and the three-dimensional surface element can be written as [65]

$$\mathrm{d}^3S_\alpha = -n_\alpha\sqrt{g_S}\,\mathrm{d}^3x\,, \tag{2.61}$$

where

$$g_S = \frac{\Sigma^4}{\Delta}g_{\phi\phi}, \tag{2.62}$$

is the determinant of the induced metric on the hypersurface. The enclosed mass will there-

---

[2] The non-relativistic phase space distribution is normalized so that its integral over all space gives the total mass. Since we are considering all the DM particles to have the same mass, this identification simply multiplies the particle number by a constant.

[3] Total rest mass: from the discussion of the non-relativistic case, this is seen to be equal to m_χ times the number of particles. Also, recall from the definition of J that it is the mass-current four vector, *not* the energy-current four vector.

fore be

$$\begin{aligned} M &= -\int \mathrm{d}^3 S_\alpha \, J^\alpha \\ &= \int \mathrm{d}r \, \mathrm{d}\theta \, \mathrm{d}\phi \, \frac{\sqrt{g_S}}{\sqrt{-g^{tt}}} \left(g^{tt} J_0 + g^{t\phi} J_\phi \right) \\ &= 2 \int \frac{\mathrm{d}r \, \mathrm{d}\theta \, \mathrm{d}\phi \, \mathrm{d}\mathcal{E} \, \mathrm{d}C \, \mathrm{d}L_z}{r^2 \sin\theta \sqrt{V(r)} \sqrt{U(\theta)}} \frac{\Sigma^2 \sqrt{g_{\phi\phi}}}{\sqrt{-\Delta g^{tt}}} \left(g^{t\phi} L_z - g^{tt} \mathcal{E} \right) f(\mathcal{E}, C, L_z). \end{aligned} \tag{2.63}$$

If we interchange the order of integration, making sure that we respect proper constraints like $V(r) > 0$, we obtain a distribution of particles per unit conserved quantity, $N(\mathcal{E}, C, L_z)$, such that $M = \int \mathrm{d}\mathcal{E} \, \mathrm{d}C \, \mathrm{d}L_z \, N(\mathcal{E}, C, L_z)$. Using the relation $g^{tt} = -g_{\phi\phi}/(\Delta \sin^2\theta)$ for the Kerr metric, this is, explicitly

$$N(\mathcal{E}, C, L_z) = 4\pi \int \frac{\mathrm{d}r \, \mathrm{d}\theta \, \Sigma^2}{r^2 \sqrt{U(\theta)} \sqrt{V(r)}} \left(g^{t\phi} L_z - g^{tt} \mathcal{E} \right) f(\mathcal{E}, C, L_z). \tag{2.64}$$

In this expression, the limits of integration are the radial turning points of $V(r)$ and the angular turning points in $U(\theta)$. Under adiabatic evolution, the constants of the motion will change to $\mathcal{E}^*$, C^*, ${L_z}^*$, such that $N(\mathcal{E}, C, L_z) \, \mathrm{d}\mathcal{E} \, \mathrm{d}C \, \mathrm{d}L_z = N^*(\mathcal{E}^*, C^*, {L_z}^*) \, \mathrm{d}\mathcal{E}^* \, \mathrm{d}C^* \, \mathrm{d}{L_z}^*$.

The new constants of the motion are determined by the invariance of the action integrals in Eq. (2.49). The invariance of I_ϕ gives $L_z = L_z^*$. The remaining two action variables allow us to relate N and N^* by using the chain rule of multivariable calculus

$$\frac{\partial(\mathcal{E}^*, C^*)}{\partial(\mathcal{E}, C)} = \frac{\partial(\mathcal{E}^*, C^*)}{\partial(I_r^*, I_\theta^*)} \frac{\partial(I_r, I_\theta)}{\partial(\mathcal{E}, C)}. \tag{2.65}$$

Taking partial derivatives in Eq. (2.49), we find:

$$\mathfrak{J} \equiv \frac{\partial(I_r, I_\theta)}{\partial(\mathcal{E}, C)} = 2 \int \frac{\mathrm{d}r \, \mathrm{d}\theta \;\; \Sigma^2 (\mathcal{E} g_{\phi\phi} + L_z g_{t\phi})}{r^2 \sin^2\theta \Delta \sqrt{U(\theta)} \sqrt{V(r)}}. \tag{2.66}$$

We now use $g^{tt} = -g_{\phi\phi}/(\Delta \sin^2\theta)$, $g^{t\phi} = g_{t\phi}/(\Delta \sin^2\theta)$. Comparing Eq. (2.66)to Eq. (2.64),we obtain

$$N(\mathcal{E}, C, L_z) = 2\pi\mathfrak{J}\, f(\mathcal{E}, C, L_z), \tag{2.67}$$

with a similar expression for N^*. Equating $N\,\mathrm{d}\mathcal{E}\,\mathrm{d}L_z\,\mathrm{d}C = N^*\,\mathrm{d}\mathcal{E}^*\,\mathrm{d}L_z^*\,\mathrm{d}C^*$ and using Eq. (2.67), we find

$$\begin{aligned}
2\pi\mathfrak{J}\, f(\mathcal{E}, C, L_z)\,\mathrm{d}\mathcal{E}\,\mathrm{d}C\,\mathrm{d}L_z &= 2\pi\mathfrak{J}^*\, f^*(\mathcal{E}^*, C^*, L_z^*)\,\mathrm{d}\mathcal{E}^*\,\mathrm{d}C^*\,\mathrm{d}{L_z}^* \\
&= 2\pi\mathfrak{J}^*\, f^*(\mathcal{E}^*, C^*, L_z^*)\frac{\partial(\mathcal{E}^*, C^*)}{\partial(I_r^*, I_\theta^*)}\frac{\partial(I_r, I_\theta)}{\partial(\mathcal{E}, C)}\,\mathrm{d}\mathcal{E}\,\mathrm{d}C\,\mathrm{d}L_z \\
&= 2\pi\mathfrak{J}^*\, f^*(\mathcal{E}^*, C^*, L_z^*)\frac{\mathfrak{J}}{\mathfrak{J}^*}\,\mathrm{d}\mathcal{E}\,\mathrm{d}C\,\mathrm{d}L_z \\
&= 2\pi\mathfrak{J}\, f^*(\mathcal{E}^*, C^*, L_z^*)\,\mathrm{d}\mathcal{E}\,\mathrm{d}C\,\mathrm{d}L_z\,,
\end{aligned} \tag{2.68}$$

which demonstrates the adiabatic invariance of the distribution function, $f(\mathcal{E}, C, L_z) = f^*(\mathcal{E}^*, C^*, L_z^*)$. We see that the proof hinges on showing that the phase space volume is unchanged between initial and final states. Now that we have established the invariance of the distribution function and have laid out a numerical method for evaluating the relevant action integrals, we will apply this formalism in the following chapters.

Chapter 3

Particle Dark Matter Models

In this chapter we describe some (partially published) work on different approaches to constrain particle DM models. The first one is purely theoretical and is within the framework of a specific model: the NMSSM. Although that section will not mention DM at all, the idea here is that when a complete particle model is proposed, many more constraints are available than the ones described in Chapter 1.

For instance, if the DM is produced by the decay of a heavy particle that couples with the SM, care must be taken so that its decay does not introduce extra relativistic degrees of freedom during nucleosynthesis, as that can change the expansion rate of the universe and, subsequently, the cosmological abundance of ^{4}He.

The constraint we will consider is that of vacuum stability, mentioned in Chapter 1: the extra scalar particles introduced in the NMSSM can destabilize the electroweak vacuum. Since the masses of the W and Z bosons depend on the higgs vacuum expectation value, such models would be excluded.

In a similar vein, if we postulate a DM/SM coupling, the DM that is clustered in galaxies could still have some residual annihilation into SM particles. This residual annihilation could lead to the production of particles like photons and neutrinos that could then propagate all the way to the Earth and be observed. Here, instead of proposing a particle model and deriving specific constraints, we will take an agnostic approach and use the phase space formalism developed in Chapter 2 to calculate the effect of a central SMBH on the central region of a galactic DM halo. This may then be folded into a specific particle model to calculate the fluxes that might be observed. This work has been published in [48].

3.1 Vacuum Stability Constraints On Supersymmetric Dark Matter

3.1.1 The Scalar Potential of The NMSSM

The MSSM has been the subject of intense theoretical and experimental study over the years, and is severely constrained. In particular, the non-observation of any superpartners at the LHC has excluded large areas of the MSSM parameter space have been excluded, mostly the ones that are considered "natural" to have weak-scale SUSY breaking. Restricted to the fields (h_u, h_d), the SUSY preserving part of the MSSM potential is [22]

$$V(h_u, h_d) = |\mu|^2\Big(h_u^2 + h_d^2\Big) + \frac{1}{8}\Big(g^2 + g'^2\Big)\Big(h_u^2 - h_d^2\Big)^2. \tag{3.1}$$

In this equation, g, g' are, respectively, the electroweak gauge couplings in the $\mathrm{SU}(2)_L$ and $\mathrm{U}(1)_Y$ sectors of the SM. From this, it is seen that the global minimum of this potential is at $h_u = h_d = 0$. In the MSSM, electroweak symmetry breaking must therefore be related to SUSY breaking in some way.

This leads to a "naturalness problem" [25] of the MSSM, also known as the "little fine-tuning problem". The argument is as follows: since electroweak symmetry breaking in the MSSM comes from SUSY breaking terms, some "conspiracy" must be at place to ensure that the SUSY-respecting μ-term present in the quadratic Higgs potential combines with the SUSY-breaking terms in such a way that the masses of the W and Z bosons have their correct values. In particular, the SUSY preserving μ parameter is constrained to be around the electroweak scale even though, a priori, there is no relation between the electroweak symmetry breaking scale and the SUSY scale. Therefore, some "fine-tuning" is required in the MSSM to get the correct electroweak symmetry breaking scale.

A way out of this conundrum is to generate the μ-term in the MSSM dynamically, which we will do by adding a new chiral supermultiplet to the theory. This supermultiplet will be an SM singlet and interact only with the higgs fields. The model thus defined, known as the NMSSM, may therefore be seen as a supersymmetric version of the “Higgs-portal” dark matter models, since the fermion part of the chiral supermultiplet may compose the dark matter. We will denote the scalar part of the supermultiplet as s.

The full scalar potential of the NMSSM, including SUSY breaking terms, is [66]

$$\begin{aligned} V(h_u, h_d, s) = &\left(-\lambda h_u h_d + \kappa s^2 + \mu' s + \xi_F\right)^2 + \frac{1}{8}\left(g^2 + g'^2\right)\left(h_u^2 - h_d^2\right)^2 \\ &+ \left(m_{H_u}^2 + (\mu + \lambda s)^2\right) h_u^2 + \left(m_{H_d}^2 + (\mu + \lambda s)\right)^2 h_d^2 \\ &m_s^2 s^2 - 2\lambda A_\lambda h_u h_d s + \frac{2}{3}\kappa A_\kappa s^3 + m_S'^2 s^2 + 2\xi_s s - 2m_3^2 h_u h_d. \end{aligned} \tag{3.2}$$

We have highlighted in red all the NMSSM contributions to the potential. In this equation, we still have an explicit μ-term, but, as seen by the highlighted λs terms, an effective μ-term may be generated dynamically if s acquires a vacuum expectation value. Here we see in practice the effects of introducing more scalars into a theory: by introducing a single scalar field, the scalar potential contains many more free parameters and is significantly more complex. By being defined in a 3D “field space” (h_u, h_d, s), instead of the 2D space (h_u, h_d), we also introduce more extrema in the potential, some of which could have a lower energy than the physical vacuum. Moving forward, we will consider the so called $\mathbb{Z}_3$-invariant NMSSM, in which $\mu = \mu' = \xi_F = m_3^2 = m_S'^2 = \xi_S = 0$.

In the MSSM, the tree-level higgs boson mass is bounded from above by the mass of the Z boson [22], which is observed to be 91.2GeV. Therefore, significant radiative corrections are required to boost the higgs mass to its observed value of 125GeV. This constrains the parameter space of the MSSM, but also introduces significant theoretical uncertainties to the computation of the higgs mass, due to the technical difficulties in computing 2-loop corrections. These are important since the diagrams that dominate the one loop corrections, namely the ones with top-stop loops [25], receive strong interaction corrections at 2-loop order.

The NMSSM provides an interesting mechanism to boost the higgs boson mass at tree level. If we parametrize the (h_u, h_d) vacuum expectation values by $v_u = v\cos\beta, v_d = v\sin\beta$, with v the SM higgs expectation value and β a mixing angle, then the linear combinations $h = h_d\cos\beta + h_u\sin\beta, H = h_d\sin\beta - h_u\cos\beta$ are such that $\langle h\rangle = v, \langle H\rangle = 0$. For simplicity, we will now assume that the H state is heavy and is mostly decoupled from (h, s).

If the s state is lighter than h, the mixing between these two will give rise to level repulsion, boosting the higgs mass already at tree level. This means that radiative corrections do not have to be as large, and this is experimentally interesting because it implies that a second higgs-like state could be close to experimental detection [26]. We will show, however, that vacuum stability can be used to effectively constrain this section of the NMSSM parameter space [67].

3.1.2 Vacuum Stability Analysis

Taking the $\mathbb{Z}_3$-invariant NMSSM Lagrangian from [66], the mass matrix of the model can be approximated to one loop as follows, using the (h, H, s) fields:

$$\begin{aligned}
M^2_{hh} &= M_Z^2\cos^2(2\beta) + \lambda^2v^2\sin^2(2\beta) + (\delta m_h^2) \quad &(3.3)\\
M^2_{HH} &= (M_Z^2 - \lambda^2v^2)\sin^2(2\beta) + \frac{2B\mu}{\sin(2\beta)} \quad &(3.4)\\
M^2_{ss} &= \frac{1}{2}\lambda v^2\sin(2\beta)\left(\frac{\Lambda}{v_s} - 2\kappa\right) + 4\kappa^2v_s^2 + A_\kappa\kappa v_s \quad &(3.5)\\
M^2_{hH} &= \frac{1}{2}(M_Z^2 - \lambda^2v^2)\sin(4\beta) \quad &(3.6)\\
M^2_{hs} &= \lambda v(2\mu - \Lambda\sin(2\beta)) \quad &(3.7)\\
M^2_{Hs} &= \lambda v\Lambda\cos(2\beta). \quad &(3.8)
\end{aligned}$$

In the above equations, $\Lambda = A_\lambda + 2\kappa v_s, B = A_\lambda + \kappa v_s$, and we have highlighted the NMSSM contributions to the mass matrix elements involving the (h, H) scalars that are present in the MSSM. We are writing down this mass matrix in the approximation that only the top-stop loop is important, and it only contributes to δm_h^2 [26]. The radiative correction δm_h^2 is given by

$$\delta m_h^2 = \frac{3g^2 m_t^4}{8\pi m_W^2}\left[\log\left(\frac{M_{\text{SUSY}}^2}{m_t^2}\right) + \frac{X_t^2}{M_{\text{SUSY}}^2}\left(1 - \frac{X_t^2}{12M_{SUSY}^2}\right)\right], \tag{3.9}$$

with $M_{\text{SUSY}}^2 = m_{\tilde{t}_1} m_{\tilde{t}_2}$ and $X_t = A_t - \mu/\tan\beta$.

The model is now parametrized by $\lambda, A_\lambda, \kappa, A_\kappa, \tan\beta, \mu$. We will focus on the small λ region, following Badziak et. al [26]. In this region, $h - s$ mixing at tree level can boost the value of the Higgs-like mass, meaning that we need smaller contributions from radiative corrections, which allows for lighter stops. Note that the λv^2 term already contributes to the higgs mass at tree level, so the higgs mass is not only boosted by mixing with s, but directly by the extra terms in the scalar potential. The reason to consider small λ is to also keep the s mass below the higgs mass of 125GeV, so as to take advantage of the previously mentioned level repulsion.

For fixed $\mu, \tan\beta, \Lambda, \lambda$, we can find the other parameters by fixing the masses of the scalar eigenstates, which provides a more physical parametrization for the model. Once this is done we can proceed to compare each parameter point to experiment. Since our mass matrix was written at one loop and in an approximate form, it is important to check that this parametrization is consistent and the radiative corrections that we ignored are small. We do this using the spectrum generator SPheno [68, 69].

More generally, our purpose here is to check how well this "base-parametrization" can describe regions of the NMSSM model space which give the correct value of the higgs-like scalar mass (within theoretical + experimental uncertainties) and are experimentally viable. Another important check for the model is vacuum stability, which we will show to be very constraining in this region of parameter space.

Rather than performing an extensive parameter scan as in [67], we have chosen to vary

$\tan\beta$ and Λ in our work because they directly parametrize $h-s$ mixing. Also, to reduce the number of free parameters that we are working with, we have taken the limit of no tree-level squark mixing and degenerate soft masses.

We checked the global stability of the vacuum at tree level using HOM4PS2 [70], a software package that can numerically solve polynomial equations in multiple variables. Since the tree level scalar potential is polynomial in the fields, we can use this program to find all complex extrema of the scalar potential. Once we have all of the extrema we can then find the true vacuum and check if the EWSB parameters and the singlet VEV are correctly obtained.

We compared this method with an "NMSSMTools-like" check (see [71] for a reference on NMSSMTools, a popular spectrum calculator for the NMSSM), in which we minimize the potential in the $v_u - v_d$,$v_u - s$ and $v_d - s$ planes and check if any of these "extrema" are at a lower potential then the correct electroweak vacuum. The other check performed is the positivity of all masses squared in the scalar and pseudoscalar sector. The results for each method are shown in Fig. (3.1). We see that the full homotopy calculation is only slightly more constraining than the simple "NMSSMTools-like"check. In Fig. (3.2) we show the values of the higgs-like scalar mass obtained once all radiative corrections are included. We see that our parametrization is adequate for moderate $\tan\beta$ and Λ.

In all of our calculations we consider two different models: "Model 1" sets the masses of the (s,h,H) particles, respectively, to 100GeV, 125GeV, and 500GeV. We also fix $\lambda = 0.06, \mu = 150$GeV. "Model 2" sets the masses of (s,h,H) to 75GeV, 125GeV, and 1000GeV, respectively. We keep $\mu = 150$GeV but set $\lambda = 0.08$. The upper boundary of our plots was considered in [26] as being experimentally interesting. Our analysis shows, however, that vacuum stability would exclude this region, pointing out the importance of performing this calculation.

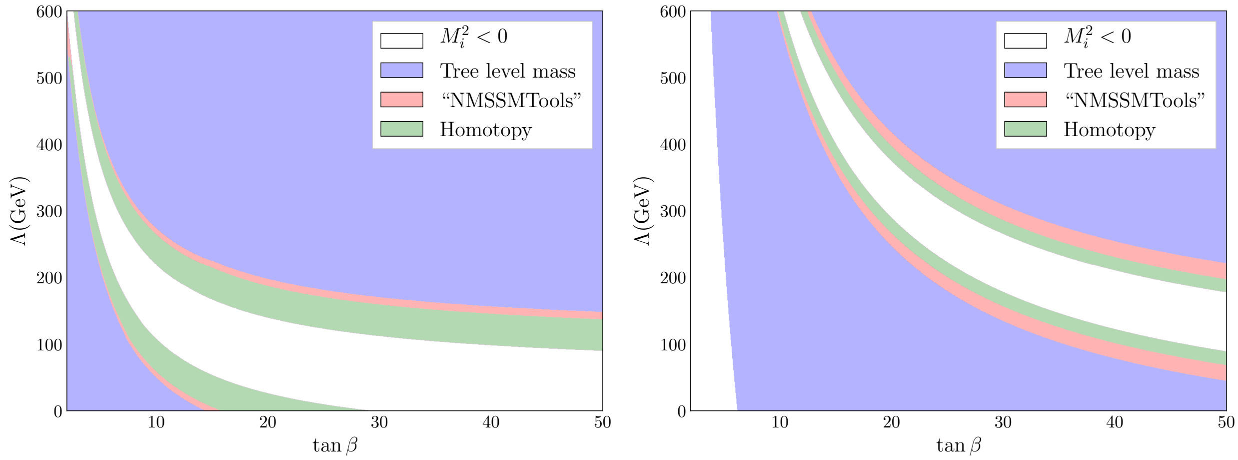

(a) Model 1 **(b)** Model 2

Fig. 3.1: Tree-level analysis of vacuum stability. The colored regions represent the allowed parameter space given by each method. In interpreting this figure it is important to note that the green region is contained in the "NMSSMTools-like" check, and that positivity of masses only excludes the white space.

3.1.3 Comparison with experiment

Using the software HiggsBounds [72, 73, 74, 75] we can quickly go from an the output model file calculated from SPheno, which provides effective couplings, cross-sections and decay rates of a variety of processes, to the experimental data that is publicly available from the. This experimental data consists of LHC and LEP results of searches for new particles in several final states. With a light scalar in the spectrum, we expect that the most stringent constrains would come from LEP searches for higgs-like particles decaying to $b\bar{b}$. However, as emphasized in [26], the small mixing term with the heavy scalar H can suppress the couplings of s to $b\bar{b}$, enabling the LEP constraints to be evaded. In this region, couplings to $c\bar{c}$ are enhanced, and that would be an interesting signature of this model.

Going through the comparison between model predictions and data, we see that the model presented here seems to be severely constrained by experiments, but nevertheless there are small regions that are not excluded at 95%-CL. The experimentally available regions in this model are all close to the edge of the negative mass squared region. Throughout the parameter space that we considered, the particle whose mass squared turns negative in the

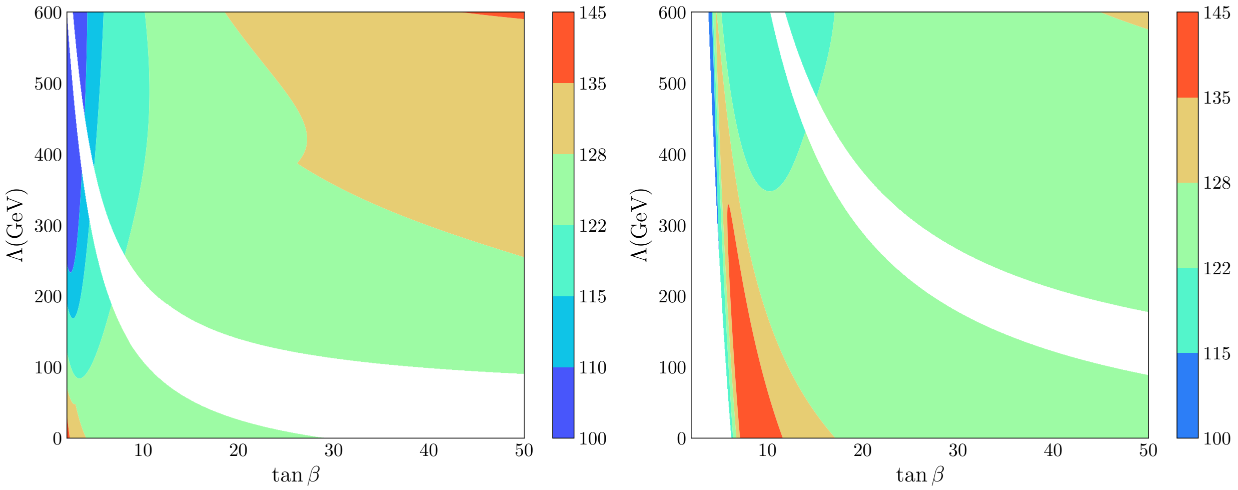

(a) Model 1

(b) Model 2

Fig. 3.2: Self-consistency check for the higgs-like particle mass(in GeV), calculated using SPheno. The green region corresponds to higgs masses that are within theoretical and experimental errors of the observed values.

forbidden regions is one of the pseudoscalar states. This seems to imply that a signature of this model would be a light pseudoscalar particle. Moreover, since negative masses squared are a signal of vacuum instability, this also shows the necessity of performing a more thorough check of vacuum stability through softwares like Vevacious [76], which can find minima of the scalar potential including 1-loop corrections.

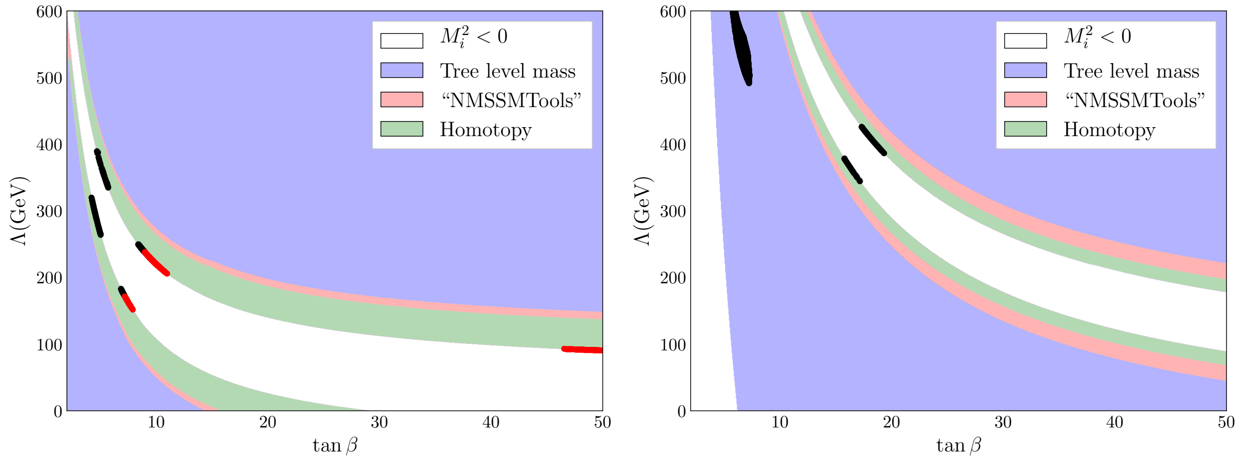

(a) Model 1

(b) Model 2

Fig. 3.3: Comparison with experimental data using HiggsBounds, overlayed on the vacuum stability plot. Red points pass experimental constrains, as well as having a higgs mass within the accepted uncertainty. Black points pass the HiggsBounds tests but do not have an acceptable mass.

3.2 Indirect Detection of Dark Matter Particles

The WIMP paradigm is powerful because it provides concrete tools to take a given theoretical model and deduce observable quantities that can be used to constrain it. Fig. (3.4) shows some simple processes that could be observed if DM particles admit an annihilation channel to the SM sector. An important consequence of this idea is that all of these processes are linked by the crossing symmetries of quantum field theory and observing any of these processes constrains the others (see [77] for some situations where this is not straightforward). Because of this property, these processes are termed *complementary*.

Direct detection experiments consist of looking for the scattering of DM particles with nuclei, and collider production could be observed as missing energy at, say, the LHC. In this thesis, we will be focusing on quantities that affect *indirect detection*, which is the production of SM particles from DM particles, which could be optimally observed from large concentrations of DM that are close by, like in the GC.

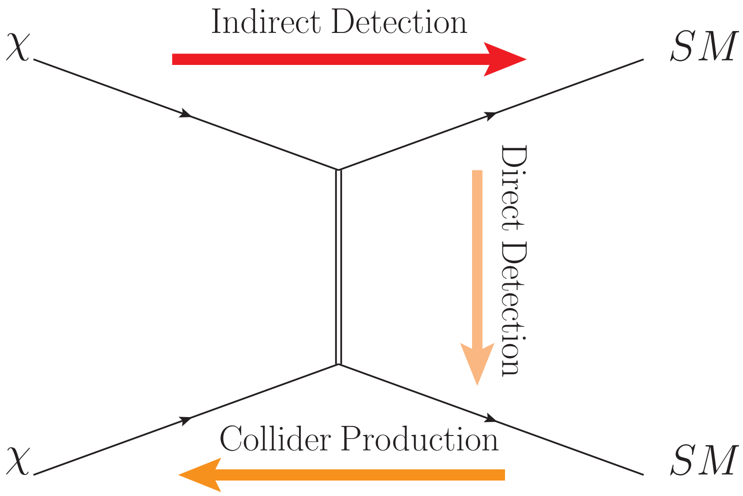

Fig. 3.4: A Feynman diagram schematically showing the different detection channels for DM coupling to the SM.

The indirect detection observable is a particle flux to be detected by a satellite or ground-based observatory. Three quantities are necessary in order to calculate the particle flux from self-annihilation of DM: the velocity averaged cross section $\langle\sigma v\rangle$, the DM density n squared, and the energy spectrum of the final state produced in the annihilation, $\mathrm{d}N_f\,/\,\mathrm{d}E$. A simple “derivation” of the particle flux is as follows. At any point a distance s from the Earth, we will have $n\langle\sigma v\rangle$ DM particles hitting any given DM particle per unit time. There are a total of $n\,\mathrm{d}V/2$ pairs of particles per unit volume. From every collision, only a fraction $\mathrm{d}N_f\,/\,\mathrm{d}E$ of the annihilation products will have energy E and be in the final state f. If we assume that the final state particles are emitted isotropically, then the particle flux is simply the total number of collisions per unit time divided by the area of the sphere between the Earth and the point where annihilations occur, $4\pi s^2$. Using $\mathrm{d}V = s^2\,\mathrm{d}s\,\mathrm{d}\Omega$, we can find the flux coming from a direction Ω by integrating over the distance from the observation point:

$$\frac{\mathrm{d}N_f}{\mathrm{d}t\,\mathrm{d}A\,\mathrm{d}\Omega\,\mathrm{d}E} = \frac{\langle\sigma v\rangle}{8\pi m_\chi^2}\frac{\mathrm{d}N_f}{\mathrm{d}E}\int \mathrm{d}s\,\rho^2(s,\Omega), \tag{3.10}$$

where we introduced the mass density ρ and the DM particle mass m_χ. The integral over s is known as the J-factor or the line-of-sight integral. This equation has one main assumption, namely that $\langle \sigma v \rangle$ is independent of position. This can only happen in two cases. The first one is when $\langle \sigma v \rangle$ is velocity independent, as the velocity distribution is tied to ρ by the Jeans equation. Another possibility, which was considered historically, is that the DM density follows a singular isothermal density profile $\rho \propto r^{-2}$. In this case, the velocity distribution is the same everywhere, which makes the average independent of position [31]. Nevertheless, since DM is non-relativistic, that approximation will hold whenever the main annihilation channel is s-wave.

What is important here is that a separation has been made between the "particle physics dependence" and the "astrophysical dependence" of the flux. As mentioned in Chapter 1, $\langle \sigma v \rangle$ is tied to the observed relic abundance of DM, and its value is therefore constrained to about a factor of a few in any given model. The biggest source of (particle) model dependence in the observed fluxes will be in $\mathrm{d}N_f \,/\, \mathrm{d}E$

Indirect detection thus presents the possibility of, having some idea of ρ and $\langle \sigma v \rangle$ from theory or simulations, providing a detection of DM from spectral signatures of the observed particles. Conversely, given a detection of DM in a collider or direct detection experiment, we would be able to map out the DM distribution in a new way, as well as check our theoretical models for consistency across different interaction channels.

There are several challenges to indirect detection that we glossed over in the above discussion: Eq. (3.10) gives the so-called "prompt spectrum", i.e the energy spectrum of particles that are generated at the source. In order to correctly predict an observed energy spectrum, we need an understanding of the interstellar and intergalactic media over which these particles will propagate. For instance, charged particles will interact with local magnetic fields and radiate energy, and they can also collide with gas particles. If the final state f includes quarks, then their hadronization must also be taken into account.

In order to maximize the J-factor, a DM source should be close to the Earth and also have a high concentration of DM. The most promising source is the GC, but this brings up a different issue, which is that of astrophysical backgrounds. The GC is a very active region over several orders of magnitude in energy, and any attempt of detecting DM through, say, the gamma-ray spectrum of the GC requires understanding the gamma-rays being emitted by all of the astrophysical sources in that region, which is a daunting task. In spite of this, analyses of gamma-ray data from the FERMI satellite have revealed an excess of observed photons relative to models of the known astrophysical backgrounds (see [78] for the first proposed detection of this signal). As mentioned, this is an excess over models of *known* astrophysical backgrounds, and it has been proposed that an unresolved population of millisecond pulsars could account for the reported excess [79].

Explanations for this excess are still being debated. For this reason, dwarf galaxies, which are simple, dark matter dominated systems, are considered a better target for indirect detection of DM, even though their J-factors are smaller than that of the GC. Currently, there are no convincing detections from those targets. That said, such signals are actively being searched and some tentative, but heavily contested, detections, have been made [80].

We finish this chapter by considering an important detail to these calculations: the presence of an adiabatic spike around an IMBH/SMBH could lead to substantially larger fluxes than would be obtained with a simple NFW profile. Although we will be concerned with a Milky Way-like SMBH, the proper scaling of the density profiles with the BH mass has been obtained by GS [1] and it is straightforward to transpose our results to other BH masses.

3.3 Adiabatic Spikes With WIMPs

Previous work on relativistic corrections to adiabatic spikes focused on applying the matching procedure to an initial Hernquist profile [52, 48], which is defined by [81]

$$\rho(r) = \frac{\rho_0}{\left(\frac{r}{r_s}\right)\left(1+\frac{r}{r_s}\right)^3} \qquad \Phi(r) = -\frac{GM}{r_s + r}, \tag{3.11}$$

with $M = 2\pi\rho_0 r_s^3$ the mass of the DM halo, which will be taken to be $M = 10^{12} M_\odot$. The scale radius r_s, which marks where the logarithmic slope of the profile changes, will be taken to be 20kpc, and this fixes ρ_0. This section reports on our work using this initial profile [48], which we focused on to make sure that our code could accurately reproduce previous results before moving on to more general profiles.

The Hernquist model has several attractive features: physically, it has a finite total mass and is astrophysically motivated [82, 81]. Mathematically, the simple form of the potential will make our numerical procedures more straightforward and, more importantly, the phase space distribution function $f_{\mathrm{NR}}(E)$ is known analytically:

$$\begin{aligned} f(E) &= \frac{M}{\sqrt{2}(2\pi)^3 (GMr_s)^{3/2}} \tilde{f}_{\mathrm{H}}(\tilde{\epsilon}) \qquad \tilde{\epsilon} = -\frac{Er_s}{GM}, \\ \tilde{f}_{\mathrm{H}}(\tilde{\epsilon}) &= \frac{\sqrt{\tilde{\epsilon}}}{(1-\tilde{\epsilon}^2)} \left[(1-2\tilde{\epsilon})(8\tilde{\epsilon}^2 - 8\tilde{\epsilon} - 3) + \frac{3\sin^{-1}\sqrt{\tilde{\epsilon}}}{\sqrt{\tilde{\epsilon}(1-\tilde{\epsilon})}} \right]. \end{aligned} \tag{3.12a}$$

The DM halos found in simulations can be better fit by an NFW profile [12], which also has the behavior $\rho \propto 1/r$ at small distances. As pointed out in [47], the slope of the spike is completely determined by the behavior of $f(E)$ for the most bound orbits. Since the Hernquist profile and the NFW profile have similar functional forms at small distances, it is reasonable to expect that they will produce the same spike if properly scaled.

We will define the following dimensionless quantities:

$$x = \frac{r}{r_s} \qquad \tilde{L} = \frac{L}{\sqrt{GMr_s}}. \tag{3.13}$$

In terms of these quantities and $\tilde{\epsilon}$, I_r reads

$$2\sqrt{GMr_s} \int_{x_-}^{x_+} \mathrm{d}x \, \frac{\sqrt{2x^2 - 2\tilde{\epsilon}x^2(1+x) - \tilde{L}^2(1+x)}}{x\sqrt{1+x}}, \tag{3.14}$$

where the limits of integration $x_\pm$ are the (dimensionless) turning points of the motion.

Looking for turning points leads to a cubic equation in x. In general, this equation will have three solutions: the two physical turning points $x_\pm$, and a spurious negative solution x_n. Factoring the polynomial in the square root allows us to write the numerator of Eq. (3.14) as $(2\tilde{\epsilon})^{1/2}((x-x_n)(x-x_-)(x_+-x))^{1/2}$. Doing the change of variable $x = tx_+ + (1-t)x_-$, we find

$$I_r^H = 2\sqrt{2GMr_s\tilde{\epsilon}}(x_+ - x_-)^2 \int_0^1 \mathrm{d}t \, \frac{\sqrt{t(1-t)(x-x_n)}}{x\sqrt{1+x}}. \tag{3.15}$$

To implement the adiabatic matching, we only need an interval in which to constrain $\tilde{\epsilon}$. Orbits that escape to infinity have $\tilde{\epsilon} = 0$, and, since $r_h \leq r_s$, it is reasonable to constrain $\tilde{\epsilon} > 0.01$. The upper bracketing point is more complicated: for $\tilde{\epsilon} = 1$, the cubic equation for the turning points has a single real root, and we cannot evaluate the radial action. We can find the $\tilde{\epsilon}$ for which the potential turns from having three real roots to a single real root by setting the discriminant of the polynomial in the numerator of Eq. (3.14) to 0. The discriminant is

$$D(V) = -4\left(2\tilde{L}^6\tilde{\epsilon} + \tilde{L}^4(4\tilde{\epsilon}(2\tilde{\epsilon}+5)-1) + 8\tilde{L}^2(\tilde{\epsilon}-1)^3\right). \tag{3.16}$$

This polynomial equation can be solved numerically, but it is important to note that $\tilde{L}$ is, in general, small. This is because the relevant angular momentum scale around the black hole is Gm, which, when turned into a dimensionless $\tilde{L}$, will be small. This simply means that we are mostly considering orbits that are very deeply bound in the initial gravitational potential. As such, it is appropriate to look for a series expansion solution for the upper endpoint of our bisection interval as $\tilde{\epsilon} = 1 - a_1\tilde{L}^b + a_2\tilde{L}^{2b} + \ldots$, and keep only the first two terms. A straightforward calculation gives $b = 2/3, a_1 = 3/2, a_2 = 1$. This is a simple expression for the upper endpoint of our bisection method that works very well.

We display the main results of our calculation in Figs. (3.5,3.6,3.7). The first figure shows the effects of increasing the spin parameter on the density in the equatorial plane. The second figure shows how the density varies with angle for fixed spin and, finally, the last figure shows a two-dimensional density plot to give an idea of where the spike is centered. A simple summary of the most extreme effects of the calculation is provided by Fig. (3.8).

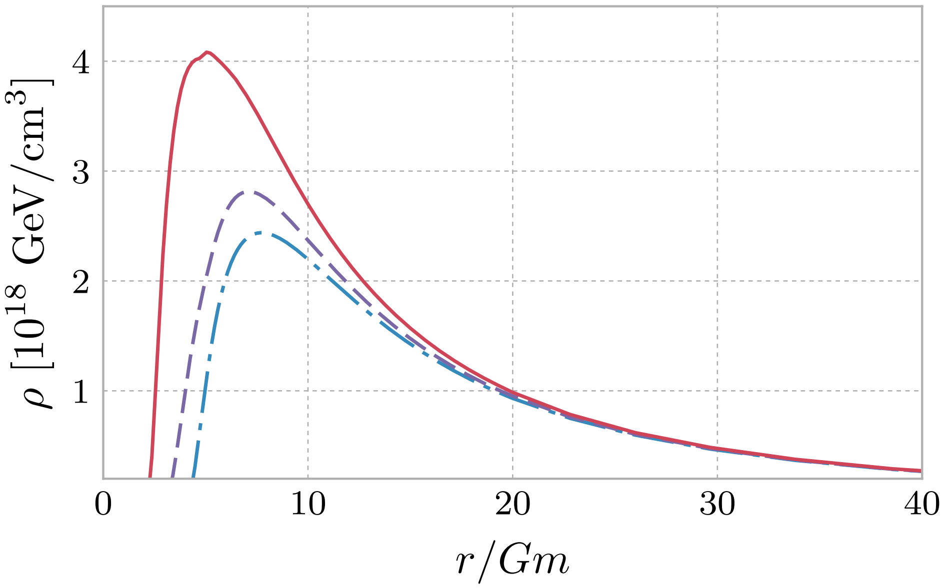

Fig. 3.5: Dark matter density in the equatorial plane with increasing Kerr parameter. The density profile before the black hole grows is given by the Hernquist form described in the text. The different lines show the Schwarzschild calculation from SFW (blue, dot-dashed), $\alpha = 0.5$ (purple, dashed), and $\alpha = 0.8$ (red, solid).

To estimate the effects of the spike on the dark matter annihilation fluxes we compare the line of sight integral for a beam of opening angle $\theta = 1°$ towards the GC, as in [51]

$$J_\alpha(\theta) = \frac{\langle \sigma v \rangle}{4\pi m_\chi^2} \int_0^{2\pi} \mathrm{d}\phi \int_0^{\theta} \mathrm{d}\psi \cos\psi \sin\psi \int \mathrm{d}s\, \rho^2(r, \vartheta), \tag{3.17}$$

with or without the presence of the spike. In Eq. (3.17) $r = \sqrt{R^2 + s^2 - 2Rs\cos\psi}$ is the Boyer-Lindquist coordinate, s is the radial coordinate from the Earth to the annihilation point, $R = 8.5$ kpc is the distance from the Earth to the GC, and ϑ is the angle relative to the equatorial plane of the black hole. We write the J-factor as J_α to emphasize the dependence on the spin parameter of the SMBH when it is present.

We chose the following DM parameters: $\langle \sigma v \rangle = 3 \times 10^{-26}\mathrm{cm}^3/\mathrm{s}$, $m_\chi = 100\mathrm{GeV}$. We

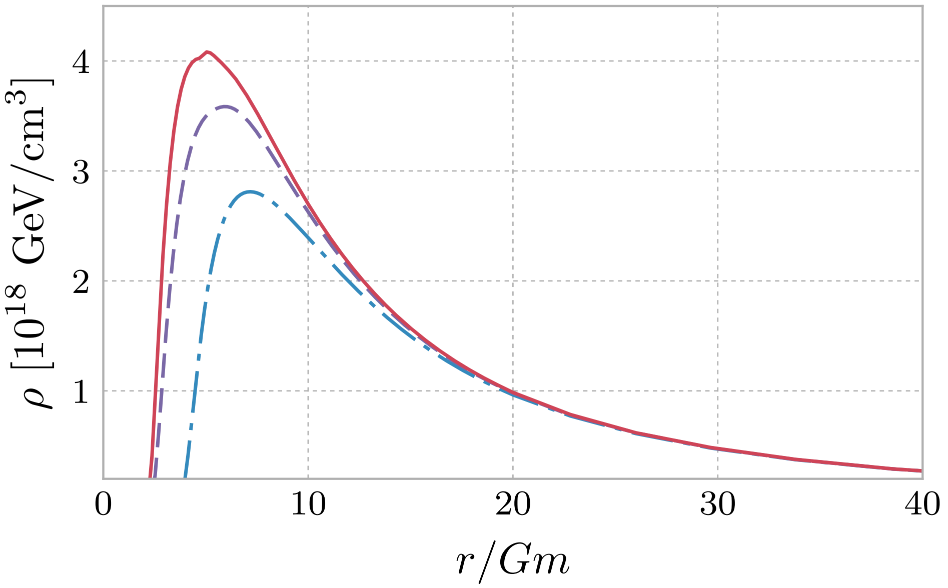

Fig. 3.6: Density anisotropy for an initial Hernquist profile and $\alpha = 0.8$. The spike is shown at different angles with respect to the black hole rotation axis: on axis $\theta = 0$ (blue, dot-dashed), $\theta = \pi/3$ (purple, dashed) and equatorial $\theta = \pi/2$ (red, solid).

then calculated the flux to be 6.3×10^{-9} cm^{-2}s^{-1} for annihilations in the halo with only the underlying Hernquist profile included.

To evaluate the integral in Eq. (3.17), we fit the profiles that were previously calculated using MC techniques to the functional form

$$\rho(r, \vartheta) = \frac{A}{r^p}\left(1 - \frac{r_{\text{min}}(a, \vartheta)}{r}\right)^n, \tag{3.18}$$

with all coefficients being allowed to vary with ϑ. The expression in Eq. (3.18) slightly generalizes Eq. (9) in [1] to allow for a ϑ-dependent end point for the spike. This expression is then matched to the power law $B/r^{\gamma_{\text{sp}}}$ using smooth functions to improve the fit and to give a reasonable estimate of ρ. We use $\gamma_{\text{sp}} = 2.33$ corresponding to the Newtonian spike generated by a $1/r$ NFW or Hernquist cusp [47].

Our calculation of the spike is not self-consistent in two ways: it does not include the effects of the DM distribution on the metric, and it also does not take into account that DM

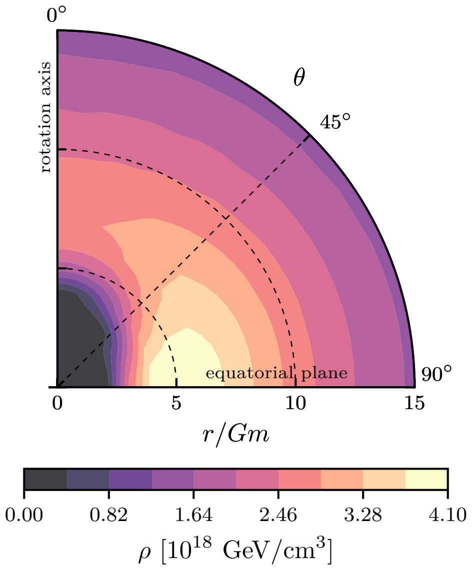

Fig. 3.7: Dark matter density in the $r-\theta$ plane for a spin parameter $\alpha = 0.8$, and an initial distribution function corresponding to a Hernquist profile.

particles that fall into the BH contribute to the final BH mass. Previous studies have shown that both effects are small [47, 45], but not having a self-consistent formalism means that we will not have a correct expression for the spike profile when it begins to transition to the original profile as the DM dominates the gravitational potential. We extend our spike profile until the density is equal to that of the underlying Hernquist profile. This happens at 12.4 pc, and we take the fiducial $1/r$ halo shape beyond this point. Since most of the event rate is dominated by the inner regions of the spike, this does not affect our calculation of $J_\alpha(\theta)$.

Putting all the pieces together, our model for the central part of the halo is equivalent to the canonical model used in [51], aside from the fact that we are assuming an underlying Hernquist profile with $r_s = 20$ kpc and the extension of the spike. For the Schwarzschild geometry, we find a flux that is a factor of 1.93×10^9 higher than when the spike is not present.

In Tab. (3.1) we present the flux enhancement normalized to the Schwarzschild one, as that is less sensitive to the normalization of the underlying density profile. In particular, this quantity also does not depend on the particle physics model.

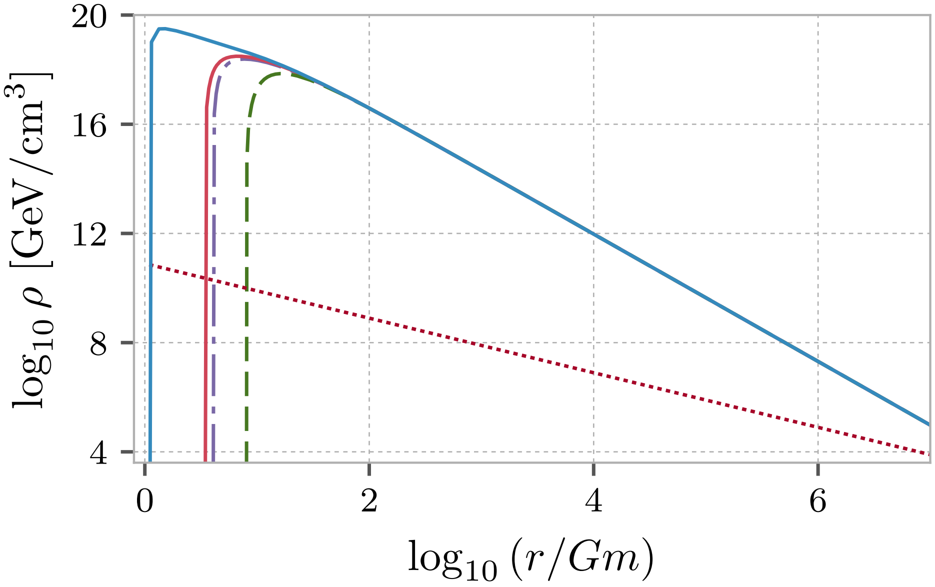

Fig. 3.8: Equatorial (solid blue) and on-axis (solid red) density obtained for the near-extreme black hole, compared with previous calculations assuming a Schwarzschild hole (dot-dashed purple), and the non-relativistic estimate in [1] (dashed green). The black hole grows in an initial Hernquist profile shown as the dotted red line.

Spike	$J_\alpha(\theta)/J_0(\theta)$
$\alpha = 0.5$	1.11
$\alpha = 0.6$	1.14
$\alpha = 0.7$	1.22
$\alpha = 0.8$	1.38
$\alpha = 0.9$	1.59
$\alpha = 0.998$	1.97

Tab. 3.1: Boost factors for different Kerr spin parameters α for the full spike

When the DM density gets as high as it is in our spike profiles, DM can self-annihilate efficiently and level off the spike. SFW followed the strategy used in [1], and considered that the effect of self-annihilation was to form a core within the radius $r_{\rm ann}$ determined by the location where the density equals $\rho_{\rm ann} = m_\chi/\sigma v t_{\rm bh}$, which for our thermal relic turns out to be $r_{\rm ann} = 1.3 \times 10^{-2}$ pc, if we assume that the annihilation process has been acting over $t_{\rm bh} = 10^{10}$ yr.

However, it was pointed out in [83] that a plateau is only in equilibrium if all the dark matter particles move in circular orbits: the proper profile under the influence of DM self-annihilation is actually a "weak cusp" $\rho \propto r^{-1/2}$ for a more realistic isotropic distribution of DM velocities. This behaviour has been confirmed by integrating the Boltzmann equation in [84] for the case of s-wave annihilation.

Regardless of our assumptions on the profile slope once annihilations are included, we should note that a power-law spike of radius R and slope γ has a J-factor $J \propto R^{3-2\gamma}$. As long as $3 > 2\gamma$, J will be dominated by the outer regions of the spike, where particles are non-relativistic, and the effects of GR will not be important. The study done in [51] also shows that the GC does not present a canonical adiabatic spike and, as such, analyses of spike profiles should focus on other sources. If relativistic effects are to be important, moreover, the focus should be on particle physics models that have small interaction cross sections, so that the effect of self-annihilations does not wash out the spike.

Chapter 4

Primordial Black Hole Dark Matter

In this chapter we will review some of the ways in which the abundances of primordial black holes have been constrained by astrophysical observations. The formation mechanisms for PBHs and their relationship to their relic abundance —which may or may not be the cosmological DM density —is highly model dependent and will therefore not be considered.

Instead, we will focus on the inverse problem of constraining the PBH abudance. The LIGO observations of gravitational wave events from black hole mergers can also be used to put strong constraints on the fraction of the DM that is composed of PBHs. We discuss the present-day merger rate of PBHs and how it may be influenced by adiabatic spikes.

4.1 Observational Constraints of PBH DM

In inflationary scenarios, the link between PBH formation and early-universe density fluctuations means that the observation of a PBH population would provide information about these fluctuations [85]. This makes the study of PBHs interesting on its own, and there are several observational limits on the PBH fraction f of the total DM density.

When the LIGO collaboration announced the observation of the first few black hole merger events, the fact that these black holes had a mass on the order of $30M_{\odot}$ seemed difficult to explain astrophysically. Moreover, the existing observational constraints were such that a fraction $f = 1$ of DM in PBHs was still allowed in this mass range. Thus, the possibility that LIGO had made an indirect detection of DM could not be ruled out [32]. Results from [86] added more constraints in the hypothesis of $f = 1$. The current status is that $f = 1$ is excluded except for a small region in which PBHs would have roughly asteroid masses (see [87] for a review, and [88] for work calling into question the femtolensing constraints in the asteroid mass region).

These constraints are computed assuming a monochromatic PBH mass spectrum and, as pointed out in [87], most formation scenarios naturally predict *extended* mass spectra, in which PBHs could play multiple roles. Abundant, low mass PBHs could provide the bulk of the mass that we identify as dark matter, while rare, high mass PBHs could provide the seeds for the density fluctuations that will eventually form galaxies [33]. If this is taken into account, it is still possible that PBHs compose all of the dark matter [87]. This means that PBHs are not yet ruled out as DM candidates, and further investigation is necessary to better constrain their abundances and understand their role, should they exist, in the global picture of cosmological models.

Although the high masses reported by LIGO for the merging BHs are difficult to obtain from stellar evolution, they are not impossible and it is not yet clear what is the contribution to the observed BH merger rate from astrophysical BHs. Without this input, the strongest constraint that can be put on PBH abundances from LIGO observations is that their contribution to the merger rate is not greater than the total measured merger rate. This turns out to be a very strong constraint [89]. We now turn to a description of the basic physics surrounding this phenomenon.

There are two main channels for PBH binaries that are merging at the present time to be formed: they can be formed in the early universe and have a lifetime equal to the Hubble time [89], or they can form in the present day universe and merge [32]. Since PBHs are a form of non-relativistic matter, they should cluster like cold dark matter and are also susceptible to form an adiabatic spike. The spike is relevant for mergers of binaries that form in present day halos [90], so we will consider the formation of those binaries in what follows.

A black hole binary loses energy and angular momentum from the emission of gravitational waves. For high eccentricity orbits, the coalescense time is given in terms of the semi major axis a and eccentricity e by [91]

$$t_{\mathrm{GW}} = \frac{3}{170}\frac{a^4(1-e^2)^{7/2}}{G^3 M_{\mathrm{PBH}}^3} = \left(1.94 \times 10^{13}\mathrm{Gyr}\right)(1-e^2)^{7/2}\left(\frac{a}{1\mathrm{mpc}}\right)^4\left(\frac{M_{\mathrm{PBH}}}{30M_\odot}\right)^{-3}. \tag{4.1}$$

Although this expression is not correct for all eccentricities, the dimensionful factors carry the correct scaling with a and M_{PBH} and also correctly display the fact that eccentric black holes merge much faster that non-eccentric ones. A binary in a Milky Way-like halo, formed from a collision of two $30M_\odot$ BHs, will have a semi major axis on the order of 10^4km (see Eq. (A.12)), which implies a merger timescale of around 1yr, ignoring the eccentricity dependence.

This means that we may calculate the merger rate of PBHs in galactic DM halos as follows: two black holes undergo a gravitational encounter, in which they may radiate their relative kinetic energy in gravitational waves. The cross section for binary formation through this channel is given by [92, 32]

$$\sigma = 1.37 \times 10^{-14}\left(\frac{M_{\mathrm{PBH}}}{30M_\odot}\right)^2\left(\frac{v_{\mathrm{rel}}}{200\mathrm{km/s}}\right)^{-18/7}\mathrm{pc}^2. \tag{4.2}$$

Since the timescale for these BHs to merge is instantaneous compared with cosmological time, all binaries formed in this way promptly merge and can be observed by LIGO. Although binary formation is a non-local event, their semi major axes are so small compared to typical galactic scales that we may consider the capture process as happening at a point. The calculation of the merger rate in a halo could then be performed using Eq. (3.10), provided that the proper averaging over the relative velocity distribution is made.

Due to the ρ^2 dependence of the event rate in Eq. (3.10), the merger rate is very sensitive to PBH clustering. This means that the presence of a density cusp should be taken into account when estimating the merger rate. Such a calculation was performed in [90], where it was shown that, depending on the DM halo parameters, PBH spikes around SMBHs could explain the observed LIGO event rate.

We now turn to a full calculation of the PBH event from binaries formed in an SMBH spike, using the formalism developed in Chapter 2. In particular, we will calculate the local event rate at each point in the spike using Eq. (2.20).

4.2 PBH Mergers In The Local Universe: Adiabatic Spikes

We will take as our model for the initial DM cusp a general power law

$$\rho(r) = \rho_0 \left(\frac{r_0}{r}\right)^{\gamma}, \tag{4.3}$$

With $0 < \gamma < 2$. A power law has no natural length scale, so, in applications, we may take r_0 to be any length and ρ_0 normalizes the density. As an example, if the DM profile of the Milky Way is described as an NFW, the logarithmic slope $\gamma \sim 1$ for $r \lesssim 20$ kpc. If we normalize the density so that in the solar neighborhood, $r \simeq 8$ kpc, $\rho \simeq 0.3$ GeV/cm^3, then it is appropriate to describe the DM density by the above profile with $r_0 = 8$ kpc and $\rho_0 = 0.3$ Gev/cm^3.

The potential $\Phi(r)$ generated by this distribution can be found by solving

$$\begin{aligned} \frac{\mathrm{d}\Phi}{\mathrm{d}r} &= \frac{GM(r)}{r^2}, \qquad \Phi(0) = 0, \\ M(r) &= 4\pi \int_0^r \mathrm{d}r'\, r'^2 \rho(r). \end{aligned} \tag{4.4}$$

For the slopes that we are considering, the total mass is infinite, and as such the potential will be positive and unbounded above. Rather than truncating the distribution and attempting to find a self-consistent phase space distribution that approximates the truncated one, we will simply take this density profile and gravitational potential at face value, as we will be focusing on distances $r \ll r_0$, where any truncation effects will not be relevant[4]. The solution to Poisson's equation is

$$\Phi(r) = \frac{4\pi\rho_0 r_0^{\gamma} r^{2-\gamma}}{(3-\gamma)(2-\gamma)} = \frac{4\pi\rho_0 r_0^2}{(3-\gamma)(2-\gamma)}\left(\frac{r}{r_0}\right)^{2-\gamma} \equiv \phi_0\left(\frac{r}{r_0}\right)^{2-\gamma}. \tag{4.5}$$

The phase space distribution $f(E)$ that generates this initial profile should satisfy the self-consistency condition (see Eq. (2.6))

$$\rho(r) = 4\pi \int\limits_{\Phi(r)}^{\infty} \mathrm{d}E\, f(E)\sqrt{2(E-\Phi(r))}. \tag{4.6}$$

This is slightly different from Eq. (2.6) due to the fact that this potential does not have a finite total mass, and, as such, $\Phi(r) \to \infty$ as $r \to \infty$. Introducing a power-law ansatz $f(E) = f_0 E^{-\beta}$, we can do the integral in Eq. (4.6) analytically, obtaining

$$\begin{aligned} f(E) &= \frac{\rho_0}{(2\pi\phi_0)^{3/2}}\frac{\Gamma(\beta)}{\Gamma(\beta-3/2)}\left(\frac{\phi_0}{E}\right)^{\beta}, \\ \beta &= \frac{6-\gamma}{2(2-\gamma)}. \end{aligned} \tag{4.7}$$

We will introduce the following dimensionless variables

$$x = \frac{r}{r_0} \qquad \epsilon = \frac{E}{\phi_0} \qquad l = \frac{L}{r_0\sqrt{\phi_0}} \qquad l_z = \frac{L_z}{r_0\sqrt{\phi_0}}. \tag{4.8}$$

To calculate the radial action, Eq. (2.48), we need to know the turning points of an orbit given E, L, L_z. These cannot be found analytically, but they can be found through a bracketing algorithm. At a turning point x_t,

$$\epsilon = x_t^{2-\gamma} + \frac{l^2}{2x_t^2}. \tag{4.9}$$

---

[4] A power law profile does not have any characteristic length scale. More rigorously, if we define a truncation scale $r_T \gg r_0$, the proper statement is that we are considering the profile in a region $r \ll r_T$. Since $r_0 \ll r_T$, $r \ll r_0$ naturally implies $r \ll r_T$

Both terms on the right hand side of the above equation are positive, so we obtain a bound $\epsilon \geq x_t^{2-\gamma} \Rightarrow x_t \leq \epsilon^{\frac{1}{2-\gamma}}$. We also find $\epsilon \geq \frac{l^2}{2x_t^2} \Rightarrow x_t \geq \sqrt{\frac{l^2}{2\epsilon}}$, which brackets the two turning points. We will order the two turning points as $x_1 < x_2$. As long as we are not matching I_r to $I_r^K = 0$[5], we can also find an intermediate bracketing point $x_1 < x_c < x_2$ by finding the circular orbit of this potential, which is located at $x_c = (l^2/(2-\gamma))^{\frac{1}{4-\gamma}}$. With the turning points at hand, we can calculate I_r numerically, given (ϵ, l, l_z). We will also use a bracketing algorithm to solve for the energy. Once more, as long as we are not matching to $I_r^K = 0$, we know that we will not be integrating over a circular orbit, and thus $\epsilon > \Phi(x_c)/\phi_0$. There is no analytical upper bound that can be obtained on the energy, but, if we consider the change of variables $E = \Phi(r)y$ in Eq. (4.6), we obtain

$$\rho(r) = f_0 \Phi(r)^{3/2-\beta} \int_1^\infty \mathrm{d}y\, y^{-\beta}\sqrt{y-1}. \tag{4.10}$$

In our applications, we will be considering a profile with $\gamma = 1$, and from Eq. (4.7), we see that $\beta = 5/2$. The exact value of the integral over y is 2/3, and integrating up to $y = 150$ allows us to obtain this integral to better than 1% accuracy. This means that we are allowed to truncate this distribution at $E \simeq 150\Phi(r)$. In terms of the variable ϵ, this is a truncation at $150\Phi(r)/\phi_0$, which is a small number since $\phi(r) \ll \phi_0$ for the distances $r \ll r_0$ that we will be considering. That said, the MC algorithm will sporadically select very loosely bound orbits, so we conservatively truncate the distribution at $\epsilon = 10$.

In Fig. (4.1), spike profiles generated from power laws with different slopes are compared with an NFW profile ($\gamma = 1$). All of these profiles are normalized to have a density of 0.3 GeV/cm^3 at a distance r_0 =8kpc. In order to provide a simple fitting function for the spike, we revisited the Schwarzschild background calculation using a general power law profile, and

---

[5] $I_r = 0$ corresponds to a circular orbit. If $I_r \neq 0$ then the potential must have two turning points and it will have an extremum between them.

obtained the following fitting function for the density

$$\rho(r) = \rho_R \left(\frac{2R_{\text{sp}}}{Gm}\right)^{\gamma_{\text{sp}}} \frac{(1-\mathcal{E}_{circ}(r))^{\gamma_{\text{sp}}}}{\left(1+\frac{4Gm}{r}\right)^{\beta_\gamma}}, \tag{4.11}$$

where $\mathcal{E}_{circ}(r)$ is the energy of a circular orbit at coordinate r, and ρ_R, R_{sp} are given by [1]. See Fig. (4.2) for a comparison between the fitting function and the Schwarzschild spike.

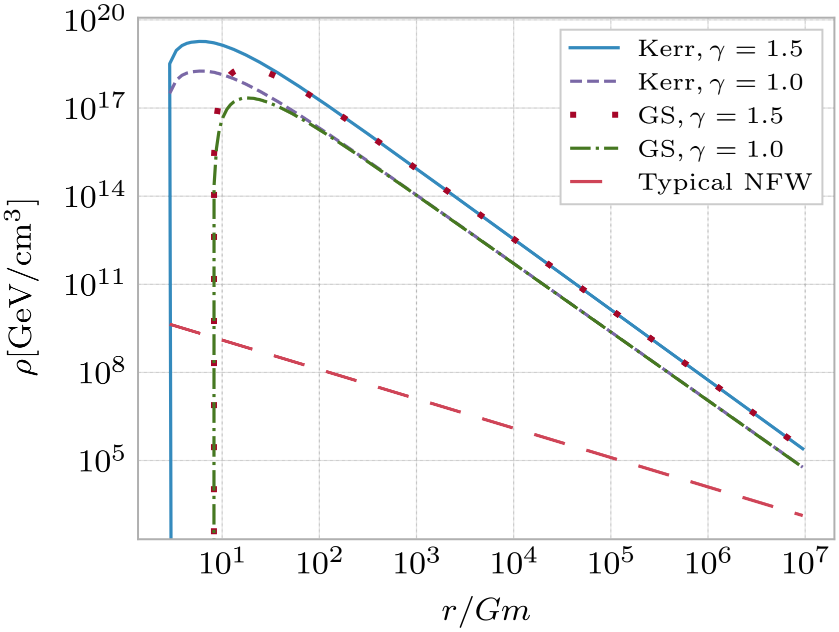

Fig. 4.1: A comparison of the density profiles generated from adiabatic matching to an outer profile with scale density 0.3 GeV/cm^3 and scale radius 8.0 kpc, but with a varying initial slope. Shown in the figure are the results of the classic Gondolo and Silk calculation (red dotted line and green dash-dotted line) and that of a calculation taking into account the effects of the Kerr metric (solid blue line and purple dashed line) with dimensionless spin parameter 0.7. We set the mass of the central black hole to be $4 \times 10^6 M_\odot$. To set the scale, an NFW profile with the same scale density and radius is shown (red, long dashes)

$$\rho_R = \rho_0 \left(\frac{r_0}{R_{\text{sp}}}\right)^{\gamma} \qquad R_{\text{sp}} = \alpha_\gamma r_0 \left(\frac{M}{\rho_0 r_0^3}\right)^{\frac{1}{3-\gamma}}. \tag{4.12}$$

The constant α_γ is given for a few values of the initial slope γ in [1]. The exponent β_γ varies slowly with γ and is displayed in Tab. (4.1). As we will show, provided that the correct density profile is used in Eq. (3.10), there is not a big difference between the full calculation that we perform here and one that simply uses the newtonian circular velocity to estimate $\langle\sigma v\rangle(r)$. It is therefore useful to have this expression for the density to estimate event rates using Eq. (3.10)[6], as it is just as easy to use as the fits provided by [1] but more accurate. This procedure is also computationally more efficient than doing the double phase space integration required in Eq. (2.20).

γ	0.05	0.2	0.4	0.8	1.0	1.2	1.4
β_γ	3.336	3.367	3.393	3.394	3.422	3.504	3.574

Tab. 4.1: Exponent β_γ in the fitting function of Eq. (4.12) as a function of the outer slope γ for a few values of γ.

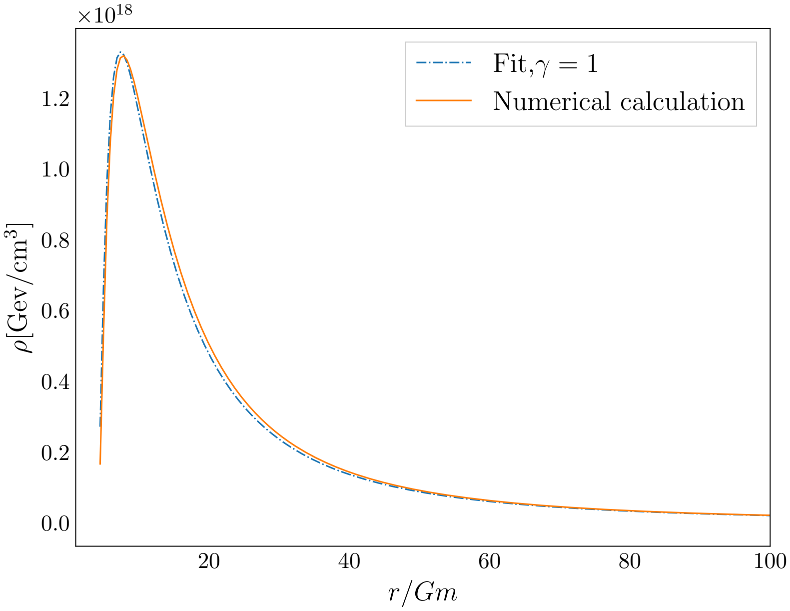

Fig. 4.2: A comparison for the density profile obtained numerically for $\gamma = 1$, with the same ρ_0, r_0 described in the text, and the proposed fitting function.

Having estabilished a method to efficiently calculate the adiabatic invariants, we may now calculate the event rate per unit volume within the spike using Eq. (2.20). We then use the axisymmetry of the final distribution and the fact that $\sqrt{-g} = (r^2 + a^2 \cos\theta)\sin\theta$ for

---

[6] With the understanding that $\langle\sigma v\rangle$ should now go inside the integral, as it is no longer a constant. We may also ignore the energy spectrum term.

the Kerr metric to calculate the total event rate within a halo as

$$\frac{\mathrm{d}N_{\text{spike}}}{\mathrm{d}t} = 2\pi \int \mathrm{d}(\cos\theta)\,\mathrm{d}r\,(r^2 + a^2\cos\theta)\frac{\mathrm{d}N}{\mathrm{d}^4x}(r, \cos\theta). \tag{4.13}$$

We perform the double integral by using a 2-dimensional Gauss-Legendre method. In Fig. (4.3) we show the impact of general relativistic effects on the event rate per unit volume from a given DM spike. Since the bulk of the event rate comes from contributions at small distances, it is seen that proper modeling of the spike is crucial. The PBHs considered here are assumed heavier than the average star, and dynamical friction from stellar encounters could make them sink to the center and provide another density enhancement, as considered in [86]. We will quantify these effects in Sec. (4.3).

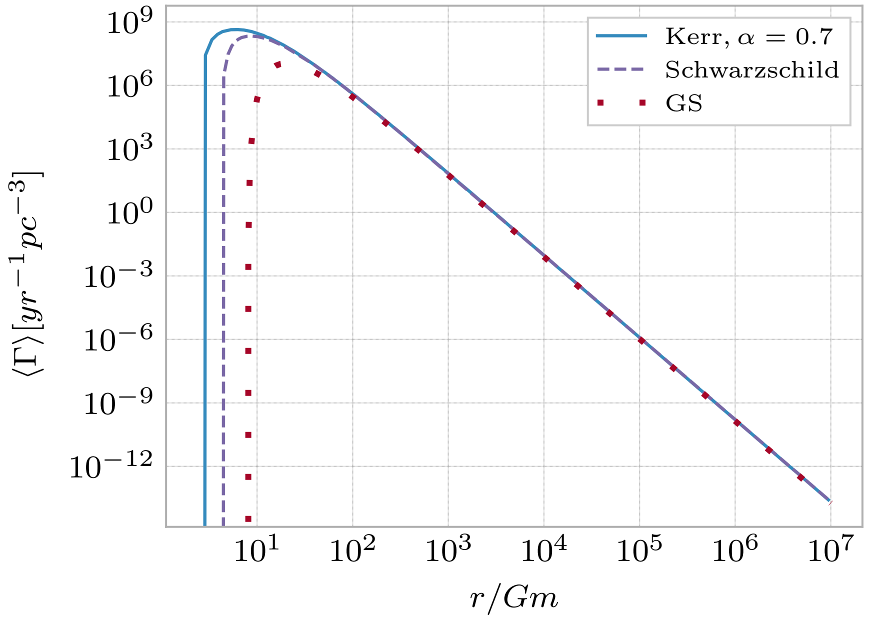

Fig. 4.3: Phase-space averaged event rate per unit spacetime volume for the spike matched to a $\gamma = 1.0$ outer profile, with $\rho_o = 0.3$ GeV/cm^3 and $r_0 = 8.0$ kpc. Results are shown for the equatorial plane of a Kerr background with dimensionless spin parameter 0.7 (blue,solid), a Schwarzschild background and the GS calculation (dotted,red). In all cases, the mass of the SMBH is $4 \times 10^6 M_\odot$. As discussed in the text, the impact mostly comes from the density enhancement instead of the velocity distribution.

In Tab. (4.2), we present event rates obtained for profiles with varying slopes and black hole masses. We do this by showing the ratio of our event rates to those obtained from a GS spike. It is seen that the effect of taking into account the full phase-spaced averaged cross section instead of simply inserting the newtonian circular velocity in Eq. (4.2) is small. The determination of SMBH spins is difficult [93], but spin parameters as high as 0.8 have been reported in the literature [94]. We therefore fix the spin parameter of the SMBH (which sets the background geometry) in our calculations to 0.7 to get an idea of the size of the boost to be expected while still being conservative.

Since most of the enhancement is already contained in going from the newtonian profile to the Schwarzschild background, we consider this a reasonable estimate for the boost factor. The scaling between the event rate obtained with a GS spike and that obtained from a Kerr spike is mass-independent. Therefore, one could adjust the LIGO event rates obtained in [90] by multiplying them with the corresponding factor in Tab. (4.2). However, as the authors of [89] point out, there is a dominant effect over this contribution to the merger rate of PBHs coming from binaries formed in the early universe that are merging today.

γ	GS(yr^{-1})	Sch,Circ	Sch,Full	Kerr,Circ	Kerr,Full
0.5	7.54×10^{-10}	1.80	1.95	1.89	2.05
1.0	3.73×10^{-8}	1.84	2.00	1.95	2.13
1.5	3.18×10^{-6}	1.84	2.00	1.96	2.15

Tab. 4.2: Total PBH merger rate for PBHs merging around the spike of a $4 \times 10^6 M_\odot$ SMBH, assuming that the spike is composed entirely of PBHs. The second column shows the result for a GS spike, and subsequent columns display the ratio of the event rate obtained for that calculation to the GS result. We pick a scale density of $0.3\mathrm{GeV/cm}^3$ and a scale radius of 8.0kpc. We show results for different background geometries and also show the effect of including the full phase space averaged cross section versus using the Newtonian circular velocity.

We therefore present these results as a mild strengthening of the work of Nishikawa et.al [90]. The analytical expression for the Schwarzschild spike also provides a simple way of taking into account general relativistic effects in the calculation of indirect detection observables, which, as shown here, can be significant.

The fact that most of the enhancement to the event rate of PBH mergers comes (for SMBHs with intermediate spin parameters) from the density enhancement rather than from a modification of the velocity distribution shows that the newtonian circular velocity, taken in [90] as the representative velocity for the calculation of the merger rate, is an appropriate choice and should not lead to considerable uncertainties. In the next section we will, however, point out some flaws in this approach.

4.3 PBH Mergers In The Local Universe: Orbital Decay and Dynamical Friction

We now turn to the analysis of two effects that can affect the spike profile close to the radius of influence of the SMBH: gravitational wave emission from the orbital motion of the PBHs around the SMBH, and dynamical friction from a nuclear star cluster (NSC) close to the SMBH. The emission of gravitational waves can be appropriately considered by focusing on the case of a PBH circling the SMBH. The characteristic time for an orbit at radial distance r to decay is [95]

$$T_{\mathrm{GW,SMBH}}(r) = \frac{5r}{256}\left(\frac{r}{Gm}\right)^2 \frac{r}{GM_{\mathrm{PBH}}} = 0.43\mathrm{yr} \times \left(\frac{m}{4\times 10^6 M_\odot}\right)\left(\frac{M_{\mathrm{PBH}}}{30 M_\odot}\right)^{-1}\left(\frac{r}{Gm}\right)^4. \quad (4.14)$$

We note that this timescale is exceedingly short compared to cosmological times on distance scales $r/Gm \lesssim 100$. This region, however, is where the spike is most concentrated and is the region responsible for most of the event rate considered in Sec. (4.2). Therefore, we may conclude that the signal originally considered in the previous section and in [90] is likely not present, as these PBHs would not make it to the present day to merge.

That said, dynamical friction from the stars on the outer region of the spike could still provide a mechanism for PBHs in that region to sink toward the SMBH, and this boosted spike could potentially lead to an enhanced merger rate around the SMBH. We will now attempt to quantify this effect but, before moving on, we will state some basic facts about dynamical friction.

Dynamical friction is the effect emerging from gravitational encounters of objects of mass M_{PBH} with a population of "field objects" of mass $m_* \ll M_{\mathrm{PBH}}$. When these objects exchange energy and momentum, the main effect on the more massive object is that it will lose energy, experiencing an effective drag force (see [31] for a derivation) in the direction of motion given by the Chandrasekhar formula

$$F_{DF} = -\frac{4\pi G^2 M_{\mathrm{PBH}}^2 \rho \log\Lambda}{v^2}\left[\mathrm{erf}(X) - \frac{2X}{\sqrt{\pi}}e^{-X^2}\right]. \tag{4.15}$$

In the above equation, ρ is the mass density of field objects, $X = v/\sqrt{2}\sigma$, σ their velocity dispersion, and $\log\Lambda$ is the *Coulomb logarithm*, a cutoff parameter to regulate the long-distance behavior of the gravitational interaction. The parameter Λ is typically estimated as $b_{\max}/b_{90}$, where $b_{\max}$ is a cutoff impact parameter (of order the size of the system), and b_{90} is the impact parameter leading to a 90° deflection of the relative velocity. Typical values for $\log\Lambda$ are between 5 and 10.

Several assumptions go into the derivation of this equation, the most important being that the velocity distribution of the system is Maxwellian and that the density ρ is constant everywhere in space. In spite of these very strong assumptions, numerical work shows that this approximation is able to capture the essential physics of dynamical friction in many situations. We will therefore assume the validity of the Chandrasekhar formula in the local density approximation, in which we replace $\rho, \sigma \to \rho(r), \sigma(r)$. This has been shown in the literature to be reliable to at least estimate the timescale in which an object might sink due to dynamical friction [96].

In order to move forward, we require a model for both of these quantites. The Milky Way's nuclear star cluster is well described by a broken power-law profile [2]. To do a calculation applicable to Milky-Way-like galaxies rather than just the Milky Way, we will follow the recipe in [97] and assume that the SMBH's sphere of influence contains a stellar mass of $2m$. We will also assume, following observations, that the inner slope of the stellar density is $\gamma_{\rm NSC} = 1$.

With this information in hand, we will assume that the PBHs move in circular orbits and that the effect of dynamical friction is to introduce a dragging torque, which will cause the PBHs to sink. We will therefore solve the differential equation

$$\frac{\mathrm{d}L}{\mathrm{d}t} = -F_{DF} r, \quad L = M_{\rm PBH} v r = M_{\rm PBH}\sqrt{Gmr}. \tag{4.16}$$

Furthermore, we will assume that, within the SMBH's radius of influence, the stellar velocity dispersion may be taken to be of order $\sqrt{Gm/r}$, since the SMBH should dominate the gravitational potential. This leads to the following differential equation for $r(t)$

$$\frac{\mathrm{d}r}{\mathrm{d}t} \equiv -v_{\rm DF}(r) = -\frac{8\pi M_{\rm PBH}}{m}\rho_{0*} r_{0*}^{5/2}\sqrt{\frac{G}{m}}\left(\frac{r_0}{r}\right)^{\gamma-5/2}\log\Lambda g(1), \tag{4.17}$$

with $g(X) = \mathrm{erf}(X) - 2X\pi^{-1/2}e^{-X^2}$. The parameters r_{0*}, ρ_{0*} are, respectively, the SMBH's radius of influence (where we are cutting off the stellar profile) and the stellar density at that position. This provides us with a local timescale $T_{\rm DF}(r) = r/v_{\rm DF}(r)$, which would be the time for a PBH to fall to the origin if it sank at constant speed. This does not happen and, in fact, the time to fall towards the origin diverges, as can be seen by solving Eq. (4.17), which gives $t(r_{\rm final}) \sim r_{\rm final}^{\gamma-3/2}$ for $r_{\rm final} \ll r(t=0)$. That said, we can take this as a timescale in which dynamical friction can efficiently act on the PBHs. We show these timescales on Fig. (4.4). In that figure, we also show an estimate of the timescale for merger events to occur. To estimate that timescale, $T_{\rm merge}$, we use the fact that the binary formation rate is $\rho\langle\sigma v\rangle/M_{\rm PBH}$, and we take as $\rho(r)$ the initial spike profile.

Let us put Fig. (4.4) in perspective: our guiding assumption is that the PBH spike was formed sometime early in galactic history, and may have lived for times as long as 10Gyr. If the spike has survived without significant modification, then $T_{\rm merge}(r)$ is the inverse of

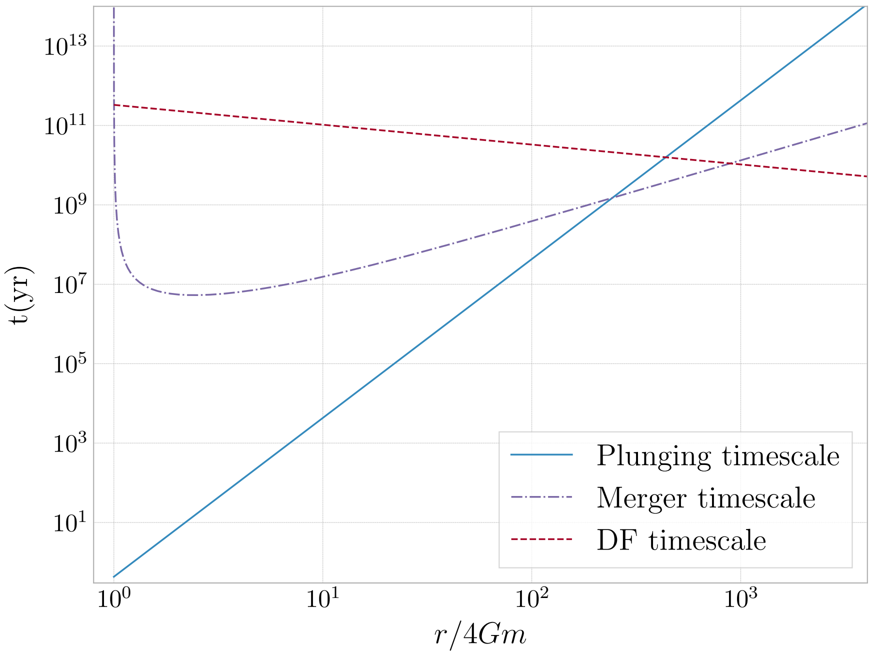

Fig. 4.4: The timescales for orbital decay from gravitational wave emission (solid line), binary formation (dot-dashed line) and the local dynamical friction timescale (dashed line)

.

the local binary formation rate in the spike. It can also be interpreted as the average time between binary formation events. We see that, if the spike is formed early on, it cannot be "pristine" after 10Gyr: not only is $T_{\mathrm{merge}} \ll 10$Gyr, but also $T_{\mathrm{GW,SMBH}} \ll 10$Gyr. This means that binary formation events *and* plunges into the SMBH would change the spike profile.

Unlike in the case of WIMP dark matter, however, PBHs that undergo mergers don't annihilate away: they turn into a larger BH. If we make the simple assumption that every merger turns two black holes of mass M_{PBH} into a single black hole of mass $2M_{\mathrm{PBH}}$, then the mass density is not changed by mergers. The cross section $\langle\sigma v\rangle \propto M_{\mathrm{PBH}}^2$, so this timescale would get shorter as black holes continue merging, but we will ignore this and just take T_{merge} as a typical timescale for a merger to occur. The fact that $T_{\mathrm{merge}} \ll 10$Gyr can then be taken to mean that the *mass spectrum* of PBHs within the spike could change significantly over

10Gyr.

Turning now to the timescale $T_{\rm DF}(r)$, that scale shows from which regions in the halo PBHs could sink significantly in 10Gyr. The sinking of these PBHs would cause the density to increase, lowering $T_{\rm merge}$ and making it so PBHs from the outer spike can now contribute significantly to the present merger rate.

We are now faced with the following issues: by how much does the spike profile contract, and does it produce an appreciable boost to the event rate? Furthermore, will the merging PBHs have the same mass $M_{\rm PBH}$ as the initial PBHs, or will that distribution have significantly changed? In estimating these effects, we note from Fig. (4.4) that dynamical friction is only relevant in the outer regions of the spike. We are thefore permitted to ignore the effects of spin, using Eq. (4.11) to model the initial spike profile.

To estimate the boost to the present merger rate, as well as to estimate how many PBHs would undergo at least one merger, we implement the following scheme: we solve the continuity equation with a source term, $\frac{\partial \rho/M_{\rm PBH}}{\partial t} = -\nabla\cdot\boldsymbol{j} - \frac{1}{2}\langle\sigma v\rangle\left(\frac{\rho}{M_{\rm PBH}}\right)^2$. We will take $\boldsymbol{j} = -v_{\rm DF}\hat{r}$ and, from our analysis in the previous section, we will calculate $\langle\sigma v\rangle(r)$ from Eq. (4.2) and using the newtonian circular velocity as $v(r)$, since we have verified that this is appropriate.

The idea behind this analysis is that, ignoring the merger rate term, the continuity equation provides us with the boost to the density due to the sinking of PBHs from the outer spike. Inclusion of the merger rate term will remove PBHs from the profile, and will provide us with an estimate of how many PBHs will merge at least once. If most PBHs merge, the fact that $T_{\rm merge}(r)$ is expected to decrease with repeated mergers would then allow us to conclude that we can expect the mass spectrum of the presently merging PBHs to have contributions from multiple masses.

Fortunately, with all of the approximations that we have introduced, the continuity equation can be solved analytically, and the solution is

$$\frac{1}{n(r,t)} = \frac{1}{n(r_i,0)}\left(\frac{r}{r_i}\right)^{\alpha+2} - \frac{\langle\sigma v\rangle_0 r}{2v_0}\frac{\left(\frac{r}{Gm}\right)^{\beta}\left(\frac{r}{r_{infl}}\right)^{\alpha}\left(1-\left(\frac{r_i}{r}\right)^{\beta-1-2\alpha}\right)}{(\beta-1-2\alpha)8\pi\frac{M_{PBH}}{m}\sqrt{\frac{M_{0*}}{m}}\log\Lambda g(1)}, \tag{4.18}$$

$$\tilde{v}_0 = \sqrt{\frac{GM_{0*}}{r_{0*}}},\ M_{0*} = \rho_{0*}r_{0*}^3.$$

In the above expression, $\beta = 11/14$ comes from the dependence of the GW capture cross section on the relative velocity of the two PBHs ($\sigma v \sim v^{-11/7}$ and $v \sim r^{-1/2}$). The parameter $\alpha = 5/2 - \gamma_{NSC}$ comes from $v_{DF}(r)$. The distance $r_i = r_i(r,t)$ corresponds to the radial coordinate that the PBH currently at coordinate r had at time $t = 0$. The factor $\langle\sigma v\rangle_0$ is a normalization factor for the capture cross section. In Fig. (4.5), we show the combined effect of mergers and dynamical friction on the density profile, as well as the effect of dynamical friction acting on the PBH system by itself.

With these profiles in hand, we can calculate the GW merger event rate from them using Eq. (3.10) and taking advantage of the spherical symmetry that we may assume of our system. For the density profiles in Fig. (4.5), we obtain merger rates of $6.65 \times 10^{-8}\text{yr}^{-1}$, $2.47 \times 10^{-5}\text{yr}^{-1}$ and $5.48 \times 10^{-7}\text{yr}^{-1}$ for the pure spike, DF only, and DF with mergers removed ("Continuity" in Fig. (4.5)), respectively. To put this in perspective, in [90] a merger rate of of $3.73 \times 10^{-8}\text{yr}^{-1}$ is obtained for the GS spike, so the effects of dynamical friction may be significant.

Although it may seem like the merger rate for the "Continuity" profile is the one to be expected as our estimate for the present PBH merger rate, it is important to remember that black holes that undergo a merger are not removed from the profile, they become a black hole of a different mass. Therefore, the DF only calculation could provide a reasonable estimate, since, due to the properties of the binary capture cross section, the integral in Eq. (3.10) for the pure spike is independent of M_{PBH}. The DF only result is roughly 650 times larger than that obtained by [90]. For the parameters that we considered, roughly 3/4 of all PBHs

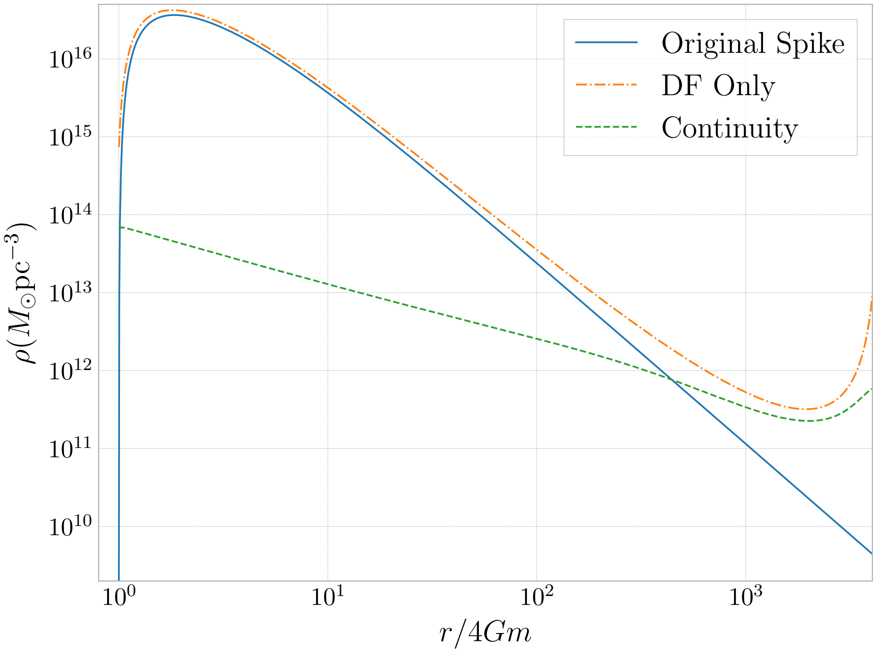

Fig. 4.5: The original spike profile (continuous line), the spike enhanced by dynamical friction (dot-dashed line), and the dynamical friction enhanced profile with merging PBHs removed (dashed). For both of these profiles, we assumed that dynamical friction acts on the PBHs for 10Gyr.

should participate in at least one merger event.

This "boost factor" that we have obtained should be calculated as a function of SMBH mass, since the total merger rate that an observatory like LIGO would see is the merger rate per SMBH folded in with the SMBH mass function. We finish this section by commenting on some of our expectations for these results. Ultimately, numerical simulations are required to solve this problem.

The starting point, which may be seen from Eq. (4.17), is that $T_{\mathrm{DF}} \propto m^{3/2}$. Thus, dynamical friction can act more efficiently in the NSCs around lighther SMBHs, leading to larger boosts. Moreover, cutting off the stellar distribution at r_{infl} is a simplification, and PBHs could fall from further distances in 10Gyr, as is seen explicitly in [97]. This requires a more detailed model of what the spike should be beyond r_{infl}, but here we will make the simplest possible assumptions.

It should be stressed that there is no reason to expect the simple analysis performed here, using the Chandrasekhar formula, to hold in systems around lighter SMBHs, as those will necessarily contain fewer stars and fewer PBHs. More importantly, the sensitivity of our results to $\log \Lambda$ implies that a detailed study is needed to properly understand the effects of dynamical friction on the merger rate.

We conclude by remarking that it would be important to check these calculations with numerical simulations, as they can provide a reliable value of the boost that dynamical friction can have to the merger rate around PBH spike and whether or not this could make it competitive with the rates obtained from binaries formed in the early universe [89]. Moreover, the broadening of the PBH mass function or other observationally interesting signatures could be explicitly obtained.

4.4 PBH Mergers In The Early Universe And Future Perspectives

As Eq. (4.1) shows, only very small, eccentric binaries can merge within a Hubble time. Binaries that form in our local universe are both [98], and therefore merge very quickly, within at most a few hundred thousand years [7]. The strong dependence on orbital parameters led to the proposal [99] that MACHOs formed in the early universe could merge within a Hubble time and be observed by gravitational wave detectors.

In fact, transposing the result in [99] to $30 M_\odot$ PBHs, a merger rate can be obtained (depending on the fraction of DM in PBHs) that is several orders of magnitude larger than that inferred by the LIGO collaboration [89]. However, due to their incredibly long lifetimes and the multitude of perturbations that act on them, it is not entirely obvious that such

---

[7] Eqs. (4.1, A.12) show that there should be a strong dependence on the merger timescale and the halo velocity dispersion. This upper limit of a few hundred thousand years comes from considering halos with virial masses of $10^6 M_\odot$ [32], which have a lower velocity dispersion than the Milky Way, leading to the longer lifetime

binaries can survive without being disrupted.

The physical picture that emerges from [89] is, however, surprisingly simple: given a random distribution of PBHs, those that are tightly bound at early times (prior to matter-radiation equality) can form stable binaries with a distribution of eccentricities. It is this property of being tightly bound at such early times that gives these binaries their stability: being such a strong density perturbation, they are stable against tidal torques from other objects.

That said, there are significant uncertainties in the analytical estimates performed in the literature, particularly on three fronts: N-body effects [100] in the formation of the first PBH halos, dynamical friction from a potential WIMP halo surrounding the PBH binary [101], and baryon accretion [102]. Most of the follow-ups to [89] seem to at least agree on the fact that the merger rate obtained from binaries formed in the early universe is still high enough to exclude PBHs as forming all of the dark matter, if a narrow PBH mass spectrum is assumed. With regards to these uncertainties, baryon accretion could potentially have the most impact in the disruption of the binary, but dedicated simulations are still required.

Another issue with the calculation in [89] is the probability distribution that is assumed for the binary separation: namely, it is taken to be a Poisson process with one binary on average per volume $V = M_{\mathrm{PBH}}/\rho_M$. This is the simplest possible assumption for their distribution, although there is significant discussion as to whether or not PBH clustering could occur [103, 104, 105]. However, it is agreed upon that the distribution of PBHs could only be *more* clustered than the naive Poisson distribution and this strengthens the constraints that can be imposed from the LIGO merger rate. Overall, the limits on the PBH fraction obtained from [89], though potentially too restrictive, seem to be robust.

We finish this chapter by proposing a new, yet unexplored (and undeveloped) way that simulations taking PBH DM seriously could probe their abundance. The idea is as follows: it is observed that roughly half of all stars are part of binary systems [31], and simulations show that three-body encounters between a binary of low mass stars and a more massive black hole can rapidly lead to *exchange encounters* where one of the stars in the binary is replaced by the black hole (see, e.g [106]). In high density environments like galactic nuclei and globular clusters, such three-body encounters are frequent enough to, in principle, turn an isolated population of PBHs into black hole-stellar binaries and, potentially, to take this process a step further and form more PBH binaries.

To estimate this effect, we consider the three-body exchange cross-section to scale as $\Sigma \sim \frac{G(M_{\rm PBH}+2M_{\rm star})a}{V^2}$ [107]. If we take as our environment the NSC in the Milky Way, Fig. (4.6), based on the observations of [2] shows how, even for a conservative fraction of binary systems (10%), the stellar binary density is much larger than the local DM density. We will therefore take the stellar density to be unperturbed by the relatively few exchanges with PBHs. A simple estimate of the rate at which stars will be ejected from such systems is then simply $\Gamma = n_{\rm star}\Sigma V$, and we take $V \sim 30$km/s as an estimate of the local velocity

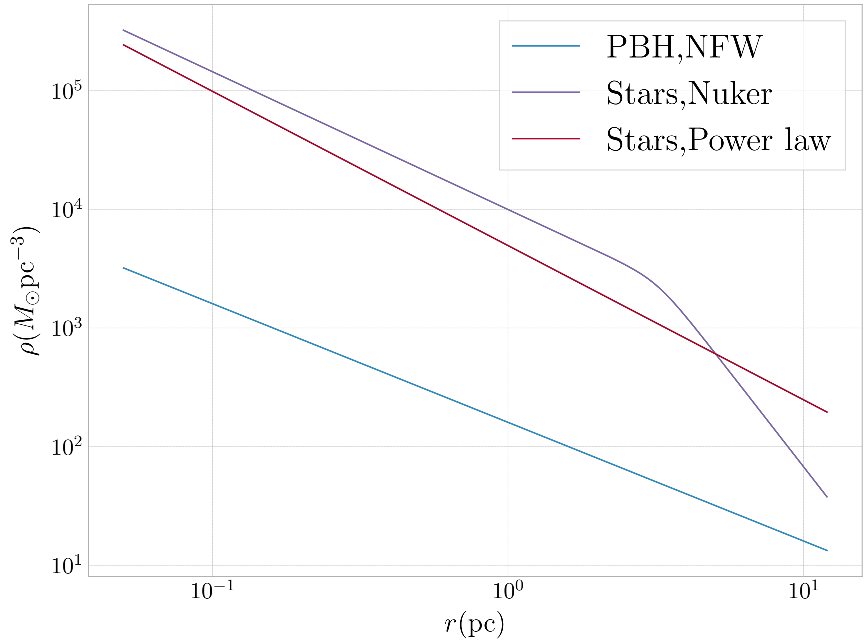

Fig. 4.6: Mass density of stellar binaries and PBHs, with the assumption $f_{\rm binary} = 0.1$. The "Nuker profile" is the functional form used in [2] to fit the observed stellar density in the Milky Way's NSC.

dispersion in the NSC [38]. Thus, the timescale for an exchange interaction to occur would be on the order of

$$\begin{aligned} t_{\rm ex} &\sim \frac{2m_{\rm star}V}{f_{\rm binary}\rho_{\rm star}G(M_{\rm PBH}+2m_{\rm star})a} \\ &\simeq (1{\rm Gyr})\left(\frac{f_{\rm binary}}{0.1}\right)^{-1}\left(\frac{m_{\rm star}}{M_\odot}\right)\left(\frac{V}{30{\rm km/s}}\right)\left(\frac{\rho_{\rm star}}{10^5M_\odot{\rm pc}^{-3}}\right)^{-1}\left(\frac{a}{10AU}\right)^{-1}\left(\frac{M_{\rm PBH}}{30M_\odot}\right)^{-1}. \end{aligned} \tag{4.19}$$

Although the stellar density in the NSC drops off rapidly from the reference value we took in Eq. (4.19), the smaller densities at larger distances could potentially allow wider binaries to be present. For instance, taking as a criterion for the maximum binary radii allowed as a function of r that tidal forces in the local (PBH + NSC + SMBH) gravitational field be weaker than the internal attraction of the binary, separations of up to 2000AU are permitted, which could potentially compensate the drop in density and keep the exchange timescale at around 1Gyr.

Due to the complexities involved and the high densities in the NSC, the study of these systems should be made through simulations, which could potentially reveal interesting constraints on the PBH fraction. This is because, if we assume a constant exchange rate between PBHs and stars, the total number of binary systems formed should naively scale linearly with the DM fraction in PBHs, as the total exchange rate per unit volume should simply be $n_{\rm PBH}/t_{\rm ex}$ [8]. Such considerations could also potentially allow for cross-checks of models of a PBH population to be performed by comparing local populations of X-ray binaries (which would be formed in one step of the exchange processes) with local populations of BH binaries inferred from mergers, once a sufficient number of these have been observed.

---

[8] This is important because other constraints scale with higher powers of the PBH fraction f and are potentially less constraining at low f

Chapter 5

Conclusions

The nature of the dark matter and dark energy present in the standard cosmology are important unsolved problems in physics. Although we have detected their gravitational effects, nothing is known about how these components of our universe interact with visible matter. Models have been proposed and parameter space has been carved out, but the simplest models, such as WIMPs, have yet to be effectively ruled out.

A competing alternative to the inclusion of dark matter in the standard cosmology is modified gravity, in which it is assumed that GR must be modified. To describe data such as galactic rotation curves, phenomenological models like Modified Newtonian Dynamics (MOND) introduce a small acceleration scale (in $c = 1$ units, acceleration has dimensions of inverse length) in which the newtonian potential must be modified. It is possible to write down lagrangians (i.e, "complete theories") that reproduce the phenomenological newtonian potential proposed in MOND, but as of yet, there is no corresponding alternative "concordance model" that is able to explain all of the available observations in the way the standard cosmology can. Should such a model emerge, a critical future issue will be to determine how to discriminate between such disparate competing models. Modifying gravity, however, is not the subject of this work.

In this work, we have chosen to follow the mainstream and look for an avenue in which dark matter could be detected in an astrophysical context. As mentioned in Chapter 1, SMBHs exist at the center of most galaxies, and those that are less massive, in systems that might have not undergone major mergers, it is possible that they grow adiabatically from a small seed. Under this assumption, the surrounding DM density increases substantially, and this has a substantial impact on indirect detection observables.

Chapter 2 describes how to use a phase space distribution to describe a relativistic system, and how to extract observable quantities. We use a framework in which covariant and invariant quantites (vectors and scalars) are calculated before converting them into observer-dependent quantities. This procedure has the advantage of making the observer or coordinate dependence of a given calculation simple to take into account. We finish by generalizing a proof of the adiabatic invariance of the phase space distribution function to particle motion around a Kerr metric.

With the setup of Chapter 2, Chapter 3 mostly focuses on the calculation of the adiabatic spike generated by an initial DM distribution that is a Hernquist profile. We chose that profile because it has the same slope as the NFW profile but has a phase space distribution that can be calculated analytically. Since the inner spike profile should only depend on the slope of the density profile and some normalization, this is appropriate. We then proceed to calculate the impact of SMBH spin on the particle fluxes coming from a spike, finding a moderate increase over the Schwarzschild case. The spike profile from WIMPs is expected to be cutoff by DM annihilations, which washes out the effects of spin, but spikes might still be present around IMBHs at the centers of dwarf galaxies, should they exist.

Chapter 4 deals with the possibility of DM not being a standard WIMP, but instead primordial black holes. Such PBHs would be non-relativistic throughout cosmic history and could cluster in an adiabatic spike. In this case, the equivalent process to WIMP annihilation is binary BH merger, and instead of producing particles, it generates gravitational waves. However, due to the short merger timescales of bound PBH binaries, the mathematical description of this process is similar and a gravitational wave flux can be extracted using the same formalism developed in Chapter 2. However, emission of gravitational waves from the PBH orbit around the SMBH is shown to effectively destroy the spike, although dynamical friction from a surrounding NSC could generate a significant amount of PBH mergers. Furthermore, binaries formed in the early universe could provide a more constraining channel on the PBH abundance. That said, adiabatic spikes replenished by dynamical friction could become an interesting channel to observe the extreme mass ratio inspiral of a PBH into an SMBH with a space-based gravitational wave observatory like LISA.

APPENDICES

Appendix A

The Black Hole Binary Formation Cross Section

In this appendix, we will present a derivation of Eq. (4.2), the cross section for the formation of a PBH binary from the emission of gravitational waves. The main idea of this calculation [92] is that the pair of black holes is sufficiently separated and slowly moving so that the gravitational wave emission can be taken care of in the context of perturbation theory. Typical velocities of galactic objects are small compared to that of light [31], so the second part of the approximation is certainly guaranteed. We will show that the first part of the approximation is also reasonable in the derivation of the cross-section.

In the context of these approximations, capture happens when the kinetic energy of the black hole pair is dissipated by gravitational waves. Since we will be using the quadrupole formula from perturbation theory [15], it will therefore be permissible to ignore the contribution of the kinetic energy of the pair to the "zeroth-order" orbit, as it will be of the same order of the perturbative effect of gravitational wave emission. This implies that we can calculate the emission of gravitational waves by the pair assuming that their relative coordinate describes a newtonian parabolic orbit.

Since the orbit we are considering is planar, we will use cylindrical coordinates (r, θ, z)

and set $z = 0$. The emitted power is given in terms of the traceless quadrupole tensor:

$$P = -\frac{G}{5}\frac{\mathrm{d}^3 J_{ij}}{\mathrm{d}t^3}\frac{\mathrm{d}^3 J^{ij}}{\mathrm{d}t^3}, \tag{A.1}$$

$$J_{ij} = \mu\left(x_i x_j - \frac{1}{3}r^2\delta_{ij}\right), \tag{A.2}$$

where μ is the reduced mass of the system. We denote the mass of each particle in the system as m_1, m_2. This is a three-dimensional tensor in flat space, so the metric to be used here is simply δ_{ij}. We will begin by considering general masses (m_1, m_2) and only set $m_1 = m_2$ at the end of the calculation for the cross-section. In terms of the polar coordinates (r, θ), we have

$$J_{ij} = \frac{\mu r^2}{3}\begin{pmatrix} 3\cos^2\theta - 1 & 3\cos\theta\sin\theta & 0 \\ 3\cos\theta\sin\theta & 3\sin^2\theta - 1 & 0 \\ 0 & 0 & -1 \end{pmatrix}. \tag{A.3}$$

The parabolic orbit is described in polar coordinates as

$$r(\theta) = \frac{2r_p}{1+\cos\theta}, \tag{A.4}$$

where r_p is the distance of closest approach, taken to be at $\theta = 0$. The newtonian parabolic orbit has zero total energy, so using that information along with conservation of angular momentum gives

$$\dot{\theta} = \frac{l}{4\mu r_p^2}(1+\cos\theta)^2 \tag{A.5}$$

$$l^2 = 2Gm_1m_2\mu r_p, \tag{A.6}$$

l being the relative angular momentum of the system. Inserting Eqs.(A.4, A.5) in Eq.(A.1), we find

$$\begin{aligned}\frac{\mathrm{d}E}{\mathrm{d}t} &= -\frac{G^4\mu^2(m_1+m_2)^3}{60r_p^5}(1+\cos\theta)^5(13+11\cos\theta),\\ \frac{\mathrm{d}E}{\mathrm{d}\theta} &= -\frac{\sqrt{2(m_1+m_2)}G^{7/2}(m_1m_2)^2}{30r_p^{7/2}}(1+\cos\theta)^3(13+11\cos\theta).\end{aligned} \tag{A.7}$$

Integrating from $-\pi$ to π gives the energy loss from emission

$$\Delta E = -\frac{85\pi}{12\sqrt{2}}\frac{G^{7/2}(m_1m_2)^2(m_1+m_2)^{1/2}}{r_p^{7/2}}. \tag{A.8}$$

The capture criterion $|\Delta E| \geq \frac{1}{2}\mu v^2$ gives us a maximum value $r_{p,\max} = R_p$ equal to

$$R_p = \left(\frac{85\pi\sqrt{2}G^{7/2}m_1m_2(m_1+m_2)^{3/2}}{12v^2}\right)^{2/7}. \tag{A.9}$$

The naive cross section would then be given by $\sigma = \pi R_p^2$, but we need to take into account the gravitational focusing effect from the Coulomb potential: certain hyperbolic orbits that have an impact parameter $b > R_p$ will be focused to have a distance of closest approach $r_p < R_p$. The actual cross-section is then given by πB^2, where B is the value of the impact parameter such that the distance of closest approach is R_p. This can be straightforwardly obtained from conservation of energy and angular momentum:

$$\begin{aligned} l = \mu v B = \mu v_p R_p &\Rightarrow v_p = v\frac{B}{R_p},\\ \frac{1}{2}v^2 = \frac{1}{2}v_p^2 - G\frac{m_1+m_2}{R_p} &\Rightarrow v^2 = v^2\frac{B^2}{R_p^2} - \frac{2G(m_1+m_2)}{R_P}\\ &\Rightarrow B^2 = R_p^2\left(1+\frac{2G(m_1+m_2)}{v^2R_p}\right).\end{aligned} \tag{A.10}$$

The approximation of slow moving masses means that we can ignore the 1 in comparison with the second term in the previous equation, obtaining, finally,

$$\sigma = 1.37 \times 10^{-14} \left(\frac{M_{\rm PBH}}{30 M_\odot}\right)^2 \left(\frac{v_{\rm rel}}{200 {\rm km/s}}\right)^{-18/7} {\rm pc}^2. \tag{A.11}$$

If we expect our PBHs to have a mass of $30M_\odot$, then we can write

$$R_p = 10^4 {\rm km} \left(\frac{\mu}{15 M \odot}\right)^{2/7} \left(\frac{M_{\rm PBH}}{30 M_\odot}\right)^{5/7} \left(\frac{v}{200 {\rm km\, s^{-1}}}\right)^{-4/7}. \tag{A.12}$$

The event horizon size for a $30M_\odot$ spherical PBH is 45km, so we see that capture does indeed happen at a distance where the effects of general relativity are unimportant. This 10^4km capture separation implied by the previous equation is also roughly 600 times smaller than the event horizon size of a $4 \times 10^6 M_\odot$ SMBH, which means that tidal effects from a central SMBH can also be reasonably be ignored in the Milky-Way-type galaxy considered in the main text[9]. For smaller BHs, such as the IMBH that might be present at the centers of dwarf galaxies [108], tidal effects could be important for the most deeply bound BHs.

We may also use the quadrupole formula to derive Eq. (4.14). In this case, we may simply plug in $\theta = \omega t$ for a circular orbit, with $\omega^2 = G(m_1 + m_2) r^{-3}$. If we then assume that GW emission has the relative coordinate go from one circular orbit to the next[10], we may say that $P = \dot{E}$, and E can be taken as the energy of a circular orbit, $-\frac{1}{2} G(m_1 + m_2)\mu r^{-1}$. Evaluating the quadrupole formula and solving for $\dot{r}$ then gives

$$\frac{{\rm d}r}{{\rm d}t} = -\frac{64}{5} \frac{G(m_1 + m_2)^2 \mu}{r^3}. \tag{A.13}$$

Assuming that $m_1 \gg m_2$, then $m_1 + m_2 \simeq m_1$, $\mu \simeq m_2$. We can now integrate Eq. (A.13) to find the time $T_{\rm GW,SMBH}$ for a circular of initial radius r to decay, which gives Eq. (4.14).

---

[9] That said, the presence of the SMBH can induce a three-body effect known as a Lidov-Kozai resonance, which can make PBH relative orbits very eccentric. We will ignore this.

[10] A detailed analysis of angular momentum losses from gravitational waves shows that their emission tends to circularize orbits. It is therefore fair to assume that no eccentricity will be added in the secular evolution of the orbital parameters.

Bibliography

[1] Paolo Gondolo and Joseph Silk. Dark matter annihilation at the galactic center. *Phys. Rev. Lett.*, 83:1719–1722, 1999.

[2] R. Schödel, E. Gallego-Cano, H. Dong, F. Nogueras-Lara, A. T. Gallego-Calvente, P. Amaro-Seoane, and H. Baumgardt. The distribution of stars around the Milky Way's central black hole. II. Diffuse light from sub-giants and dwarfs. A&A, 609:A27, January 2018.

[3] Gianfranco Bertone and Dan Hooper. A History of Dark Matter. *Submitted to: Rev. Mod. Phys.*, 2016.

[4] A. V. Zasov, A. S. Saburova, A. V. Khoperskov, and S. A. Khoperskov. Dark matter in galaxies. *Phys. Usp.*, 60(1):3–39, 2017.

[5] Igor Tkachev. Cosmology and Dark Matter. In *Proceedings, 2016 European School of High-Energy Physics (ESHEP2016): Skeikampen, Norway, June 15-28 2016*, volume 5, pages 259–294, 2017.

[6] Katherine Freese. Status of Dark Matter in the Universe. *Int. J. Mod. Phys.*, 1(06):325–355, 2017.

[7] F. Zwicky. Die Rotverschiebung von extragalaktischen Nebeln. *Helvetica Physica Acta*, 6:110–127, 1933.

[8] S. Weinberg. *Cosmology*. Cosmology. OUP Oxford, 2008.

[9] Vera C. Rubin, W. Kent Ford, Jr., and Norbert Thonnard. Extended rotation curves of high-luminosity spiral galaxies. IV. Systematic dynamical properties, Sa through Sc. *Astrophys. J.*, 225:L107–L111, 1978.

[10] Fabio Iocco, Miguel Pato, and Gianfranco Bertone. Evidence for dark matter in the inner Milky Way. *Nature Phys.*, 11:245–248, 2015.

[11] F. Lelli, S. S. McGaugh, and J. M. Schombert. SPARC: Mass Models for 175 Disk Galaxies with Spitzer Photometry and Accurate Rotation Curves. AJ, 152:157, December 2016.

[12] Julio F. Navarro, Carlos S. Frenk, and Simon D. M. White. The Structure of cold dark matter halos. *Astrophys. J.*, 462:563–575, 1996.

[13] Biswajit Pandey and Suman Sarkar. Testing homogeneity in the Sloan Digital Sky Survey Data Release Twelve with Shannon entropy. *Mon. Not. Roy. Astron. Soc.*, 454(3):2647–2656, 2015.

[14] Kelvin K. S. Wu, Ofer Lahav, and Martin J. Rees. The large-scale smoothness of the Universe. *Nature*, 397:225–230, 1999. [,19(1998)].

[15] Sean M. Carroll. *Spacetime and geometry: An introduction to general relativity.* Addison-Wesley, San Francisco, CA, 2004.

[16] Edward W. Kolb and Michael S. Turner. The Early Universe. *Front. Phys.*, 69:1–547, 1990.

[17] N. Aghanim et al. Planck 2018 results. VI. Cosmological parameters. 2018.

[18] Paul Bode, Jeremiah P. Ostriker, and Neil Turok. Halo formation in warm dark matter models. *Astrophys. J.*, 556:93–107, 2001.

[19] J. Bernstein. *Kinetic Theory in the Expanding Universe.* Cambridge University Press, Cambridge, U.K., 1988.

[20] Celine Boehm and Richard Schaeffer. Constraints on dark matter interactions from structure formation: Damping lengths. *Astron. Astrophys.*, 438:419–442, 2005.

[21] Gianfranco Bertone, Dan Hooper, and Joseph Silk. Particle dark matter: Evidence, candidates and constraints. *Phys. Rept.*, 405:279–390, 2005.

[22] H. Baer and X. Tata. *Weak scale supersymmetry: From superfields to scattering events.* Cambridge University Press, 2006.

[23] Rudolf Haag, Jan T. Lopuszanski, and Martin Sohnius. All Possible Generators of Supersymmetries of the S-Matrix. *Nucl. Phys.*, B88:257, 1975. [,257(1974)].

[24] Mark Srednicki. *Quantum Field Theory.* Cambridge Univ. Press, Cambridge, 2007.

[25] Stephen P. Martin. A Supersymmetry primer. pages 1–98, 1997. [Adv. Ser. Direct. High Energy Phys.18,1(1998)].

[26] Marcin Badziak, Marek Olechowski, and Stefan Pokorski. New Regions in the NMSSM with a 125 GeV Higgs. *JHEP*, 06:043, 2013.

[27] Bernard J. Carr and S. W. Hawking. Black holes in the early Universe. *Mon. Not. Roy. Astron. Soc.*, 168:399–415, 1974.

[28] Francesc Ferrer, Eduard Masso, Giuliano Panico, Oriol Pujolas, and Fabrizio Rompineve. Primordial Black Holes from the QCD axion. *Phys. Rev. Lett.*, 122:101301, 2018.

[29] T. Padmanabhan. *Structure Formation in the Universe.* Cambridge Univ. Press, Cambridge, UK, 1993.

[30] Sébastien Clesse and Juan García-Bellido. Massive Primordial Black Holes from Hybrid Inflation as Dark Matter and the seeds of Galaxies. *Phys. Rev.*, D92(2):023524, 2015.

[31] J. Binney and S. Tremaine. *Galactic Dynamics: Second Edition*. Princeton University Press, 2008.

[32] Simeon Bird, Ilias Cholis, Julian B. Muñoz, Yacine Ali-Haïmoud, Marc Kamionkowski, Ely D. Kovetz, Alvise Raccanelli, and Adam G. Riess. Did LIGO detect dark matter? *Phys. Rev. Lett.*, 116(20):201301, 2016.

[33] Bernard Carr and Joseph Silk. Primordial Black Holes as Generators of Cosmic Structures. *Mon. Not. Roy. Astron. Soc.*, 478(3):3756–3775, 2018.

[34] Masahiro Kawasaki, Ken'ichi Saikawa, and Toyokazu Sekiguchi. Axion dark matter from topological defects. *Phys. Rev.*, D91(6):065014, 2015.

[35] Davide Cadamuro. *Cosmological limits on axions and axion-like particles*. PhD thesis, Munich U., 2012.

[36] John Kormendy and Luis C. Ho. Coevolution (Or Not) of Supermassive Black Holes and Host Galaxies. *Ann. Rev. Astron. Astrophys.*, 51:511–653, 2013.

[37] D. Lynden-Bell. Gravity power. Phys. Scr, 17:185–191, March 1978.

[38] Reinhard Genzel, Frank Eisenhauer, and Stefan Gillessen. The Galactic Center Massive Black Hole and Nuclear Star Cluster. *Rev. Mod. Phys.*, 82:3121–3195, 2010.

[39] W. L. W. Sargent, P. J. Young, A. Boksenberg, K. Shortridge, C. R. Lynds, and F. D. A. Hartwick. Dynamical evidence for a central mass concentration in the galaxy M87. ApJ, 221:731–744, May 1978.

[40] K. Gebhardt, D. Richstone, S. Tremaine, T. R. Lauer, R. Bender, G. Bower, A. Dressler, S. M. Faber, A. V. Filippenko, R. Green, C. Grillmair, L. C. Ho, J. Kormendy, J. Magorrian, and J. Pinkney. Axisymmetric Dynamical Models of the Central Regions of Galaxies. ApJ, 583:92–115, January 2003.

[41] Yue Shen. The Mass of Quasars. *Bull. Astron. Soc. India*, 41:61, 2013.

[42] Laura Ferrarese and David Merritt. A Fundamental relation between supermassive black holes and their host galaxies. *Astrophys. J.*, 539:L9, 2000.

[43] Piero Ullio, HongSheng Zhao, and Marc Kamionkowski. A Dark matter spike at the galactic center? *Phys. Rev.*, D64:043504, 2001.

[44] P. J. E. Peebles. Gravitational collapse and related phenomena from an empirical point of view, or, black holes are where you find them. *General Relativity and Gravitation*, 3:63–82, June 1972.

[45] P. Young. Numerical models of star clusters with a central black hole. I - Adiabatic models. ApJ, 242:1232–1237, December 1980.

[46] H. Zhao. Analytical models for galactic nuclei. MNRAS, 278:488–496, January 1996.

[47] Gerald D. Quinlan, Lars Hernquist, and Steinn Sigurdsson. Models of Galaxies with Central Black Holes: Adiabatic Growth in Spherical Galaxies. *Astrophys. J.*, 440:554–564, 1995.

[48] Francesc Ferrer, Augusto Medeiros da Rosa, and Clifford M. Will. Dark matter spikes in the vicinity of Kerr black holes. *Phys. Rev.*, D96(8):083014, 2017.

[49] David Merritt, Milos Milosavljevic, Licia Verde, and Raul Jimenez. Dark matter spikes and annihilation radiation from the galactic center. *Phys. Rev. Lett.*, 88:191301, 2002.

[50] Gianfranco Bertone and David Merritt. Time-dependent models for dark matter at the Galactic Center. *Phys. Rev.*, D72:103502, 2005.

[51] Brian D. Fields, Stuart L. Shapiro, and Jessie Shelton. Galactic Center Gamma-Ray Excess from Dark Matter Annihilation: Is There A Black Hole Spike? *Phys. Rev. Lett.*, 113:151302, 2014.

[52] Laleh Sadeghian, Francesc Ferrer, and Clifford M. Will. Dark matter distributions around massive black holes: A general relativistic analysis. *Phys. Rev.*, D88(6):063522, 2013.

[53] F. Debbasch and W. A. van Leeuwen. General relativistic Boltzmann equation, II: Manifestly covariant treatment. *Physica A Statistical Mechanics and its Applications*, 388:1818–1834, May 2009.

[54] E. D. Fackerell. Relativistic Stellar Dynamics. ApJ, 153:643, August 1968.

[55] Brandon Carter. Global structure of the Kerr family of gravitational fields. *Phys. Rev.*, 174:1559–1571, 1968.

[56] T. A. Weaver. Reaction rates in a relativistic plasma. Phys. Rev. A, 13:1563–1569, April 1976.

[57] Michael E. Peskin and Daniel V. Schroeder. *An Introduction to quantum field theory.* Addison-Wesley, Reading, USA, 1995.

[58] Steven Weinberg. *The Quantum theory of fields. Vol. 1: Foundations.* Cambridge University Press, 2005.

[59] Barrett O'Neill. *The geometry of Kerr black holes.* Courier Corporation, 2014.

[60] Kip S. Thorne. Disk accretion onto a black hole. 2. Evolution of the hole. *Astrophys. J.*, 191:507–520, 1974.

[61] James M. Bardeen, William H. Press, and Saul A Teukolsky. Rotating black holes: Locally nonrotating frames, energy extraction, and scalar synchrotron radiation. *Astrophys. J.*, 178:347, 1972.

[62] Robert M Wald. *General relativity.* Chicago Univ. Press, Chicago, IL, 1984.

[63] T. Hahn. CUBA: A Library for multidimensional numerical integration. *Comput. Phys. Commun.*, 168:78–95, 2005.

[64] H. Goldstein, C.P. Poole, and J.L. Safko. *Classical Mechanics.* Addison Wesley, 2002.

[65] Eric Poisson. *A Relativist's Toolkit: The Mathematics of Black-Hole Mechanics.* Cambridge University Press, 2004.

[66] Ulrich Ellwanger, Cyril Hugonie, and Ana M. Teixeira. The Next-to-Minimal Supersymmetric Standard Model. *Phys. Rept.*, 496:1–77, 2010.

[67] Jyotiranjan Beuria, Utpal Chattopadhyay, AseshKrishna Datta, and Abhishek Dey. Exploring viable vacua of the Z_3-symmetric NMSSM. *JHEP*, 04:024, 2017.

[68] Werner Porod. SPheno, a program for calculating supersymmetric spectra, SUSY particle decays and SUSY particle production at e+ e- colliders. *Comput. Phys. Commun.*, 153:275–315, 2003.

[69] W. Porod and F. Staub. SPheno 3.1: Extensions including flavour, CP-phases and models beyond the MSSM. *Comput. Phys. Commun.*, 183:2458–2469, 2012.

[70] T.L. Lee, T.Y. Li, and C.H. Tsai. Hom4ps-2.0: a software package for solving polynomial systems by the polyhedral homotopy continuation method. *Computing*, 83(2-3):109–133, 2008.

[71] Ulrich Ellwanger, John F. Gunion, and Cyril Hugonie. NMHDECAY: A Fortran code for the Higgs masses, couplings and decay widths in the NMSSM. *JHEP*, 02:066, 2005.

[72] Philip Bechtle, Oliver Brein, Sven Heinemeyer, Georg Weiglein, and Karina E. Williams. HiggsBounds: Confronting Arbitrary Higgs Sectors with Exclusion Bounds from LEP and the Tevatron. *Comput. Phys. Commun.*, 181:138–167, 2010.

[73] Philip Bechtle, Oliver Brein, Sven Heinemeyer, Georg Weiglein, and Karina E. Williams. HiggsBounds 2.0.0: Confronting Neutral and Charged Higgs Sector Predictions with Exclusion Bounds from LEP and the Tevatron. *Comput. Phys. Commun.*, 182:2605–2631, 2011.

[74] Philip Bechtle, Oliver Brein, Sven Heinemeyer, Oscar Stal, Tim Stefaniak, Georg Weiglein, and Karina E. Williams. HiggsBounds $-$ 4: Improved Tests of Extended Higgs Sectors against Exclusion Bounds from LEP, the Tevatron and the LHC. *Eur. Phys. J.*, C74(3):2693, 2014.

[75] Philip Bechtle, Sven Heinemeyer, Oscar Stal, Tim Stefaniak, and Georg Weiglein. Applying Exclusion Likelihoods from LHC Searches to Extended Higgs Sectors. 2015.

[76] J. E. Camargo-Molina, B. O'Leary, W. Porod, and F. Staub. **Vevacious**: A Tool For Finding The Global Minima Of One-Loop Effective Potentials With Many Scalars. *Eur. Phys. J.*, C73(10):2588, 2013.

[77] Stefano Profumo, William Shepherd, and Tim Tait. Pitfalls of dark matter crossing symmetries. *Phys. Rev.*, D88(5):056018, 2013.

[78] Lisa Goodenough and Dan Hooper. Possible Evidence For Dark Matter Annihilation In The Inner Milky Way From The Fermi Gamma Ray Space Telescope. 2009.

[79] Kevork N. Abazajian. The Consistency of Fermi-LAT Observations of the Galactic Center with a Millisecond Pulsar Population in the Central Stellar Cluster. *JCAP*, 1103:010, 2011.

[80] Alex Geringer-Sameth, Matthew G. Walker, Savvas M. Koushiappas, Sergey E. Koposov, Vasily Belokurov, Gabriel Torrealba, and N. Wyn Evans. Indication of Gamma-ray Emission from the Newly Discovered Dwarf Galaxy Reticulum II. *Phys. Rev. Lett.*, 115(8):081101, 2015.

[81] Lars Hernquist. An Analytical Model for Spherical Galaxies and Bulges. *Astrophys. J.*, 356:359, 1990.

[82] Eli Visbal, Abraham Loeb, and Lars Hernquist. A Simple Model for the Density Profiles of Isolated Dark Matter Halos. 2012.

[83] Eugene Vasiliev. Dark matter annihilation near a black hole: Plateau vs. weak cusp. *Phys. Rev.*, D76:103532, 2007.

[84] Stuart L. Shapiro and Jessie Shelton. Weak annihilation cusp inside the dark matter spike about a black hole. *Phys. Rev.*, D93(12):123510, 2016.

[85] Misao Sasaki, Teruaki Suyama, Takahiro Tanaka, and Shuichiro Yokoyama. Primordial black holes-perspectives in gravitational wave astronomy. *Class. Quant. Grav.*, 35(6):063001, 2018.

[86] Timothy D. Brandt. Constraints on MACHO Dark Matter from Compact Stellar Systems in Ultra-Faint Dwarf Galaxies. *Astrophys. J.*, 824(2):L31, 2016.

[87] Bernard Carr, Florian Kuhnel, and Marit Sandstad. Primordial Black Holes as Dark Matter. *Phys. Rev.*, D94(8):083504, 2016.

[88] Andrey Katz, Joachim Kopp, Sergey Sibiryakov, and Wei Xue. Femtolensing by Dark Matter Revisited. *JCAP*, 1812:005, 2018.

[89] Yacine Ali-Haïmoud, Ely D. Kovetz, and Marc Kamionkowski. Merger rate of primordial black-hole binaries. *Phys. Rev.*, D96(12):123523, 2017.

[90] Hiroya Nishikawa, Ely D. Kovetz, Marc Kamionkowski, and Joseph Silk. Primordial-black-hole mergers in dark-matter spikes. 2017.

[91] Ryan M. O'Leary, Bence Kocsis, and Abraham Loeb. Gravitational waves from scattering of stellar-mass black holes in galactic nuclei. *Mon. Not. Roy. Astron. Soc.*, 395(4):2127–2146, 2009.

[92] G. D. Quinlan and S. L. Shapiro. Dynamical evolution of dense clusters of compact stars. ApJ, 343:725–749, August 1989.

[93] Henric Krawczynski. Difficulties of Quantitative Tests of the Kerr-Hypothesis with X-Ray Observations of Mass Accreting Black Holes. *Gen. Rel. Grav.*, 50(8):100, 2018.

[94] D. Porquet et al. A deep X-ray view of the bare AGN Ark120. V. Spin determination from disc-Comptonisation efficiency method. 2019.

[95] P. C. Peters. Gravitational Radiation and the Motion of Two Point Masses. *Phys. Rev.*, 136:B1224–B1232, 1964.

[96] M. Fujii, M. Iwasawa, Y. Funato, and J. Makino. Evolution of Star Clusters near the Galactic Center: Fully Self-consistent N-body Simulations. *Astrophys. J.*, 686:1082, 2008.

[97] Alexander Rasskazov and Bence Kocsis. The rate of stellar mass black hole scattering in galactic nuclei. 2019.

[98] Ilias Cholis, Ely D. Kovetz, Yacine Ali-Haïmoud, Simeon Bird, Marc Kamionkowski, Julian B. Muñoz, and Alvise Raccanelli. Orbital eccentricities in primordial black hole binaries. *Phys. Rev.*, D94(8):084013, 2016.

[99] Takashi Nakamura, Misao Sasaki, Takahir Tanaka, and Kip S. Thorne. Gravitational waves from coalescing black hole MACHO binaries. *Astrophys. J.*, 487:L139–L142, 1997.

[100] Martti Raidal, Christian Spethmann, Ville Vaskonen, and Hardi Veermäe. Formation and Evolution of Primordial Black Hole Binaries in the Early Universe. 2018.

[101] Bradley J. Kavanagh, Daniele Gaggero, and Gianfranco Bertone. Merger rate of a subdominant population of primordial black holes. *Phys. Rev.*, D98(2):023536, 2018.

[102] Kimitake Hayasaki, Keitaro Takahashi, Yuuiti Sendouda, and Shigehiro Nagataki. Rapid merger of binary primordial black holes: An implication for GW150914. *Publ. Astron. Soc. Jap.*, 68(4):66, 2016.

[103] Guillermo Ballesteros, Pasquale D. Serpico, and Marco Taoso. On the merger rate of primordial black holes: effects of nearest neighbours distribution and clustering. *JCAP*, 1810(10):043, 2018.

[104] Vincent Desjacques and Antonio Riotto. Spatial clustering of primordial black holes. *Phys. Rev.*, D98(12):123533, 2018.

[105] Torsten Bringmann, Paul Frederik Depta, Valerie Domcke, and Kai Schmidt-Hoberg. Strong constraints on clustered primordial black holes as dark matter. 2018.

[106] Brunetto Marco Ziosi, Michela Mapelli, Marica Branchesi, and Giuseppe Tormen. Dynamics of stellar black holes in young star clusters with different metallicities - II. Black hole-black hole binaries. *Mon. Not. Roy. Astron. Soc.*, 441(4):3703–3717, 2014.

[107] Douglas C. Heggie, Piet Hut, and Steven L. W. McMillan. Exchange cross-sections for hard binaries. *IAU Symp.*, 174:371, 1996.

[108] Alma X. Gonzalez-Morales, Stefano Profumo, and Farinaldo S. Queiroz. Effect of Black Holes in Local Dwarf Spheroidal Galaxies on Gamma-Ray Constraints on Dark Matter Annihilation. *Phys. Rev.*, D90(10):103508, 2014.